BACHELOR

# Active particles on a sphere

Morren, Maikel C.L.

*Award date:*
2019


Department of Applied Physics

# Active particles on a sphere

Bachelor End Project

Author:
*Maikel Cornelis Leonard Morren*

Supervisor:
*Dr. L.M.C. Janssen*

Eindhoven, July 3, 2019

**Abstract**

The behaviour of interacting active particles on curved surfaces is an interesting novel research topic, as the collective motion properties of active systems are non-trivially influenced by the intrinsic curvature of their environment. Especially scarcely understood is the behaviour of active crystals on these curved surfaces, which form at dense packing fractions close to unity. Using numerical simulations of active non-aligning interacting particles subjected to overdamped Brownian dynamics on the surface of a sphere, the short-term non-equilibrium effects of activity and temperature are investigated in relation to crystal formation. It is found that active crystals, in the absence of thermal fluctuations, perform a quasi steady collective rotation where the defects in the crystal act as attractors for the collective rotation axis. Furthermore, it is established that thermal fluctuations have an irrefutable effect on the scar formation in a passive crystal, with an increasing preference of smaller scars over isolated defects or longer scars. The present work serves as a foundation for future research on real active crystal formation at finite temperatures, which could be applied to study the behaviour of e.g. Volvox colonies or active colloids attached to a spherical droplet.

# Contents

# Chapter 1

# Introduction

From a mathematical point of view, the problem of finding the minimum energy configuration for interacting particles on a sphere is extremely complicated, and besides for some trivial cases for a handful of particles, analytically impossible [1]. In fact the problem of distributing points on the surface of a sphere has even been quoted to be one of the profound mathematical problems of this century [2]. From a historical and physical point of view, the most notorious of these problems is the *Thomson problem*, which tries to find the minimal energy configuration of $N$ electrons on a the surface of a sphere mutually, repelling each other through the Coulomb potential as an early toy model for the atom [3].

By contrast, the solution to the problem of stacking as many mutually repulsive particles as closely together as possible on a flat plane, is simply by forming a hexagonal lattice with equidistant particle spacing, resulting in a crystal [4]. A crystal can still be formed on the surface of a sphere by tiling its surface with hexagons, however it is impossible to completely tile the surface of a sphere solely with hexagons. To completely tile the surface of the sphere using regular polygons 12 pentagons are needed as dictated by the Euler characteristic for the surface of a sphere [5], see appendix A. These 12 pentagons correspond to 12 particles at the centroid of the pentagon which have merely 5 nearest neighbours as opposed to the 6 nearest neighbours of their hexagonal counterparts. Deviations from this preferable six-fold coordination are called *defects*, and are the source of impurities in crystals [6].

The problem of crystal formation on the surface of a sphere becomes even more intriguing when considering *active matter* Active matter is a relatively 'new' class of matter, which is capable of converting excess forms of energy into self driven motion [7]. Since active matter needs a continuous supply of energy to sustain its self-propulsion, active matter systems are purely dissipative and are constantly out of equilibrium. These local non-equilibrium processes can combine into a plethora of collective motion phenomena, including but not limited to: swarming [8, 9, 10], collective translation [9, 11], collective rotation [8], ageing [8] and turbulence [9, 12], where the type of emerging collective behaviour is dependent on the strength of the self-propulsion (the *activity*) and the density of active particles. Unlike passive matter which requires explicit alignment interactions to undergo any collective motion, self-propulsion alone is already a sufficient condition in active matter [13]. At sufficiently high densities, active matter crystallises [11, 13, 14], although the majority of reported effects and research are on less dense active liquid states.

A considerable amount of the early research in active matter was performed on systems of active rods, since rods most closely resemble the shapes of bacterial microswimmers, which are accurately described by an active matter model [8, 9, 15, 16]. Research on active point particles has also caught a great deal of attention [10, 11, 13, 14, 17, 18, 19, 20], although its application to real life situations is more limited. Interestingly, systems of active rods and active particles are not completely decoupled, as some researchers have modelled the defects in active nematic colloidal suspensions of rods as being active particles themselves. This analogy is justified since the collective motion properties of the nematic suspension propagate down to motion of the defects, although in those cases the 'particle' density is low [15, 21]. More recently research on active matter has also been performed on curved surfaces, showing that the presence of curvature non-trivially affects the collective motion properties and produces phenomena impossible on a flat plane (e.g. collective rotation instead of collective translation) [8, 20].

There is no standard approach to simulate active particles, or active matter in general. Some researches adopt a field theory approach [11, 14, 20], but most numerical research is performed within the framework of overdamped Brownian dynamics. In the latter category there is a noticeable division in three classes between the complexity of the used dynamical model.

(i) Simulations of interacting particles, in the absence of stochastic fluctuations, as in [8, 9, 15].

(ii) Simulations of non-interacting particles, affected only by thermal fluctuations, as in [17, 19, 20].

(iii) Simulations of both interacting and diffusing particles, as in [13, 16, 18].

In the current report, method (iii) will be applied using a soft repulsive interaction between active Brownian particles on the surface of a sphere at the packing fraction of unity. It should be noted that the interactions used in [13, 16, 18] are respectively a hard potential, an elastic spring interaction, and a screened Yukawa potential [22]. Additionally, those previous interaction potentials were all applied on a flat 2 dimensional plane, as opposed to the curved surface presented here. Furthermore, in this report the focus is on the short-term response of the system with minimal equilibration to better understand the non-equilibrium processes, as oppose to the long equilibration times in literature where the focus is on steady-state properties. hlThe aim of this work is to increase our understanding of the scarcely investigated high density solid phase of active matter on a sphere, by investigating the effects of thermal fluctuations and activity on a spherical crystal, by performing numerical simulations. The remainder of the report is structured as follows, in chapter 2 after a short mathematical description of the spherical manifold, the physical model of the particles, and the equations of motion will be discussed. In chapter 3 the numerical implementation of this model and the tools used for data analysis will be discussed. Next in chapter 4 the primary results regarding the simulations of interacting passive particles at absolute zero, interacting passive particles at finite temperature, and interacting active particles at absolute zero are presented. Lastly in chapter 5 a brief summary and discussion of these results is given along with the outlook for further research possibilities.

# Chapter 2

# Theory

Formally, the surface of the sphere is a two dimensional manifold $\mathcal{M}$, as any point on $\mathcal{M}$ can be uniquely specified by its polar and azimuthal angle $\theta_a, \phi_a$, where $\mathcal{M} = R \times \mathcal{S}^2$, with $\mathcal{S}^2$ denoting the unit sphere, and $R$ the radius of the sphere. The line element describing distances between any two points on $\mathcal{M}$ is given by

$$ds^2 = R^2 d\theta^2 + R^2 \sin(\theta)^2 d\phi^2 \tag{2.1}$$

for which no transformation $x = f(\theta, \phi),\ y = g(\theta, \phi)$ exists, such that the line element reduces to $ds^2 = dx^2 + dy^2$, thus representing an intrinsically curved surface [23]. Another way of interpreting this statement is that it is impossible to fold a sphere out of a flat piece of paper without deforming it, and thus the results of physics which hold on the flat plane need not hold on the spherical surface. By contrast with the sphere, the surface of a cylinder of radius $\rho$ is characterised by $ds^2 = dz^2 + \rho^2 d\phi^2$ with $\phi$ the polar angle in the $xy$-plane, can be reduced to the form $ds^2 = dx^2 + dy^2$ by simply letting $x = \rho\phi, y = z$, and indeed on a cylindrical surface particles arrange in a purely hexagonal structure as on the flat plane [24].

The 12 five-fold defects as imposed by the Euler characteristic for the sphere are the mere minimum number of defects as required by the topology, and form a highly idealistic picture of a spherical crystal [25]. The curvature of the sphere itself also imposes strain and stresses on the crystal, which increases the overall energy [26]. To mitigate this stress, the crystal can form additional defects by expiring this additional energy to deform the lattice, which although locally increasing the stress at the defect site, will overall add up to a global stress relief over the crystal itself [6]. This behaviour is unique to curved surfaces since on the flat plane adding defects will increase the global stress [5, 24]. However, these additional defects cannot be added at random as the Euler characteristic dictates that the total topological charge (which is $+1/3$ for a five-fold defect and $-1/3$ for a seven-fold defect) should be $+2$, which results in the formation of $5-7$ defect pairs, functioning like a defect dipole with zero net topological charge [5, 24, 26]. These topological dipoles then produce chains of $5-7$ defects often terminating in one of the 12 five-fold defects required by the topology, called *scars* [25].

## 2.1 Particle model

The activity of each particle $a$ is described by its orientation $\hat{u}_a$, which is determined by the direction of the self-propulsion force

$$\vec{F}_{act,a} = \gamma v_{act} \hat{u}_a = F_{act} \hat{u}_a \tag{2.2}$$

with $\gamma$ the friction coefficient (see below) and $v_{act}$ is the speed of the self-propulsion, where the magnitude of the self-propulsion is constant, according to the Active Brownian Particle (ABP) model [27]. For the remainder of this report, the term activity will be used to refer to the magnitude of the self-propulsion force. The appearance of the friction coefficient arises from the fact that in order to sustain constant motion along a straight line (determined by the direction of $\hat{u}_a$), the self-propulsion force must balance the friction force induced by the active motion: $\vec{F}_{fric} = -\gamma \vec{v}_{act}$. On a flat plane, the orientation vector $\hat{u}_a$ is given by

$$\hat{u}_a = \begin{pmatrix} \cos(\varphi_a) \\ \sin(\varphi_a) \end{pmatrix} \tag{2.3}$$

where $\varphi_a$ is the angle $\hat{u}_a$ makes with respect to the $x$-axis, see figure 2.1. [1]. On the surface of the sphere implementing equation (2.3) is less straightforward since there is no fixed $x$-axis, but the orientation vector will always lie in the local tangent plane $\mathcal{T}_a$ to the position of particle $a$. Tensor calculus states that for an arbitrary Riemannian manifold $\mathcal{M}$, the manifold can always locally be described by pseudo-Cartesian coordinates, by performing suitable coordinate transformations, where the pseudo-Cartesian coordinate axes are formed by the local basis vectors [23]. On the sphere this means that for each particle $a$, the tangent plane at the position $\vec{r}_a$ is represented by a Cartesian coordinate system $(\tilde{x}, \tilde{y})$, with the $\tilde{x}$-axis coinciding with $\hat{\theta}(\theta_a, \phi_a)$ and the $\tilde{y}$-axis coinciding with $\hat{\phi}(\theta_a, \phi_a)$, see figure 2.2, such that equation (2.3) still describes the direction of the orientation vector for each particle on the sphere, with $\hat{\theta}$ and $\hat{\phi}$ the unit vectors in the $\theta$ and $\phi$ directions respectively.

The particles are modelled as soft spheres of diameter $\sigma$, and each particle pair $(a, b)$ interacts through a Lennard-Jones potential

$$V_{LJ}(r_{ab}) = 4\epsilon \left[ (\frac{\sigma}{r_{ab}})^{12} - (\frac{\sigma}{r_{ab}})^{6} \right] \tag{2.4}$$

where $\epsilon$ is the potential strength, and $r_{ab} = \|\vec{r}_a - \vec{r}_b\|$ denotes the distance between the centres of mass of the particles. The first term in the Lennard-Jones potential represents the short range repulsion due to the excluded volume of each particle, whereas the second term represents the long rang attraction by the Vanderwaals interaction. A graph of $\frac{V}{\epsilon}$ versus $\frac{r}{\sigma}$ is shown in figure 2.3. The force particle $b$ then exerts on particle $a$ is

$$\vec{F}_{ba} = -\boldsymbol{\nabla}_{\vec{r}_a} V_{LJ} = -24\epsilon \frac{\sigma^6 (r_{ab}^6 - 2\sigma^6)}{r_{ab}^{13}} \hat{r}_{ab} \tag{2.5}$$

where $\hat{r}_{ab}$ is the unit vector pointing from particle $a$ in the direction of particle $b$. The energy minimum corresponds to the point $r_c$ where $\frac{\mathrm{d}V_{LJ}}{\mathrm{d}r_{ab}}|_{r_c} = 0$ which from equation (2.5) follows that

[1] In figure 2.1 $\hat{u}_{\perp,a}$ refers to the vector perpendicular to $\hat{u}_a$ The perpendicular vector to $\hat{u}_a$ was obtained by considering a coordinate rotation by $\varphi_a$ about the $x$-axis, such that $(\hat{u}_a, \hat{u}_{\perp,a})$ spans the flat plane. In principle $-\hat{u}_{\perp,a}$ is also a vector perpendicular to $\hat{u}_a$, but the basis $(\hat{u}_a, -\hat{u}_{\perp,a})$ does not correspond to a right-handed coordinate system obtained from $(x, y)$ by a rotation, and is thus an ill choice.

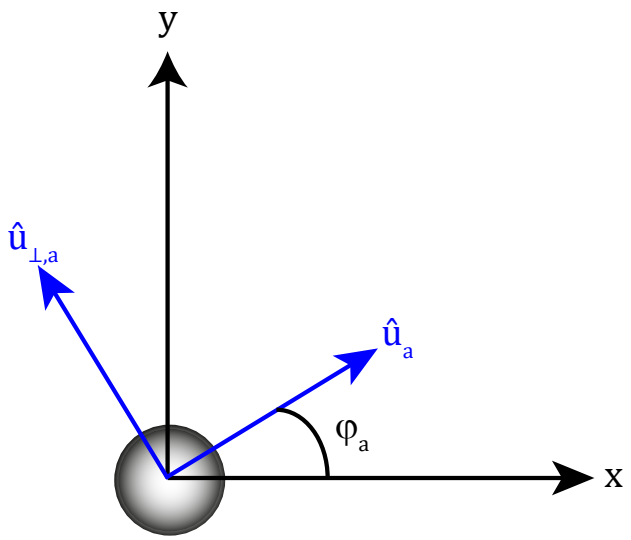


Figure 2.1: The model for activity on a flat plane. The orientation vector $\hat{u}_a$ indicating the direction of the active self-propulsion force of particle $a$ and vector $\hat{u}_{\perp,a}$ perpendicular to $\hat{u}_a$ are shown.

$r_c = 2^{1/6}\sigma$. From equation (2.5) it also follows that for $r_{ab} < r_c$ the force is repulsive and for $r_{ab} > r_c$ the force is attractive, as indicated by blue and red respectively in figure 2.3. The Cartesian components of the force can be found by the chain rule as

$$F_{ba,\beta} = -\frac{\mathrm{d}V_{LJ}}{\mathrm{d}r_{ab}}\frac{\partial r_{ab}}{\partial \beta_a} = -24\epsilon\frac{\sigma^6(r_{ab}^6 - 2\sigma^6)}{r_{ab}^{14}}(\beta_a - \beta_b) \tag{2.6}$$

where $\beta = (x, y, z)$ and $r_{ab} = \sqrt{(x_a - x_b)^2 + (y_a - y_b)^2 + (z_a - z_b)^2}$ is used to evaluate the partial derivative. Since $r_{ab}$ is the same for the interaction pairs $(a, b)$ and $(b, a)$, similarly the force particle $a$ exerts on $b$ is given by

$$F_{ab,\beta} = -24\epsilon\frac{\sigma^6(r_{ab}^6 - 2\sigma^6)}{r_{ab}^{14}}(\beta_b - \beta_a) = -F_{ba,\beta} \tag{2.7}$$

which is simply Newton's third law for pairwise interaction forces.

Since crystallisation is the main topic of interest, the particles are densely packed and predominantly feel the repulsion of their nearest neighbours and next nearest neighbours, whereas the attraction of particles in the intermediate range will be negligible compared to the repulsion. Therefore it is suitable to only consider the repulsive part of the Lennard-Jones potential, and by convention shift the potential upwards such that the truncated potential is purely positive and continuous. This truncated Lennard-Jones potential is known as the Weeks-Chander-Andersen (WCA) potential [28], where the shift follows from $V_{LJ}(r_c) = -\epsilon$, and is given by

$$V_{WCA}(r_{ab}) = \begin{cases} V_{LJ} + \epsilon & r_{ab} \leq r_c \\ 0 & r_{ab} > r_c \end{cases}. \tag{2.8}$$

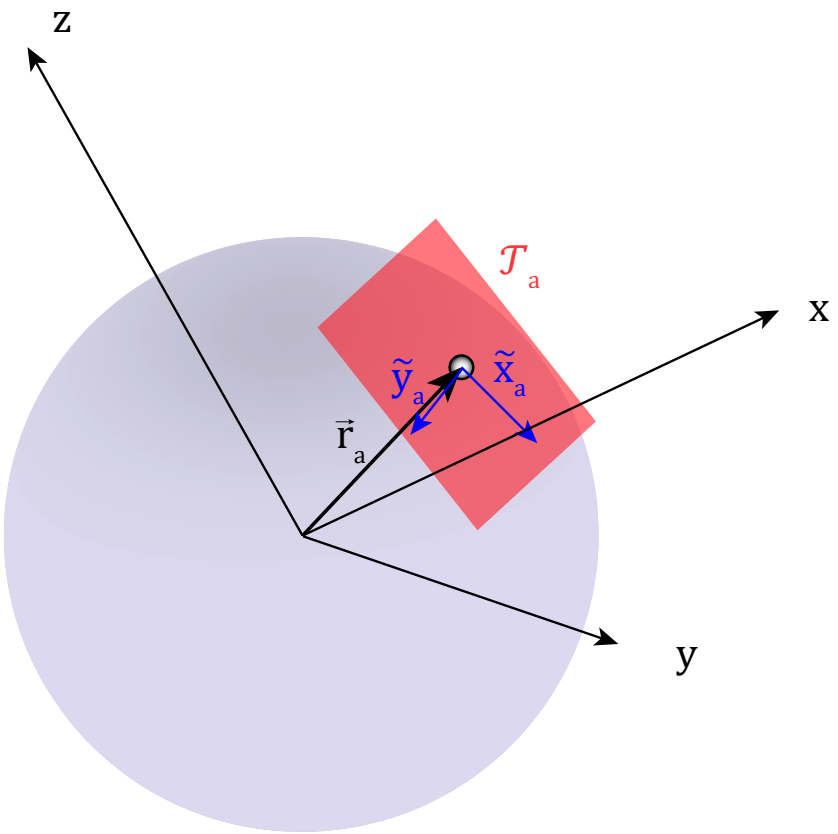


Figure 2.2: The tangent plane $\mathcal{T}_a$ of particle $a$ at the position $\vec{r}_a$, with the local $\tilde{x}_a$-axis coinciding with the $\hat{\theta}$ direction, and the local $\tilde{y}_a$-axis coinciding with the $\hat{\phi}$ direction at the coordinates $(r_a, \theta_a, \phi_a)$.

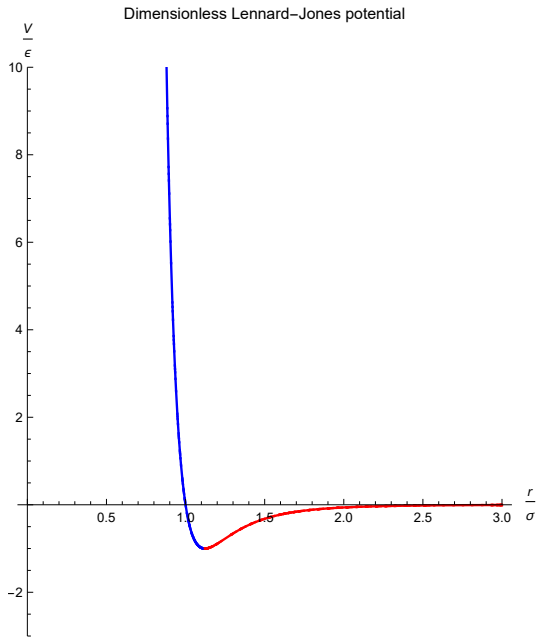


Figure 2.3: Plot of the dimensionless Lennard-Jones potential versus dimensionless interparticle distance. The blue colour of the graph corresponds to the region of repulsion, and the red colour of the graph corresponds to the region of attraction.

## 2.2 Equations of motion

The equations of motion for a non-interacting passive particle undergoing Brownian motion are given by the Langevin equations

$$m_a\ddot{\vec{r}}_a(t) = -\gamma\dot{\vec{r}}_a(t) + \sqrt{2\gamma k_b T\delta(t)} * \vec{\zeta}_a \tag{2.9a}$$

$$\gamma_R\dot{\varphi}_a(t) = \sqrt{2\gamma_R k_b T\delta(t)} * \eta_a \tag{2.9b}$$

where $m_a$ denotes the mass of particle $a$, $\vec{r}_a$ its position, $\gamma$ the translational friction coefficient, $k_b$ the Boltzmann constant, $T$ the temperature, $\gamma_R$ the rotational friction coefficient, and $\zeta_a, \eta_a$ two random numbers representing the magnitude of the thermal fluctuations, which are uncorrelated between particles. The $\delta(t)$ function in equation (2.9) is due to the uncorrelated nature of the fluctuations at subsequent times (since the random kicks form a Wiener process [29]), see appendix B.
In general, when considering activity and interactions, these equations will be supplemented by the acting forces and torques

$$m_a\ddot{\vec{r}}_a(t) = -\gamma\dot{\vec{r}}_a(t) + \vec{F}_{act,a} + \vec{F}_{int,a} + \vec{F}_{con} + \sqrt{2\gamma k_b T\delta(t)} * \vec{\zeta}_a \tag{2.10a}$$

$$\gamma_R\dot{\varphi}_a(t) = \left(\vec{r}_a(t) \times \sum \vec{F}\right) + \sqrt{2\gamma_R k_b T\delta(t)} * \eta_a \tag{2.10b}$$

where $\vec{F}_{int,a}$ is the total interaction force on particle $a$ from all pairs $(a, b)$ given by

$$\vec{F}_{int,a} = -\boldsymbol{\nabla}_{\vec{r}_a} V_{tot} = -\boldsymbol{\nabla}_{\vec{r}_a}\Big(\frac{1}{2}\sum_a\sum_b V_{WCA}(r_{ab})\Big), \tag{2.11}$$

$\vec{F}_{act,a}$ the active self-propulsion force given by equation (2.2), and $\vec{F}_{con}$ the constraint force keeping the particles constrained to the surface of the sphere. The constraint of the spherical surface is given by $g(x_a, y_a, z_a) = x_a^2 + y_a^2 + z_a^2 - R^2 = 0$, which is time independent. For such a time independent constraint dependent only the particle positions, the constraint force will be perpendicular to the surface and thus $\vec{F}_{con} = -\lambda \boldsymbol{\nabla} g$ where $\lambda$ has the same functionality as a Lagrange multiplier for optimisation under a constraint [30]. This prefactor $\lambda$ can be determined by considering $\frac{\mathrm{d}g}{\mathrm{d}t}$ and taking the inner product of equation (2.10a) with $\dot{\vec{r}}$, see appendix C, to yield

$$\begin{aligned} m_a \ddot{\vec{r}}_a(t) = &- \gamma \dot{\vec{r}}_a(t) + \vec{F}_{act,a} + \left[\vec{F}_{int,a} - \left(\vec{F}_{int,a} \cdot \hat{r}\right)\hat{r}\right] + \\ &\left[\sqrt{2\gamma k_b T \delta(t)} * \vec{\zeta}_a - \left(\sqrt{2\gamma k_b T \delta(t)} * \vec{\zeta}_a \cdot \hat{r}\right)\hat{r}\right] - m_a \dot{r}_a^2(t)\hat{r}. \end{aligned} \tag{2.12}$$

Equation (2.12) shows that any radial component of the interaction force or thermal fluctuations is projected out, such that the motion will always be constrained to the spherical surface.
Lastly, since the motion is frictional and thus dissipative the inertia term will be negligible with respect to the friction term, such that the *overdamped limit* can be considered, reducing the translational equations of motion to

$$\gamma \dot{\vec{r}}_a = \vec{F}_{act,a} + \left[\vec{F}_{int,a} - \left(\vec{F}_{int,a} \cdot \hat{r}\right)\hat{r}\right] + \left[\sqrt{2\gamma k_b T \delta(t)} * \vec{\zeta}_a - \left(\sqrt{2\gamma k_b T \delta(t)} * \vec{\zeta}_a \cdot \hat{r}\right)\hat{r}\right]. \tag{2.13}$$

## 2.3 Equations of motion in the local tangent plane

As equation (2.13) and the discussion in appendix C demonstrate that all motion stays constrained to the spherical surface, the equations of motion can be equivalently solved in the local tangent plane $\mathcal{T}_a$ of each particle $a$, without the need of accounting for the constraint force, making the equations of motion more compact. Furthermore, since $\mathcal{T}_a$ is characterised by local Cartesian coordinates, the behaviour of the equations of motion can be understood more clearly in terms of their vectorial components. The computational implementation of this tangent plane assumption is discussed in chapter 3.

For the angular equations of motion (2.10b) it is especially useful to consider the application of the local tangent plane, as $\varphi_a$ is the angle of the orientation vector $\hat{u}$ with respect to the local $\tilde{x}$-axis. Spherical particles as considered here experience no torque about their axis, such that the angular equations of motion simply reduces to angular diffusion by Brownian motion (equation (2.9b)). The effects of rotational diffusion is best understood by considering its effects on the components of the orientation vector. By the chain rule

$$\frac{\mathrm{d}\hat{u}_a}{\mathrm{d}t} = \frac{\mathrm{d}}{\mathrm{d}t}\begin{pmatrix}\cos\varphi_a \\ \sin\varphi_a\end{pmatrix} = \begin{pmatrix}-\sin\varphi_a \\ \cos\varphi_a\end{pmatrix}\frac{\mathrm{d}\varphi_a}{\mathrm{d}t}, \tag{2.14}$$

which shows that random kicks can only change the direction of $\hat{u}_a$, as the evolution of $\hat{u}_a$ is in the direction of $\hat{u}_{\perp,a}$, such that $\|\hat{u}_a\| = 1$ at all times, see figure 2.4.

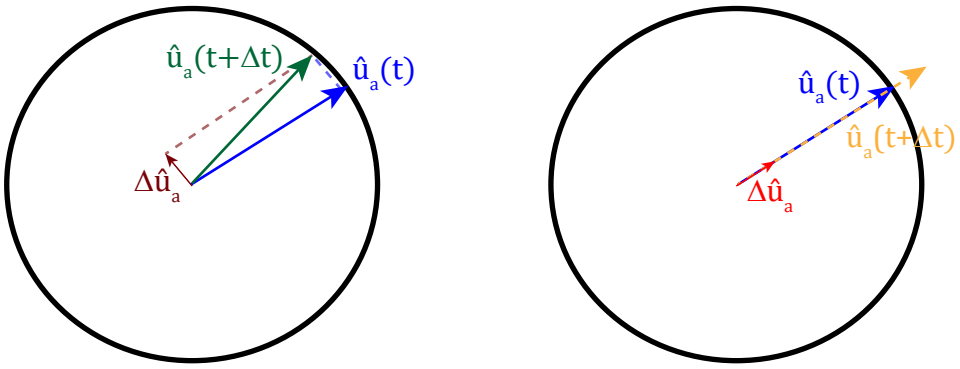


Figure 2.4: The effects of kicks (denoted by $\Delta\hat{u}_a$) perpendicular and parallel to $\hat{u}_a$. Any kicks perpendicular to $\hat{u}_a$ still lie on the same unit circle as $\hat{u}_a$, whereas kicks parallel to $\hat{u}_a$ result in a new orientation no longer on the unit circle, since $\hat{u}_a$ simply gains in magnitude.

The equations for the components of $\hat{u}_a$ are then found by dividing equation (2.9b) by $\gamma_R$

$$\frac{\mathrm{d}\hat{u}_{a,\tilde{x}}}{\mathrm{d}t} = -\hat{u}_{a,\tilde{y}}\sqrt{2k_bTD_{0,r}\delta(t)} * \eta_a \tag{2.15a}$$

$$\frac{\mathrm{d}\hat{u}_{a,\tilde{y}}}{\mathrm{d}t} = \hat{u}_{a,\tilde{x}}\sqrt{2k_bTD_{0,r}\delta(t)} * \eta_a \tag{2.15b}$$

where $D_{0,R}$ is the rotational mobility coefficient given by

$$D_{0,R} = \frac{D_R}{k_bT} = \frac{1}{\gamma_R} \tag{2.16}$$

where equation (B.14) was used for the rotational diffusion coefficient $D_R$.

In a similar fashion equation (2.13) can be rewritten into differential equations for $\tilde{x}, \tilde{y}$, but this requires some extra subtlety. The rotational friction coefficient $\gamma_R$ is a scalar on the flat plane since there is only one rotation axis in the plane, but in general the translational friction coefficient $\gamma$ will be a friction tensor $\underline{\underline{\gamma}}$ describing the degree of friction in each direction. For anisotropic particles friction will be non-uniform, causing the Brownian motion to be stronger in the direction of lowest friction coefficient. Although the spherical particles considered are completely isotropic such that $\underline{\underline{\gamma}} = \gamma\underline{\underline{I_2}}$, where $\underline{\underline{I_2}}$ denotes the unit matrix in two dimensions, it is instructive to derive the differential equations for $\tilde{x}, \tilde{y}$ under Brownian motion of an anisotropic object which has a different friction coefficients $\gamma_\parallel, \gamma_\perp$ for movement parallel and perpendicular to its polar axis. These equations then reduce to the proper equations for spherical point-like particles by letting $\gamma_\parallel = \gamma_\perp$. The polar axis is taken to be the direction of the self-propulsion force, i.e. the direction of $\hat{u}_a$, see figure 2.5. Letting $(V_a, W_a)$ denote the coordinates along $\hat{u}_a$ and $\hat{u}_{\perp,a}$ respectively, equation (2.13) becomes

$$\frac{\mathrm{d}V_a}{\mathrm{d}t} = \sqrt{2D_{0,\parallel}k_bT\delta(t)}\zeta_{V,a} \tag{2.17a}$$

$$\frac{\mathrm{d}W_a}{\mathrm{d}t} = \sqrt{2D_{0,\perp}k_bT\delta(t)}\zeta_{W,a} \tag{2.17b}$$

where $\zeta_{V,a} = \vec{\zeta}_a \cdot \hat{u}_a$, $\zeta_{W,a} = \vec{\zeta}_a \cdot \hat{u}_{a,\perp}$ and $D_{0,\beta}$ is the translational mobility coefficient according to

$$D_{0,\beta} = \frac{D_\beta}{k_b T} = \frac{1}{\gamma_\beta} \tag{2.18}$$

where $\beta = (\perp, \parallel)$. In equation (2.17) the forces have been left as their magnitude does not depend on the friction coefficient, and the forces can always decomposed with respect the new basis of the local tangent plane. From figure 2.1 and the definition of $V_a, W_a$ it follows that

$$\tilde{x}_a = \cos\varphi_a V_a - sin\varphi_a W_a = \hat{u}_{a,\tilde{x}} V_a - \hat{u}_{a,\tilde{y}} W_a \tag{2.19a}$$
$$\tilde{y}_a = \sin\varphi_a V_a + \cos\varphi_a W_a = \hat{u}_{a,\tilde{x}} V_a + \hat{u}_{a,\tilde{x}} W_a \tag{2.19b}$$

such that equation (2.17) in terms of the local Cartesian coordinates becomes

$$\frac{\mathrm{d}\tilde{x}_a}{\mathrm{d}t} = \sqrt{2D_{0,\parallel} k_b T \delta(t)}\hat{u}_{a,\tilde{x}}\zeta_{V,a} - \sqrt{2D_{0,\perp} k_b T \delta(t)}\hat{u}_{a,\tilde{y}}\zeta_{W,a} \tag{2.20a}$$
$$\frac{\mathrm{d}\tilde{y}_a}{\mathrm{d}t} = \sqrt{2D_{0,\parallel} k_b T \delta(t)}\hat{u}_{a,\tilde{y}}\zeta_{V,a} + \sqrt{2D_{0,\perp} k_b T \delta(t)}\hat{u}_{a,\tilde{x}}\zeta_{W,a}. \tag{2.20b}$$

By letting $D_{0,\parallel} = D_{0,\perp} = D_{0,T}$, and adding the forces again, the full translational equations of motion in the tangent plane reads

$$\frac{\mathrm{d}\tilde{x}_a}{\mathrm{d}t} = D_{0,T}F_{a,\tilde{x}} + \sqrt{2D_{0,T} k_b T \delta(t)}\big(\hat{u}_{a,\tilde{x}}\zeta_{\parallel,a} - \hat{u}_{a,\tilde{y}}\zeta_{\perp,a}\big) \tag{2.21a}$$
$$\frac{\mathrm{d}\tilde{y}_a}{\mathrm{d}t} = D_{0,T}F_{a,\tilde{y}} + \sqrt{2D_{0,T} k_b T \delta(t)}\big(\hat{u}_{a,\tilde{y}}\zeta_{\parallel,a} + \hat{u}_{a,\tilde{x}}\zeta_{\perp,a}\big) \tag{2.21b}$$

where the interaction force and self-propulsion force in each direction have been bundled into the single variable $F$, and the substitution $(\zeta_{V,a}, \zeta_{W,a}) \to (\zeta_{\parallel,a}, \zeta_{\perp,a})$ has been made for clarity. The fruitfulness of this detour derivation lies in the term in between parentheses, which shows the dependence of Brownian motion on the orientation vector which would not have been obtained if $\gamma$ had been treated as a scalar in the translational equations of motion. [2]

[2] Although one could argue that since $\hat{u}$ is normalised and $\zeta_{\parallel,a}, \zeta_{\perp,a}$ are uncorrelated random numbers, $\hat{u}_{a,\tilde{x}}\zeta_{\parallel,a} - \hat{u}_{a,\tilde{y}}\zeta_{\perp,a}$ and $\hat{u}_{a,\tilde{y}}\zeta_{\parallel,a} + \hat{u}_{a,\tilde{x}}\zeta_{\perp,a}$ also form two independent random numbers, (say $\zeta_{a,\tilde{x}}, \zeta_{a,\tilde{y}}$) with the same first and second moments. However, this method is devoid of generality as it cannot be applied to situations of anisotropic particles.

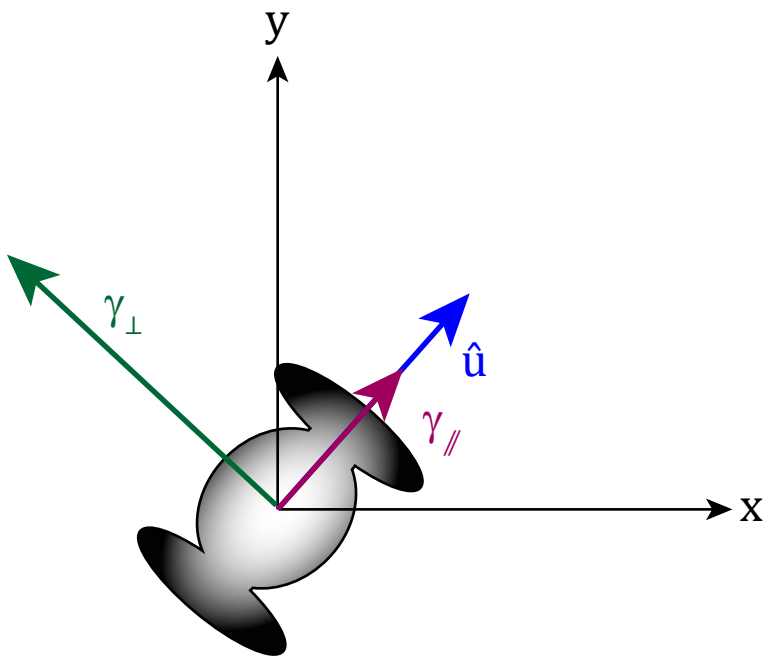


Figure 2.5: Example of an anisotropic object which has 2 different friction coefficients: one parallel to its axis of self-propulsion and one perpendicular to its axis of self-propulsion. The geometry of the object will largely determine which of these friction is dominant [9]. The difference between $\gamma_{\|}$ and $\gamma_{\perp}$ has been exaggerated for clarity.

# Chapter 3

# Methods

To investigate the effects of activity and temperature on the crystallisation on a spherical surface, the equations of motion are integrated numerically using the Euler-Maruyama method [10] in the local tangent plane of each particle, for a system of $N$ particles on a sphere of radius $R$.
The equations of motion are non dimensionalised by choosing a characteristic scales for length, time, energy and the mobility coefficient. However, as the equations of motion only involve the three fundamental units for mass, length and time, only three of these characteristic scales can be chosen independently. The fourth characteristic scale can then completely be expressed in the other three characteristic scales, according to the Buckingham Π theorem [31]. For the independent characteristic scales $\sigma$,$\epsilon$ and $D_M$ are chosen, such that the characteristic time scale follows from dimensional analysis as $\tau = \frac{\sigma^2}{\epsilon D_M}$.
Another important dimensionless parameter in active matter simulations is the packing fraction $\phi = \frac{N\pi(\sigma/2)^2}{4\pi R^2}$, which gives the ratio between the surface occupied by the particles and the surface of the sphere, thus serving as a metric for the density of the system. As discussed in chapter 1 the value of $\phi$ has a significant influence on the type of collective motion observed. Since crystallisation is the topic of interest, all simulations are performed at the dense packing fraction of $\phi = 1$, such that particle interactions will dominate over the self-propulsion or thermal fluctuations, preventing the system from forming a liquid or gas [11]. For the remainder of this chapter all quantities refer to their dimensionless counterparts without any explicit notation to differentiate between them, unless explicitly stated.

## 3.1 Initialisation

The simulation begins by either reading in the $(x_a, y_a, z_a)$ positions of each particle from an equilibrated dataset belonging to special magic particle numbers (see chapter 4) or by generating a random initial configuration. The initial $(x_a, y_a, z_a)$ coordinates of each particle are obtained by drawing two random numbers, $n_1$ and $n_2$, from a uniform distribution ranging between 0 and 1, such that the polar- and azimuthal angle of each particle is given by $\theta_a = \arccos(2\pi n_1 - 1)$ and $\phi_a = 2\pi n_2$, corresponding to the conventional ranges of $\theta \in [0, \pi]$ and $\phi \in [0, 2\pi)$ respectively. From these initial angles, the $(x_a, y_a, z_a)$ are then obtained by the standard transformation rules for spherical coordinate systems, see appendix D. Next the orientation vector $\hat{u}_a = (u_{x,a}, u_{y,a}, u_{z,a})$ of each particle is determined by drawing another two random numbers

$n_3, n_4$ to determine the angles $\tilde{\theta}, \tilde{\phi}$ in a similar fashion as the polar- and azimuthal angles for the positions. Here tildes have been used to explicitly distinguish them from the angles used for positions, since each were drawn with a different set of random numbers.
Due to the random aspect of the initialisation $\hat{u}_a$ will not lie completely in the local tangent plane $\mathcal{T}_a$ of each particle, which is in contrast with the particles being confined to move on the spherical surface. Therefore the radial part of $\hat{u}_a$ is filtered out, such that $\hat{u}_a$ will lie completely in the local tangent plane spun by $(\tilde{x}_a, \tilde{y}_a)$. Lastly $\hat{u}_a$ is subsequently renormalised after the radial component has been filtered out to satisfy $\|\hat{u}_a\| = 1$. The local components of $\hat{u}_a$ are then given by $u_{a,\tilde{x}} = \hat{u}_a \cdot \hat{\theta}, u_{a,\tilde{y}} = \hat{u}_a \cdot \hat{\phi}$. This random initial configuration is generated on a sphere of radius $r' > R$ corresponding to a dilute packing fraction of $\phi = 0.1$, such that the initial configuration is relatively stress free with large inter-particle distances, and any overlaps arising from randomisation are removed by displacing one of the overlapping particles over a distance of maximum $\frac{\sigma}{2}$ without causing new overlaps.

After all positions have been initialised and any initial overlap has been removed, the sphere is gradually shrunk from the initial radius $r'$ to the desired radius $R$ corresponding to a packing fraction of 1, in 100 steps. In each shrinking step the $(x_a, y_a, z_a)$ coordinates are rescaled to the new size of the shrunken sphere. After each shrinking step the sphere is briefly integrated during 100 time steps to allow the system to respond to the shrinking, where the time integration is discussed further below. During the first 30 shrinking steps, the system is checked and corrected for unphysical overlaps.

Alternatively, if the system is initialised by loading in the $(x_a, y_a, z_a)$ coordinates for special magic particle numbers, the sphere is already at the desired radius $R$ and only the orientation vector of each particle $\hat{u}_a$ is randomly generated by the same method as described above.

## 3.2 Numerical integration of the equations of motion

The numerical integration of the equation of motion follows by applying an Euler integration scheme to the deterministic part containing the forces, and then adding the stochastic noise term, at each time step. Thus, at each timestep of size $\Delta t$, the following equations are solved:

$$\tilde{x}_a(t + \Delta t) = \tilde{x}_a(t) + D_T^\star F_{a,\tilde{x}}(t)\Delta t + \sqrt{2D_T^\star T^\star \Delta t}\big(u_{a,\tilde{x}}(t) * \zeta_{a,\parallel} - u_{a,\tilde{y}}(t) * \zeta_{a,\perp}\big) \tag{3.1a}$$

$$\tilde{y}_a(t + \Delta t) = \tilde{y}_a(t) + D_T^\star F_{a,\tilde{y}}(t)\Delta t + \sqrt{2D_T^\star T^\star \Delta t}\big(u_{a,\tilde{y}}(t) * \zeta_{a,\parallel} + u_{a,\tilde{x}}(t) * \zeta_{a,\perp}\big) \tag{3.1b}$$

$$u_{a,\tilde{x}}(t + \Delta t) = u_{a,\tilde{x}}(t) - u_{a,\tilde{y}}(t)\sqrt{2D_R^\star T^\star \Delta t} * \eta \tag{3.1c}$$

$$u_{a,\tilde{y}}(t + \Delta t) = u_{a,\tilde{y}}(t) + u_{a,\tilde{x}}(t)\sqrt{2D_R^\star T^\star \Delta t} * \eta \tag{3.1d}$$

where $D_T^\star$ represents the translational mobility coefficient ($D_T^\star = D_T/D_M$), $D_R^\star$ the rescaled rotational mobility coefficient ($D_R^\star = D_R/D_M$), $T^\star$ the rescaled temperature ($T^\star = k_b T/\epsilon$), $\eta$ and $\zeta$ are two distinct random variables from a Gaussian distribution with a first moment of 0 and second moment of 1 [32]. The substitution of $\delta(t) \to \Delta t$ results from the discretisation of equations (2.15) and (2.21) and is valid for small timesteps $\Delta t \ll \tau$.
Since the local tangent planes do not form a global reference system as each particle has its own origin and local direction of $\hat{\theta}, \hat{\phi}$, the displacements in the local tangent plane are translated to

displacements in the global Cartesian coordinate system:

$$\begin{cases} \Delta x_a = \Delta\vec{\tilde{r}}_a \cdot \hat{x} \\ \Delta y_a = \Delta\vec{\tilde{r}}_a \cdot \hat{y} \\ \Delta z_a = \Delta\vec{\tilde{r}}_a \cdot \hat{z} \end{cases} \tag{3.2}$$

such that the global $(x_a, y_a, z_a)$ coordinates can be updated, where $\Delta\vec{\tilde{r}}_a = \Delta\tilde{x}_a\hat{\theta}_a + \Delta\tilde{y}_a\hat{\phi}_a$. Since the displacements $\Delta\tilde{x}$ and $\Delta\tilde{y}$ are linear in the local tangent plane, and $\mathcal{T}_a$ only perfectly coincides with the spherical surface at the initial location $(r_a, \theta_a, \phi_a)$ itself, the new $(x_a, y_a, z_a)$ coordinates will not lie perfectly on the surface of the sphere. This discrepancy is corrected by properly renormalising the coordinates by the factor $R/\sqrt{x_a^2 + y_a^2 + z_a^2}$ to project them back on the surface. Lastly, these projected and updated coordinates are used to calculate the new polar- and azimuthal angle of each particle after the displacement according to the relations in appendix D. These translation and projection steps may seem cumbersome, but are also applied in literature [10], since the alternative for solving the equations of motion for the azimuthal- and polar angles is significantly more complicated, including explicit coupling terms of the derivatives in the differential equations [19].

For the orientation vectors a similar technique is applied: after the orientation vector is rotated by the thermal fluctuation, the change of the components in the local tangent plane is translated back into its Cartesian components. The components of the orientation vector in the local tangent plane have to be solved anyway, since they couple to the thermal noise terms in the translational equations of (3.1). Lastly, these Cartesian components are then subsequently projected back onto the sphere by projecting out their radial component and subsequently renormalising $\hat{u}$, as described above.

## 3.3 Force calculation

The force calculation involves both the interaction force and the self-propulsion force, for which the opposite strategy as the calculation of the displacements is applied. That is, first the global Cartesian components of the forces are calculated to facilitate vectorial addition, and these Cartesian components are then transformed into the components in the local tangent plane.
Since the self-propulsion force is modelled as $\vec{F}_{act,a} = F_{act}\hat{u}_a$, the Cartesian components of the self-propulsion force simply follow from the Cartesian components of the orientation vector: $F_{act,a,\beta} = F_{act}u_{a,\beta}$, with $\beta = x, y, z$. The interaction force between a particle pair $(a, b)$ follows from equation (2.5), but since the WCA potential has a cutoff at $r_c = 2^{1/6}\sigma$, the force between any pair $(a, b)$ is zero if $r_{ab} > r_c$. For a system of large $N$ computing the total interaction force directly from equation (2.11) is thus inefficient since only a fraction of all particles will lie in the cutoff range. Regardless of this cutoff, since the Cartesian components of the force obey

$$F_{ba,\beta} = -F_{ab,\beta} \tag{3.3}$$

where $\beta = x, y, z$. The force calculation routine does not require to calculate the force between all particle pairs $(a, b)$, instead it suffices to only consider the pairs where $a > b$ and use equation (3.3) to determine the force which particle $a$ exerts on particle $b$.

The components of the total force in the local tangent plane is then obtained by

$$\begin{cases} F_{a,\tilde{x}} = \vec{F}_a \cdot \hat{\theta}_a \\ F_{a,\tilde{y}} = \vec{F}_a \cdot \hat{\phi}_a \end{cases}, \tag{3.4}$$

where $\vec{F} = \sum_\beta F_\beta \hat{\beta}$ with $\beta = x, y, z$.

However the cutoff range gives an elegant method to bypass the force calculation for particles pairs outside the cutoff range. By dividing the surface into cells with a size of $r_c \times r_c$, the interactions of a particle inside a cell will always be limited to the other particles in the same cell, and the particles in directly neighbouring cells. For clarity, this method will first be illustrated on the Euclidean plane. Consider a box of size $L \times L$ on the Euclidean plane and let $L$ be $m \times r_c$, such that the box can be perfectly divided into $m^2$ cells of size $r_c \times r_c$, where $m \in \mathbb{Z}$. [3] As each particle is characterised by its coordinates $(x_a, y_a) \in [0, L]$, each particle can be assigned to a particular cell, based on its coordinates. Let each cell be indexed by $(i, j)$, where $i$ refers to the cell number on the $x$-axis and $j$ refers to the cell number on the $y$-axis, then each particle can be assigned to a cell with index $(i, j)$ with $i = \lceil \frac{x_a}{r_c} \rceil, j = \lceil \frac{y_a}{r_c} \rceil$. Then, a circle of radius $r_c$ drawn from every particle inside the cell $(i, j)$ will always be confined to the cells $i' \in \{i-1, i+1\}, j' \in \{j-1, j+1\}$. To compute the total interaction force on particle $a$ in cell $(i, j)$, the distance $r_{ab}$ between particles $a$ and $b$ only has to be evaluated over 9 cells, and only if $r_{ab} < r_c$ the force has to be computed, see figure 3.1.
As a comparison, if no cell listing is employed the force calculation on each particle requires would require $N - 1$ inter-particle distances to be evaluated, leading to a total of $\mathcal{O}(N^2)$ operations assessing whether particles lie within the each other cutoff range. If a cell listing is used and the particles were homogeneously distributed in the plane, each cell contains $N/m^2$ particles, which is independent of the system size $N$, as for a fixed packing fraction the box size grows proportional to $N$. The total number of neighbouring cells is proportional to $m^2$, which is proportional to the box size. Thus in total for a cell listing only $\mathcal{O}(N^2/m^2) \backsim \mathcal{O}(N)$ operations are used assessing whether particles lie within each other cutoff range, which is significantly less than $\mathcal{O}(N^2)$ in the absence of a cell listing for large $N$.

## Cell list on the spherical manifold

In principle the method discussed above could be extended to a 3D Euclidean space with particle positions $(x_a, y_a, z_a)$, such that the space is filled by $m^3$ cubes of size $r_c \times r_c \times r_c$. However, this would be inefficient for the force calculation on the surface of a sphere as most cubes would lie completely in the interior and exterior of the sphere, containing zero particles. Instead, as the particles are constrained to the 2D manifold $\mathcal{M} = R \times \mathcal{S}^2$, a 2D cell listing is more suitable. However this is accompanied by some subtleties:

(i) The manifold $\mathcal{M}$ is non-Euclidean, but Riemannian. This implies that concepts such as distances are no longer given by the Pythagorean theorem, but by geodesics, and the size of a cell will no longer correspond with $r_c$.

[3] The following arguments can all be extended to the case where $L$ is not divisible by $r_c$, where the number of cells will still be $m^2$, but the size of the cells are $d \times d$ where $d > r_c$ such that $\frac{L}{d} = m$. The choice of $d > r_c$ still ensures that all interactions are limited to particles in the same cell and the directly neighbouring cells.

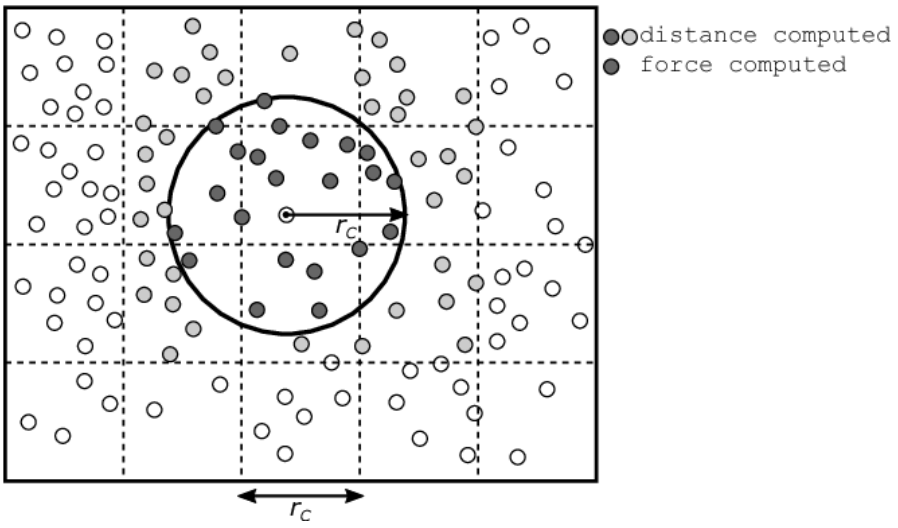


Figure 3.1: Cell list in a flat 2D Euclidean plane, only for particles neighbouring cells is the distance computed, and only for for those distances within $r_c$ the force is computed. The variables of all other particles are completely ignored, saving computation time. Adapted from [33].

(ii) The sphere is simply the geometry of the crystal, but does not correspond to a physical object. Therefore the interaction of the particles is not *screened* by the presence of the sphere, and the cutoff distance $r_c$ hence remains Euclidean.

(iii) The poles are singular points called *topological defects*, which cause the cells to converge to a single point at the poles.

(iv) A mapping using 2 indices will not be sufficient, as this does not allow to differentiate between the 'front' and the 'back' of the sphere. Consider a hemisphere cut in the $z$-axis of a Cartesian coordinate system (i.e. the collection of points $0 < x < R, |y| \leq R, |z| \leq R$). Particles near the cut at $x = 0$ lie within $r_c$ of mirror particles at the other hemisphere with the same $y_a, z_a$ coordinate (corresponding to particle positions $-R < x_a < 0$) whereas particles near $x = R$ are separated by a distance of $\sim 2R$ from mirror particles at the other hemisphere, thus differentiating between the 'front' and 'back' of the sphere is relevant.

The solution to these subtleties is as follows: instead of the physical dimensions of the cell, the angular width $\alpha$ of a cell is used to specify the cell properties. The angular width $\alpha$ corresponds to a cell with the dimensions of $l_r \times l_r$ where $l_r \geq r_c$ is the arc-length of along the cell boundary. Since the sphere is a highly symmetrical object, any cut in the equatorial plane ($z = 0$) or in the polar plane ($x = 0 \vee y = 0$) results in two identical objects. By requiring the numbers of cells in the $i, j, k$ 'directions' to be even, this symmetry will be reflected in the cell listing. Since the surface of the sphere is characterised by two angles $\theta, \phi$ this gives two obvious metrics for assigning the indices. Letting $k$ be assigned based on the azimuthal angle $k$ can be used to distinguish between the 'front' and the 'back' of the sphere (thus choosing for a cut in the polar plane at $y = 0$) by setting

$$k = \lceil \frac{\phi}{2\pi} \rceil. \tag{3.5}$$

Then letting the $i$ be assigned based on the polar angle, the index $i$ can be determined uniquely

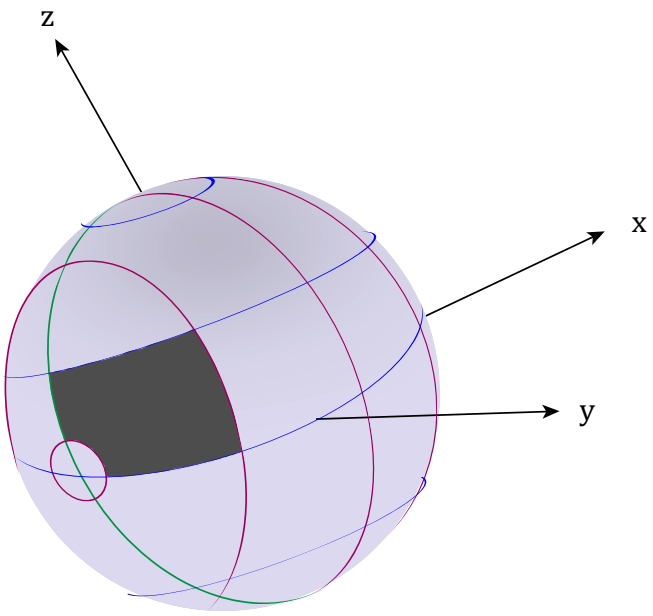


Figure 3.2: Three dimensional representation of the cell listing on the surface of the sphere for $n = 6$. The blue lines correspond to the boundaries of cells with index $i$, the red lines correspond to the boundaries of cells with index $j$, and the green line is the boundary of cells with index $k$. Indicated in dark gray is the cell with index $(3, 2, 1)$.

by

$$i = \lceil \frac{\theta}{\alpha} \rceil, \tag{3.6}$$

representing cuts of the planes $z = C$ with the sphere. Thus $(i, k)$ represents a coupling to the $y, z$ coordinates respectively, and by assigning $i, k$, the $j$ cannot be chosen be independently, since $j$ has to be coupled to the remaining $x$ coordinate. This dependency on $(i, k)$ originates from $x^2 = R^2 - y^2 - z^2$ for a given $y, z$. Interaction with the other side of the sphere (the mirror cell $(i, j, k)$ with different $k$ value) is possible if $(i, j)$ obey

$$\min(i, n - i + 1) + \min(j, n - j + 1) = \frac{n}{2} + 1 \vee \frac{n}{2} + 2 \tag{3.7}$$

where $n$ denotes the number of cells in both the $(i, j)$ 'direction'. For more details about the cell listing on the spherical surface, see appendix E. The resulting cell list of this method is shown in figure 3.2.

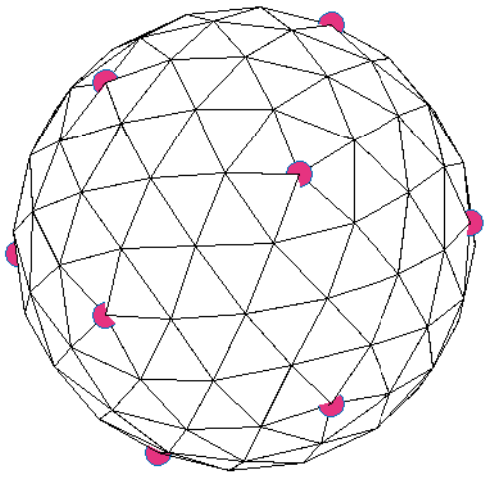

Figure 3.3: The crystal of the smallest simulated magic number configuration of $N = 122$ corresponding to $m = n = 2$ in the Delaunay triangulation of the particle positions (see section 3.5). The 12 five-fold defects are placed perfectly symmetric over the sphere and tagged by a pink marker.

## 3.4 Computational details of simulations

Using the procedures mentioned above, simulations are performed for both randomly initialised starting configurations for $N = 300, 500, 800$ particles, and special magic number configurations of $N = 122, 272, 482, 752$ particles. These magic number configurations have a particle number given by $N = 10(m^2 + mn + n^2) + 2$, which for $m = n$ precisely produce the minimal 12 five-fold defects placed symmetrically and equidistantly over the surface of the sphere [34], see figure 3.3. These magic particle numbers are generated and relaxed in a $r_{ab}^{-12}$ potential in the Thomson applet of Syracuse university [35].

The relaxation could only be performed for a regular power-law potential, where the $r_{ab}^{-12}$ potential is chosen as this most closely resembles the actual WCA used in the simulation. This pre-relaxation is done to investigate the effects of the random initialisation, by comparing the dynamics of passive particles in the absence of thermal fluctuations of these pre-relaxed magic number configurations with randomly initialised configurations of the same number of particles. In all simulations the characteristic scales $\sigma, \epsilon, D_M = 1$ are chosen such that the characteristic time scale $\tau = 1$, the timestep size has been set to $\Delta t = 5 \times 10^{-4}\tau$, and the mobility coefficients have been set to $D_T^\star = D_R^\star = 0.3$. With the exception of the calibration stage, all simulations are performed over a period of $3000\tau$ after equilibration, with the system's state $(\vec{r}_a, \hat{u}_a, \dot{\vec{r}}_a)$ exported as a trajectory for data analysis with intervals of $20\tau$.

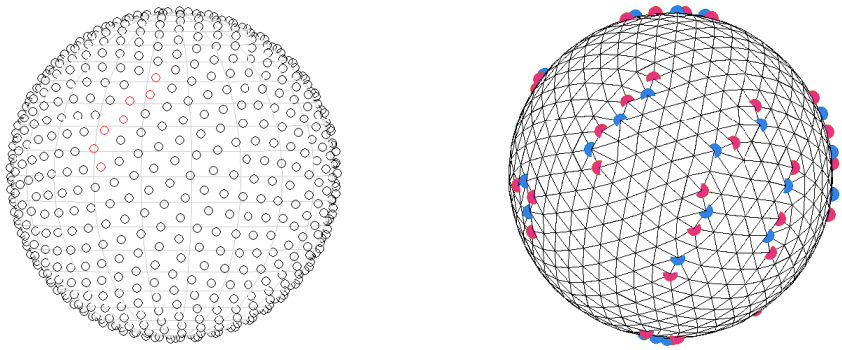

(a) (b)

Figure 3.4: A snapshot of the crystal showing in a) the particle positions, and in b) the resulting Delaunay triangulation, where the vertices of the triangles correspond to particle positions. In b) the five-fold and seven-fold defects are marked by a pink and blue marker respectively. The particles marked in red in a) correspond to the scar of 7 defects Northwest from the equator marked by alternating five-fold and seven-fold defects in b). Comparison of figures a) and b) shows that defects can be visually identified in the crystal by irregular gaps, but are significantly harder to spot than in the triangulation diagram.

## 3.5 Data analysis

Because the main aspects of interests of this research is how temperature and activity influence the properties of the crystal, the structural defects in the lattice, the organisation of defects into scars, the dynamics of particles, and the angular velocity are monitored using the exported trajectories. The latter is monitored in the anticipation of a collective rotation of the crystal when considering active particles.

To measure the structural defects, a Delaunay triangulation is applied to the particle positions $\vec{r}_a$, where each particle $a$ is triangulated with its nearest neighbours [36]. The number of times particle $a$ is then a vertex of a triangle corresponds to the coordination number of particle $a$, and this coordination number allows to identify a particle as a five-fold or seven-fold defect. If a particle is identified as a defect it is given a pink or blue marker for a five-fold and seven-fold defect respectively, which is used for visual inspection of the crystal, see figure 3.4 The number of five-fold defects and seven-fold defects are then measured separately over time, as well as the total number of defects. With the distribution of the defects on the sphere known, an adjacency list of defects is created to determine the lengths of the scars, and the composition of scars is tracked over time by counting the number of scars with lengths ranging from 1 to 10 defects, with a scar of length 1 corresponding to an isolated defect.

With the total numbers of defects known, the crystal could be characterised by the number of defects, but as the number of defects will increase with the number of particles this does not

give a means to compare the effects of activity and temperature for different system sizes [25]. However, the number of defects is still a useful metric for considering the effects of temperature and activity at fixed $N$.To then uniformly quantify the state of the system independent of system size $N$, two order parameters are considered. To measure the degree of crystallinity the global bond orientational order parameter $\psi_6$

$$\psi_6 = \frac{1}{N}\sum_a q_6(a) \tag{3.8}$$

measures the degree of hexagonal order in the system, such that $|\psi_6|$ has a value of 1 for a perfect hexagonal lattice, whereas a completely disordered system without any repeated structure has a $|\psi_6|$ value of 0 [18, 25].
The local bond orientational order parameter $q_6(a)$ in equation (3.8) is defined as

$$q_6(a) = \frac{1}{P}\sum_{m=1}^{P} \exp(i6\theta_{ma}) \tag{3.9}$$

where $P$ is the number of nearest neighbours of particle $a$ and $\theta_{ma}$ is the angle between the bonds of particles $m$ and $a$. The angle $\theta_{ma}$ between the bonds of particles $m$ and $a$ is evaluated in the local tangent plane of the central particle by projecting the neighbour positions $\vec{r}_m$ onto $\mathcal{T}_a$, and taking the local $\tilde{x}$ coordinate as a reference axis, such that $|q_6(a)|$ serves the same purpose as $|\psi_6|$ on the single particle level [37]. To measure the orientational order of the particles the polarisation order parameter $\psi_p$

$$\psi_p = \frac{1}{N}\left\|\sum_a \hat{u}_a\right\| \tag{3.10}$$

measures the degree of alignment of the orientation vectors of all particles, where $\|\cdots\|$ denotes the Euclidean norm of a vector. The polarisation order parameter has a value of 1 if all orientation vectors $\hat{u}_a$ are aligned perfectly and a value of 0 if the orientation vectors are randomly orientated, [13].

To measure the particle dynamics the mean squared displacement (MSD) of each particle $a$

$$\Delta r_a^2(t) = (x_a(t) - x_a(0))^2 + (y_a(t) - y_a(0))^2 + (z_a(t) - z_a(0))^2 \tag{3.11}$$

is tracked over time, and the average mean squared displacement of the system

$$\left\langle \Delta r^2 \right\rangle (t) = \frac{1}{N}\sum_a \Delta r_a^2(t) \tag{3.12}$$

is indicative for the type of process dominating the dynamics. In the ballistic start-up regime $\left\langle \Delta r^2 \right\rangle (t) \propto t^2$, whereas in the diffusive regime where thermal fluctuations have dominated the dynamics $\left\langle \Delta r^2 \right\rangle (t) \propto t$. In the sub-diffusive regime $\left\langle \Delta r^2 \right\rangle \propto t^n$, with $n < 1$, the system starts to quench into its equilibrium state, indicated by a plateau value in $\left\langle \Delta r^2 \right\rangle$ as the particles are trapped in their final crystalline state [38, 37]. To improve the statistics on the MSD, equation (3.11) is evaluated over multiple time origins by shifting the origin from $t_0 = 0$ to arbitrary $t_0$, which represent statistically independent measurement origins. The average over all time origins is then used in the summation of equation (3.12). For larger times, fewer time origins exist for which equation (3.11) can be evaluated, such that the MSD will be less accurate at larger times.

To quantify the degree of collective motion, which due to the tangent constrain cannot manifest as a collective translation, but will be a collective rotation, the normalised angular velocities of the particles ($\hat{\omega_a}$) and the total angular velocity of the crystal ($\vec{\omega}$) are autocorrelated. The angular velocity of a particle $a$ at position $\vec{r}_a$ with velocity $\vec{v}_a$ is

$$\vec{\omega}_a = \frac{\vec{r}_a \times \vec{v}_a}{\|\vec{r}_a\|^2} \tag{3.13}$$

such that the normalised angular velocity becomes

$$\hat{\omega}_a = \frac{\|\vec{r}_a\|}{\|\vec{v}_a\|}\vec{\omega}_a. \tag{3.14}$$

The total angular velocity of the crystal is simply the vectorial sum of the angular velocities of all particles

$$\vec{\omega} = \sum_a \vec{\omega}_a. \tag{3.15}$$

The collective autocorrelation function is defined as

$$C_{col}(\Delta t) = \frac{\langle \vec{\omega}(t) \cdot \vec{\omega}(t + \Delta t) \rangle}{\langle \vec{\omega}(t) \cdot \vec{\omega}(t) \rangle} \tag{3.16}$$

where the time translational invariance property of the autocorrelation is used to express the autocorrelation as function of the delay time $\Delta t$ only, and the average $\langle \cdots \rangle$ denotes averaging over different time origins. For a perfectly coherent rotation about a fixed axis $C_{col}$ retains the constant value of 1 for all delay times [8].
The self-part of the autocorrelation function is defined as

$$C_s(\Delta t) = \frac{\sum_a \langle \hat{\omega}_a(t) \cdot \hat{\omega}_a(t + \Delta t) \rangle}{\sum_a \langle \hat{\omega}_a(t) \cdot \hat{\omega}_a(t) \rangle} \tag{3.17}$$

where again the time translational invariance property of the autocorrelation function has been used. For a perfectly coherent rotation about a fixed axis, particles near the equator have a constant angular velocity throughout the period of rotation, whereas particles at the poles have an anti-correlated angular velocity after a the rotation has performed a half period. Assuming a uniform particle coverage over the sphere and accounting for the difference in particle occupation near the equator and poles, $C_s(\Delta t)$ will perform an oscillation between the values of 1 and 1/3 for a fixed rotation axis [8].

However, as the initialisation process and the thermal fluctuations are completely random, in total 30 simulations are performed over different random seeds. Each random seed corresponds to a statistically independent realisation for the same simulation parameters of particle number ($N$), non-dimensionalised activity ($F$), and non-dimensionalised temperature ($T^\star$). All the above quantities are then evaluated for each of the randomly initialised starting configurations and subsequently ensemble averaged to obtain the true average quantities, which are presented in the next chapter.

# Chapter 4

# Results

In this chapter the results of the lattice defects, scar composition, MSD, correlation functions and order parameters are presented separately for each performed simulation set. Firstly in section 4.1 the effects of the random initialisation is investigated by comparing the pre-relaxed magic number configurations with the randomly initialised configurations for the same number of particles. These calibration simulations are performed on athermal passive particles, corresponding to a zero non-dimensionalised temperature ($T^\star$) and a zero self-propulsion strength ($F$).
Next the results of interest, namely the effects of activity and temperature on the system properties mentioned above, are presented in sections 4.2-4.3, where a distinction is made between active athermal systems (corresponding to $F > 0, T^\star = 0$) to isolate the influence of activity, and non-active thermal system (corresponding to $T^\star = 0, F > 0$) to isolate the influence of temperature.

All plots in this chapter show the data of every $10^{\text{th}}$ trajectory with the errorbars corresponding to 68% uncertainty intervals over the 30 statistically independent starting configurations. An exception to this are the plots for the order parameters, which are either plotted for the full activity or temperature range, where the errorbars have been omitted to increase the clarity of the graphs. As a tradeoff to this, the data has been plotted for all trajectories to increase the smoothness of the graph as the ensemble average is the only information shown.

## 4.1 Calibration

To determine the effects of the random initialisation and the proper equilibration time, simulations of athermal passive particles (corresponding to $F = 0, T^\star = 0$) are performed for both randomly initialised and magic number configurations for $N = 122, 272, 482, 752$ particles. In this context the equilibration time is defined at the time required for the interaction potential to organise the system from a random unphysical initial configuration to an equilibrium configuration. The MSD and number of defects is used as a metric for determining the equilibration time, which both plateau in equilibrium. Despite the fact that the magic number configurations are pre-relaxed, a modest reorganisation is expected as the power-law potential used for relaxation is purely repulsive and has no cutoff.
For the randomly initialised configurations, the total simulation time has been set to $10\tau$. The

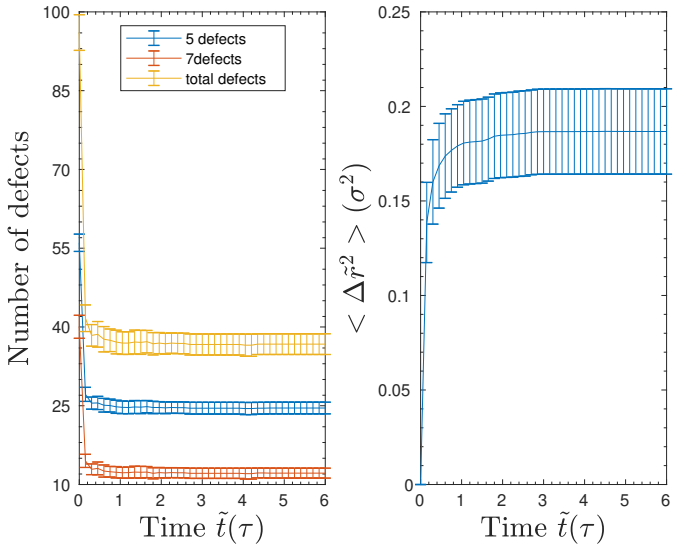


Figure 4.1: Evolution of the number of defects and mean squared displacement in time for the randomly initialised configurations of 272 particles at $F = 0, T^\star = 0$, averaged over 30 independent random seeds, where errorbars correspond to 68% uncertainty intervals.

plot of the average defect number and MSD for randomly the initialised configuration of 272 particles is shown in figure 4.1. Similar results for the randomly initialised configurations for $122, 482, 752$ particles can be found in appendix F.1. From figure 4.1 it can be seen that the plateau in MSD occurs at approximately $2\tau$, which is independent of particle number as appendix F.1 confirms. The universality of relaxation is expected since the potential and cutoff distance are both fixed physical parameters, and for a constant packing fraction roughly the same number of particles will fall within a range of $r_c$ independent of the system size. This relaxation time of $2\tau$ also corresponds to the minimum plateau of the defects, which sets into equilibrium sooner than the particles themselves, since the crystal must first rearrange from its random initial configuration to a state of hexagonal order before it can set into equilibrium.

For the pre-relaxed configurations of particles, simulations are performed for the duration of $2\tau$. The relaxation time is found to be two order of magnitude smaller and roughly $0.02\tau$, see figure 4.2, or appendix F.1. No averaging procedure over different realisations is applied since to these pre-relaxed initial configurations as in for non-active athermal particles the dynamics are completely governed by the particle positions, which for the magic number configurations are fixed over all realisations of independent orientations, and hence the dynamics are completely deterministic. As expected the relaxation time is smaller, but non-zero as the particles are already relaxed in an $r^{-12}$ potential without cutoff, such that at the start of the simulation the strain on the system loosens up corresponding to the observed MSD which is several orders of magnitude lower than in the randomised case.

For comparison, plots of the bond orientational order parameter $|\psi_6|$ for both the randomly initialised configuration and the magic number configuration for 272 particles are shown in figure 4.3. A comparison of figures 4.1-4.2 with figure 4.3 shows that the number of defect is directly related to the bond orientational order parameter, since pentagons and heptagons have significantly small $|q_6|$ values, reducing the overall $|\psi_6|$ value of the crystal. For the randomly initialised configuration $|\psi_6|$ starts at 0.55 and then quickly increases to 0.88 in the same interval as the

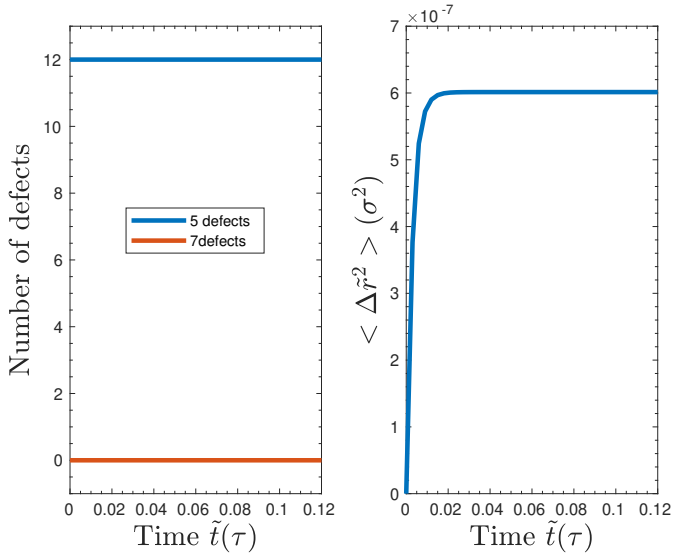


Figure 4.2: Evolution of defects and mean squared displacement for the magic number configuration of 272 particles already equilibrated to an $r^{-12}$ potential. No errorbars are shown as the dynamics for the magic number configuration are completely deterministic in the absence of active self-propulsion or thermal fluctuations. The plot for the total number of defects is not shown as this precisely coincides with the plot of the 5-five fold defects.

total amount of defects decrease from 90 to 38. The non-zero start value of 0.55 indicates that despite the disorder in the initial configuration, the system is tending towards a crystalline structure and hence shows the properties of a solid. For the magic number configuration, $|\psi_6|$ remains virtually constant and only decreases slightly during the first few time steps of the simulation, which can be attributed to the relaxation of the system from a non cut-off $r_{ab}^{-12}$ potential to the WCA potential, as indicated by the non-zero MSD. Both of these values are in perfect agreement with the earlier found value of $|\psi_6| = 0.87$ for densely packed passive particles on a sphere [25].

For all subsequent simulations discussed below, the randomly initialised configurations are equilibrated for $2\tau$ before the simulation run of $3000\tau$ for collecting data begins, and the magic number configurations are equilibrated for $0.02\tau$ before the simulation run for collecting data starts. These equilibration times ensure that the system is relaxed by particle interactions such that the results are only caused by either the active self-propulsion or the thermal fluctuations.

## 4.2 The role of activity

To determine the effects activity has on the system properties, the influence of activity is isolated by performing simulations on athermal active particles, corresponding to $T^\star = 0$ and a range of activity values $F = 0.5, 1.5, 2.5, 3.5$, such that no thermal fluctuations are present. To characterise the effects of activity then, the MSD is used as a metric for the system dynamics, and the structure of the crystal is quantified by monitoring the number of defects, with the added detail of explicitly tracking the composition of the scars. Additionally, the bond orientational order parameter $|\psi_6|$

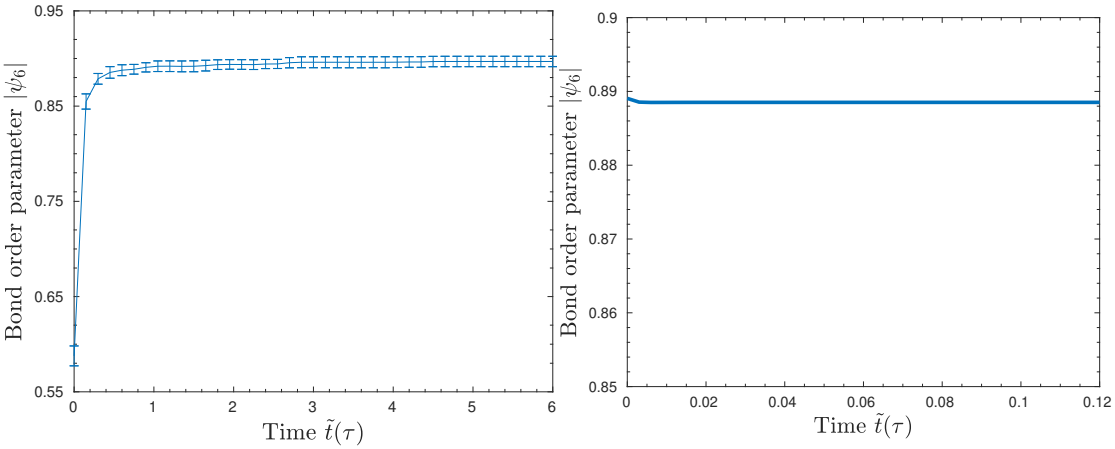


Figure 4.3: Evolution of the bond orientational order parameter $|\psi_6|$ during calibration, for a) the randomly initialised configuration of 272 particles, b) the magic number configuration of 272 particles.

is used to quantify the crystallinity of the system and is used a measure for comparing the effects of low activity and high activity on the crystal.
As activity is considered, the orientation vectors of the particles start to play a role and the polarisation order parameter $\psi_p$ is also tracked to quantify the degree of orientational order. Lastly, to monitor the collective motion property, a mix of the correlation functions and visual inspection of the trajectories is used, where for visual inspection the crystal is observed from a front- and top view to maximise the surface coverage. For the randomly initialised configurations $N = 300, 500, 800$ particles have been simulated where the case of $N = 500$ particles is treated in detail below, and similar results for the other simulations can be found in appendix F.2.

## Defect structure and MSD

The dynamics of the system in terms of the MSD and number of defects are plotted in figure 4.4 for the two extremal cases $F = 0.5$ and $F = 3.5$. In each case the number of defects remains statistically constant. The MSD in the case of low activity shows a smooth sinusoidal pattern characteristic of collective motion, which has a period of roughly $2000\tau$. For the high activity case the MSD is not smooth at all, and after an initial rise performs a small oscillation around the peak value, the reason behind which will be discussed below when considering the collective motion of the crystal. The number of defects remains fixed after an initial decrease, with a gradual but statistically insignificant decrease in defects over time for the high activity case.
A more complete picture of the defect evolution is obtained when also considering the evolution of the scars in the crystal as shown in figure 4.5. Whereas in the low activity case the composition of the scars remain completely frozen, in the high activity case the scar composition slightly changes over time, but remains statistically steady. Visual inspection of the defects in the triangulated lattice does confirm this behaviour where the scars do not noticeably change, except near the rotation axis where closely situated defect dipoles and/or isolated defects can temporarily merge to form a scar of length 3.

The general trend of activity on the crystal is captured in figure 4.6, where the bond orientational order parameter is plotted for all considered values of the activity. The value of $|\psi_6|$ remains virtually constant after a quick increase due to the initial drop in total defects, with a slight increase in the plateau value of $|\psi_6|$ as a result from the gradual decrease in defects over time. Although the increase in $|\psi_6|$ due to activity is a relatively small effect ($\sim 2 - 3 \times 10^{-3}$ increase over a base value of $\sim 0.91$) it it is distinct from numerical noise since its behaviour is smooth and monotonic.

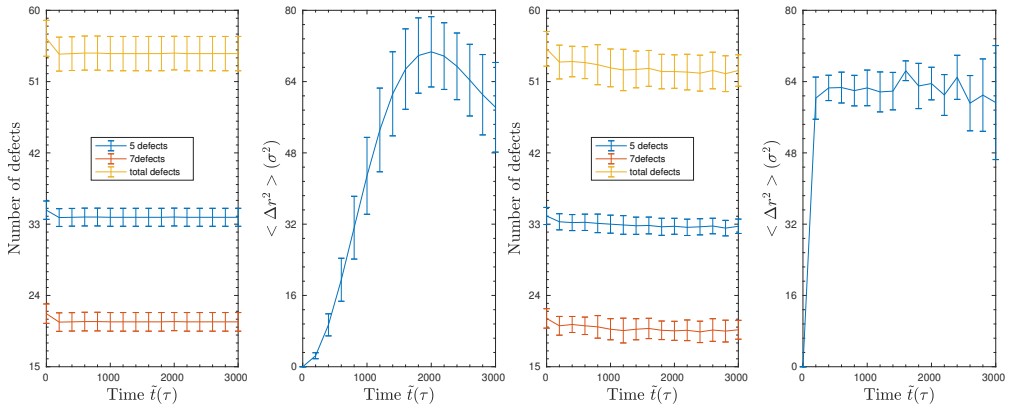


(a) (b)

Figure 4.4: MSD and evolution of the defects for the randomly initialised system of 500 athermal active particles corresponding to $T^\star = 0$ for the extremal cases of a) $F = 0.5$ and b) $F = 3.5$.

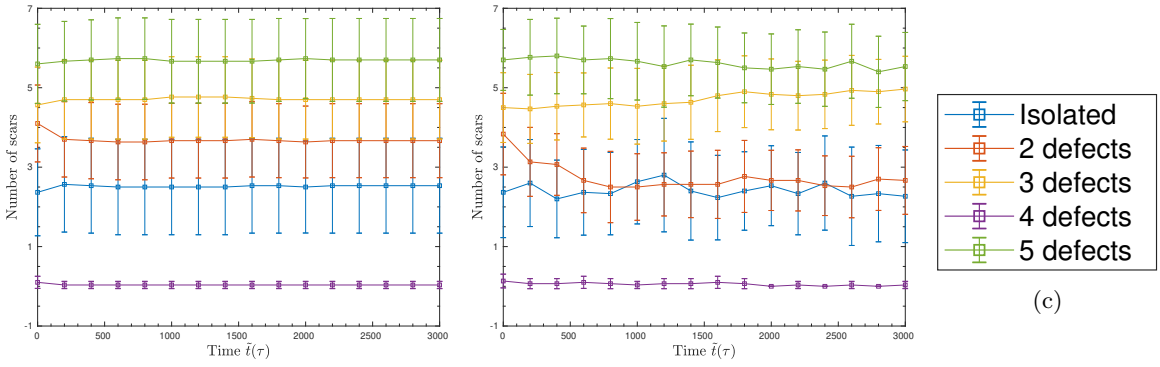


(a) (b) (c)

Figure 4.5: Evolution of the defect scars for for the randomly initialised system of 500 athermal active particles corresponding to $T^\star = 0$ for the extremal cases of a) $F = 0.5$ and b) $F = 3.5$. The legend of figure c) applies to figures a)-b).

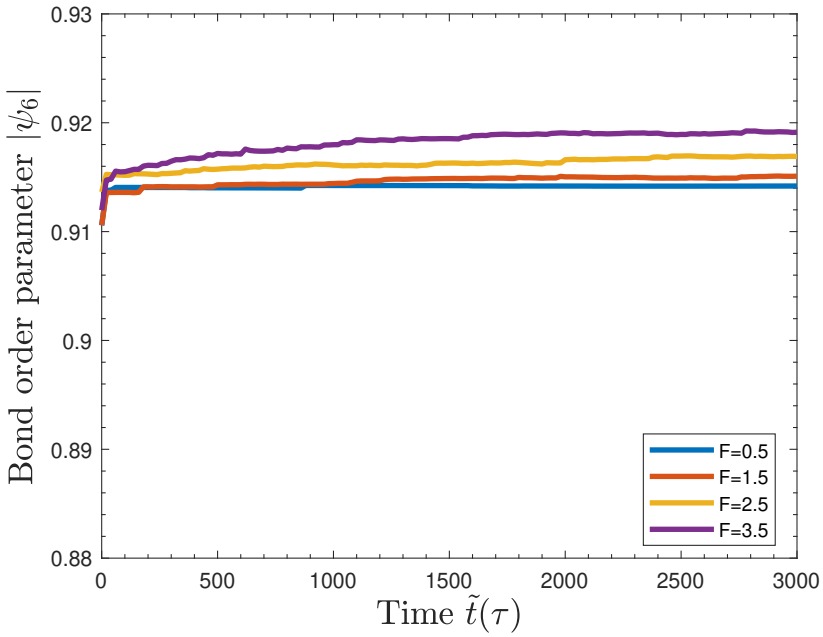


Figure 4.6: The effects of activity on the bond orientational order parameter $|\psi_6|$ for the randomly initialised system of 500 athermal active particles, corresponding to $T^\star = 0$ .

## Collective rotation

The self-propulsion of the particles along their orientation vectors is the key cause of the collective motion property of the crystal. A typical snapshot showing the orientation vectors of the particles in the crystal is shown in figure 4.7a, which shows that the orientation vectors are disordered, corresponding to the random initialisation. The collective motion property is shown in figure 4.7b where the instantaneous normalised angular field $\hat{\omega}_a$ is plotted. Also shown in this figure is the collective angular velocity vector $\vec{\omega}$ indicated by the red arrow in the normalised angular velocity field. The normalised angular velocity in figure 4.7b shows a clear sink, which coincides with the direction of the collective angular velocity, indicating that the angular velocities of the particles organise to perform collective rotation.

However, visual inspection shows this neatly organised rotation is not yet established after the equilibration of $2\tau$, as the first frame still has a relatively disordered angular velocity field. One effect of activity on the self ordering ability of the system is that increasing the activity accelerates the self ordering to a neat collective rotation, as shown in figure 4.8 where the normalised angular velocity field of the first frame for the extremal cases of $F = 0.5$ and $F = 3.5$ are shown. In the low activity case, some disordered aspects are still noticeable in between small domains of locally ordered angular velocities, whereas in the high activity case large domains of local order are clearly visible and the system is close to performing a coherent collective rotation. In both cases the collective angular velocity is also shown as a red arrow, which for the low activity case cannot easily be coupled to the shape of the normalised angular velocity field, unlike the snapshot of figure 4.7b. Even at the lowest considered activity of $F = 0.5$ the normalised angular velocity field at the next trajectory (corresponding to $t = 20\tau$) has the canonical shape of figure 4.7b indicating collective motion.

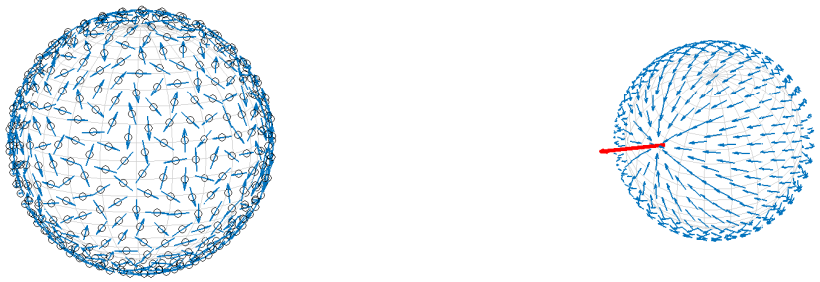

(a) (b)

Figure 4.7: Typical snapshots for the randomly initialised system of 500 athermal active particles showing in a) the particles along with their orientation vector on the sphere, and in b) the instantaneous normalised angular velocity field $\hat{\omega}_a$, where the red arrow indicates the rescaled collective angular velocity vector $\vec{\omega}$. A rescaling has been applied to the collective angular velocity vector to ensure its magnitude is larger than the radius of the sphere such that it always points out of the surface of the sphere and is not concealed inside the sphere.

However, figure 4.7b should be interpreted with care, as the angular velocity field implies a consistent rotation about a fixed axis, but this is a misleading conclusion. Visual inspection of the trajectories shows that neither the rotation axis, nor the magnitude of $\vec{\omega}$ remain fixed. Instead $\vec{\omega}$ translates over the sphere, changing the direction of the rotation axis, and the rotation speed fluctuates between relatively fast and slow rotations corresponding to changes in magnitude of $\vec{\omega}$. This behaviour is shown in figure 4.9, where $\vec{\omega}$ has been plotted for multiple frames of a single realisation, both for the extremal cases of $F = 0.5$ and $F = 3.5$. As $\vec{\omega}$ has not been rescaled in these plots, the arrow lengths directly represent the rotation speed, and vector directions represent the location of the rotation axes. Since the trajectories are snapshots of the system's state at equally spaced intervals of $20\tau$, the density of arrows is a measure for the stability of a rotational state. From figure 4.9 it can be seen that the system goes through a multitude of rotation states, and never reaches a true equilibrium state where $\vec{\omega}$ remains fixed. For the low activity case $\vec{\omega}$ has gradually changes in magnitude and translates over the surface of the sphere at a moderate and smooth rate, such that $\vec{\omega}$ sweeps out a cone. For the high activity case $\vec{\omega}$ shows drastically different behaviour, although traces of this *coning* are still present, $\vec{\omega}$ both increases and decreases in magnitude and even switches sign in one or multiple components. This non-steady behaviour of $\vec{\omega}$ is intriguing since the simulations are performed for athermal active particles, such that thermal fluctuations which would intuitively be the first cause for the changes in $\vec{\omega}$ are not present. All the observed dynamics of the collective rotation is due to the active self-propulsion of each particle and the particle interactions, which aside from the random initialisation of the orientation vectors is completely deterministic.

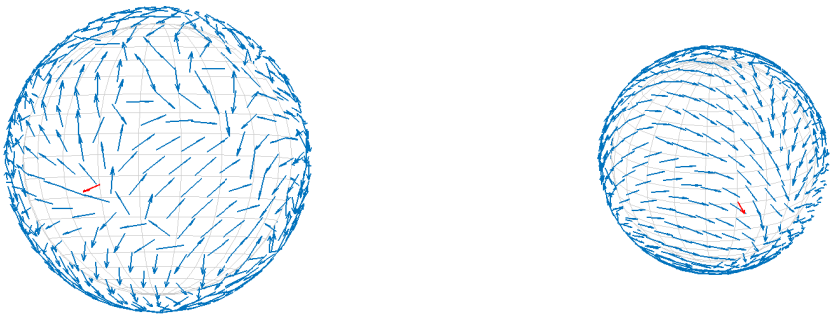

(a) (b)

Figure 4.8: Normalised angular velocity field at the first frame (corresponding to $t = 0$ after equilibration) of a single realisation of the random initialisation of 500 athermal active particles (corresponding to $T^\star = 0$) for the extremal cases of a) $F = 0.5$, and b) $F = 3.5$. The red arrow indicates the rescaled total angular velocity $\vec{\omega}$, where rescaling ensures that the vector can point out of the spherical surface.

## Correlation functions

The correlation functions for the angular velocity provide a means to quantify these observed dynamics in the angular velocity, and differentiate between the low and high activity cases. The correlation functions for the extremal cases of $F = 0.5$ and $F = 3.5$ are shown in 4.10, where the difference between low and high activity is clearly visible. For the low activity case of $F = 0.5$ the statistical average of the collective correlation function $C_{col}(\Delta t)$ remains 1 for long time delays, up until $2500\tau$, where a small decrease occurs due to the small window of time origins over which can be averaged. The self part of the correlation function $C_s(\Delta t)$ initially follows the predicted oscillation between the values of 1 and 1/3 for a steady rotation, but plateaus near the value of 1/2. At the largest time delays, $C_s$ shows a decrease for the same reasons as mentioned above. For the high activity case the collective correlation decreases to 0 over time, due to the high translational rate which causes $\vec{\omega}$ to cover a vast majority of the surface of the sphere, causing $\vec{\omega}$ to become uncorrelated with its past if averaged out over independent realisations, as $\vec{\omega}$ can be thought of performing a quasi-random walk over the surface of the sphere. For short time delays, $\vec{\omega}$ does show a correlation with its past as a result of the *coning* effect during periods of steady translation rate and relatively constant magnitude. The striking increase in uncertainty of the collective correlation function over time arises from the definition of the collective correlation function from equation (3.16). Unlike the $\hat{\omega}_a$ which are normalised at each timestep such that only the direction of the $\hat{\omega}_a$ influences the value of $C_s(\Delta t)$, the collective correlation function depends on the dot product of $\vec{\omega}$ with its future incarnations which unlike $\hat{\omega}_a$ do not have a fixed magnitude. As shown in figure 4.9 the magnitude of $\vec{\omega}$ for small time delays is virtually constant, but for long time delays can be differ significantly. Since each realisation is independent and develops a different evolution of $\vec{\omega}$ this results in an increasing variance over time. Although for longer delay times, the decrease in available time origins for averaging is also a source of increased uncertainty, but this alone cannot cause the significant growth of the uncertainty in between small and intermediate delay times.

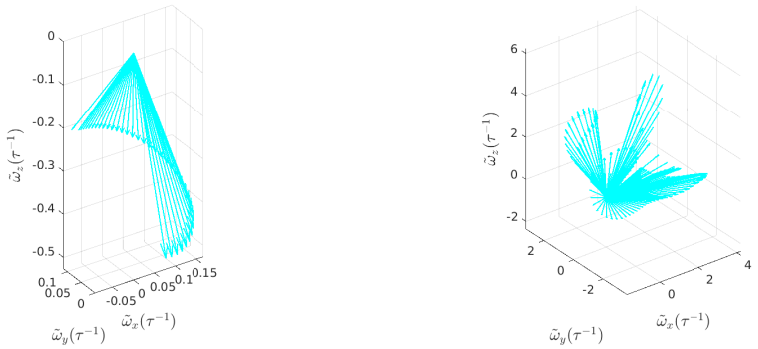


(a) (b)

Figure 4.9: The collective angular velocity vector $\vec{\omega}$ of each trajectory plotted from the origin for a single realisation of randomly initialised system of 500 athermal active particles (corresponding to $T^\star = 0$) and activity of a) $F = 0.5$, and b) $F = 3.5$. To increase the visibility only 1 in every $4^{\text{th}}$ vector has been plotted in a), whereas b) shows $\vec{\omega}$ for all trajectories.

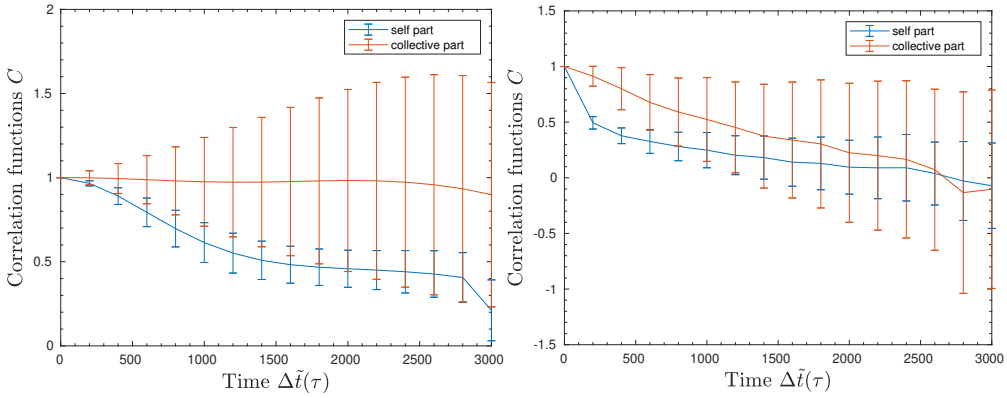


(a) (b)

Figure 4.10: Autocorrelation functions for the collective rotation and normalised angular velocities of individual particles for the randomly initialised system of 500 athermal active particles (corresponding to $T^\star = 0$), shown for the extremal cases of a) $F = 0.5$, and b) $F = 3.5$.

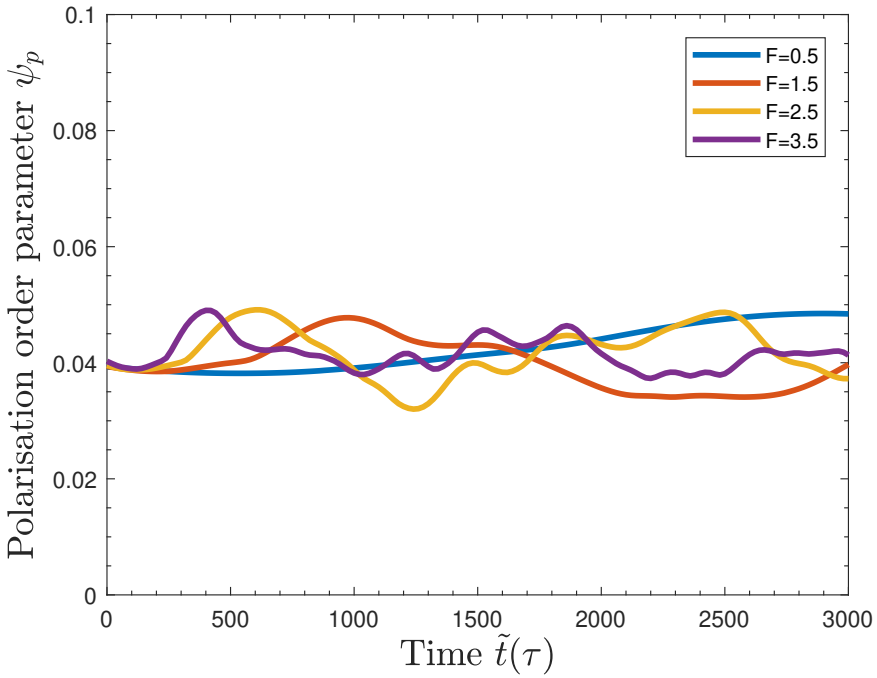


Figure 4.11: The evolution of the polarisation order parameter $\psi_p$ over time as a function of the active self-propulsion strength for the system of 500 athermal active particles (corresponding to $T^\star = 0$).

As the simulations are performed for athermal active particles, rotational Brownian motion caused by the angular kicks from equation (2.9b) cannot explain the observed translational behaviour of the rotation axis on the sphere. This is further emphasised by the polarisation order parameter $\psi_p$, which remains virtually fixed at a value of 0.04, see figure 4.11. The near zero value of $\psi_p$ indicates a disordered orientation field consistent with the random initialisation and the snapshot of figure 4.7a. The fluctuations in $\psi_p$ are numerical noise resulting from the projection of the orientation vectors onto the sphere during the rotation, since $\hat{u}_a$ must lie in the tangent plane of each particle, slightly altering its Cartesian components. All the dynamics occur under the influence of the active self-propulsion in the 'frozen-in' direction of the initialised orientation vector [4] and the interaction forces. An exchange in particle positions could explain the translation of the rotation axis as the orientation field changes under particle swaps, but are unlikely as the repulsive interaction force will prevent particles from approaching each other and crossing paths. Simulations for a small system of 50 athermal active particles confirm that such particle swaps do not occur.

The active self-propulsion force however, can the cause of the gradual changes in the angular velocity field, as the addition of the self-propulsion force will frustrate the lattice since the directions of the self-propulsion forces are randomised. In the absence of any self-propulsion the crystal forms a primarily ideal hexagonal lattice with the repulsive interaction forces balancing out on each particle, see figure 4.12a.

[4] Frozen-in refers in this context to the direction of the orientation in the local tangent plane, not to the Cartesian components of the orientation vector which are subjected to small changes as a result from the projection onto the tangent plane.

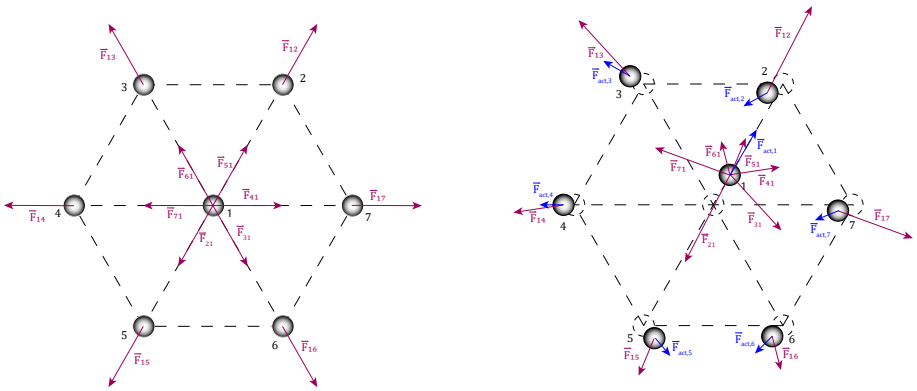

(a) (b)

Figure 4.12: Force balance for a single hexagonal unit in the crystal, where for simplicity only the pair interaction forces involving the central particle are shown. The dotted lines denote the ideal hexagonal unit positions and distances, portrayed are: a) the passive system at $T^\star = 0$, and b) its active counter part.

If activity is now added and each particle exerts an additional constant self-propulsion force in an arbitrary direction, the force balance of this ideal hexagonal lattice will be broken, and the particles will propagate in the direction of the self-propulsion force. This propagation cannot continue indefinitely as the repulsive interaction force between particles will grow as they approach each other, whereas their active self-propulsion forces remains constant. A new force balance will then be reached at slightly displaced positions and angles with respect to the ideal hexagonal lattice, see figure 4.12b. This new equilibrium configuration is more fragile than the equilibrium situation of the ideal hexagonal lattice due to the random nature of the direction of the self-propulsion forces of each particle, as each particle must find its new equilibrium position with respect to the particles within its cut-off radius, which each has a self-propulsion force in an arbitrary direction. The addition of activity thus frustrates the lattice since it cannot occupy its preferred stable equilibrium configuration dictated by the repulsive WCA interaction, but instead must compensate for all active forces of nearby particles. Visual inspection of the trajectories shows that as a result of these frustrations the lattice vibrates as small displacements are visible in the triangulation diagram for low activity which corresponds to slowest dynamics. These lattice vibrations then introduce small deviations from the ideal normalised angular velocity field for a constant collective angular velocity $\vec{\omega}$ which explains the gradual translation of the rotation axis as observed.

## Interplay of defects and rotation axis

Interestingly, and unexpectedly, it is found that the axis of rotation tends to be attracted towards the defects and scars in the crystal. By careful visual inspection of the trajectories the following observations are made:

O.1 The rotation axis is stabilised by defect structures. The rotation axis tends to stay close to scars after the rotation axis has coincided with on the defects in the scars, as opposed to the steady translation which occurs if the rotation axis is at a regular part of the lattice.

O.2 Likewise scars can stabilise the rotation axis in between them. If the rotation axis approaches equally sized and shaped scars (e.g. 2 scars of length 3 as a linear chain like the water molecule rather than forming a closed triangle) the rotation axis is stabilised in the centre of gravity of these identical scars. If the symmetry of this situation is broken, then the rotation axis is not stabilised at the centre of gravity of these identical scars, but moves towards one of these scars, or moves on to translate over the defect-free part of the lattice.

O.3 If the rotation axis approaches an area containing multiple closely situated scars, it has the tendency to move towards the largest of these scars.

O.4 The rotation axis prefers symmetric scars. If the rotation axis approaches an area with multiple scars of the same length, but with a different shape, then the rotation axis tends to move towards the most symmetric of these scars.

O.5 The translational rate of the rotation axis on the sphere is proportional to the magnitude of the angular velocity. This behaviour is intuitive to understand as a larger magnitude of the collective angular velocity corresponds to faster dynamics on the sphere, where the translation of the rotation axis is a clear dynamic effect.

O.6 Islands of closely situated isolated defects can be turned into defect scars as the rotation axis passes through these islands of isolated defects. However the additional scars created by this mechanism are not stable and dissolve back into the island of closely situated isolated defect they originated from, some time after the rotation axis has moved away from the newly formed scar. This behaviour results in the measured fluctuations of isolated defects observed in the high activity case of figure 4.5.

O.7 The stabilisation of the rotation axis is never permanent. The rotation axis does not stick at a scar forever, but will eventually disconnect from the scar and continue to translate over the defect-free area of the crystal until it is stabilised again by another scar.

A movie for a simulation at an intermediate activity of $F = 2.5$, such that the dynamics are fast enough to show multiple of these observations but not too fast such that translations dominate over the stabilisation effects by scars, is available on YouTube via `https://youtu.be/dMgyvnp7S2s`, which shows the triangulated lattice with the rotation axis indicated by a red arrow, and the normalised angular velocity field.

## Specialities for the magic number configurations

For the magic number configurations $122, 272, 482,$ and $752$ athermal active particles have been simulated at $T^\star = 0$ and for the same range of activity values as the randomly initialised configurations. The case of 482 particles is compared in detail to the randomly initialised case below, with similar results for $122, 272, 752$ particles available in appendix F.2.
On the contrary, for the magic number configurations, activity does not have any effect on the number defects or the crystallinity. Even up to the highest considered activity of $F = 3.5$ the total number of defects remained the 12 original five-fold defects. This is also reflected in the behaviour of the bond orientational order parameter $|\psi_6|$ which remains identically constant for all considered activity values, see figure 4.13.
The MSD follows a similar trend of transforming from a smooth oscillation to an inconsistent oscillation about an initial peak value, see figure 4.14. The identical behaviour of MSD at increased activity implies that $\vec{\omega}$ behaves in an identical manner with *coning* behaviour and changes in

magnitude. However the collective correlation function does not show completely identical behaviour to the randomly initialised case, see figure 4.15. This shows that the collective motion property of the system does not simply depend on the strength of the active self-propulsion force but is also dependent on the particle positions, since in both cases the strength of the self-propulsion is equal and the orientation vector of each particle is randomised according to the same protocol as described in chapter 3.
This difference in behaviour can be understood by realising that the observations discussed above involve the behaviour of $\vec{\omega}$ near scars, which are absent for the magic number configurations, where only isolated defects occur. Observations O.1 O.2 O.4 still remain applicable to describe the behaviour of $\vec{\omega}$ for the magic number configurations. Careful visual inspection of the trajectories shows these observations are indeed maintained and that the following observation can encapsulate all of these observations for the magic number configurations:

MO.1 The rotation axis is stabilised in the centre of gravity of the equidistant defects. This stabilisation occurs either in the centre of gravity of the triangle spun by 3 isolated defects or the centre of gravity of the diamond spun by 4 isolated defects. However just for the randomly initialised case, these stabilisations are never permanent and the

A movie for a simulation at an intermediate activity of $F = 2.5$, such that the dynamics are fast enough to show this observation but not too fast such that translations dominate over the stabilisation effects by defects, is available on YouTube via `https://youtu.be/f6H24CWkKwc` which shows the triangulated lattice with the rotation axis indicated by a red arrow, and the normalised angular velocity field.

Lastly the effect of activity on the polarisation order parameter for the magic number configuration of 482 particles is shown in figure 4.16, which shows practically identical behaviour to its random counterpart of 500 particles, with a slightly higher initial value, which is a result of the decreased system size.

## Summary

Overall, the role of activity for athermal systems can be summarised as follows:

i Activity has a negligible effect on the number of defects and scar composition, although for the randomly initialised configurations a marginal and gradual decrease in the number of defects occurs at high activity, corresponding to the marginal increase in the bond orientational order parameter $|\psi_6|$. The degree of crystallinity of the system thus remains statistically constant when activity is increased.

ii Activity causes the spherical to perform a collective rotation, where the speed of the dynamics is proportional to the strength of the self-propulsion force.

iii The rotational dynamics has an interesting interplay with the scars in the crystal, where the scars seem to function like an attractor for the rotation axis.

iv Due to the increase in the speed of the dynamics as activity increases and the attraction of the rotation axis by the scars, the collective angular velocity is correlated at low activity, but decorrelates over time at high activity.

v The correlated angular velocity at low activity corresponds to a smooth sinusoidal MSD, but at high activity the decorrelation of the angular velocity leads to an initial increase of MSD after which the MSD oscillates about this peak value.

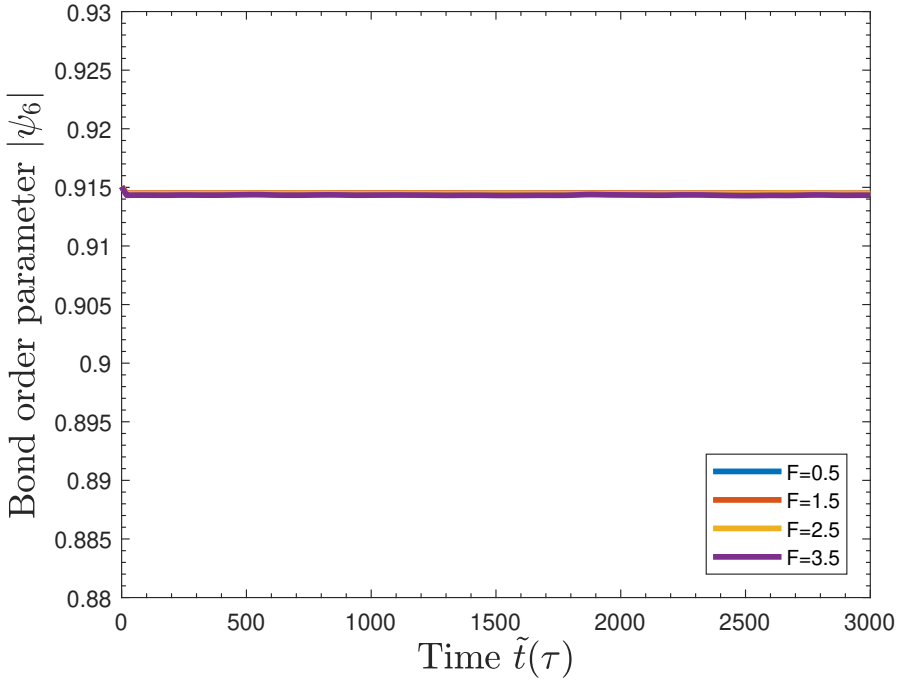


Figure 4.13: Evolution of the bond orientational order parameter $|\psi_6|$ as a function of activity for the magic number configuration of 482 athermal active particles (corresponding to $T^\star = 0$).

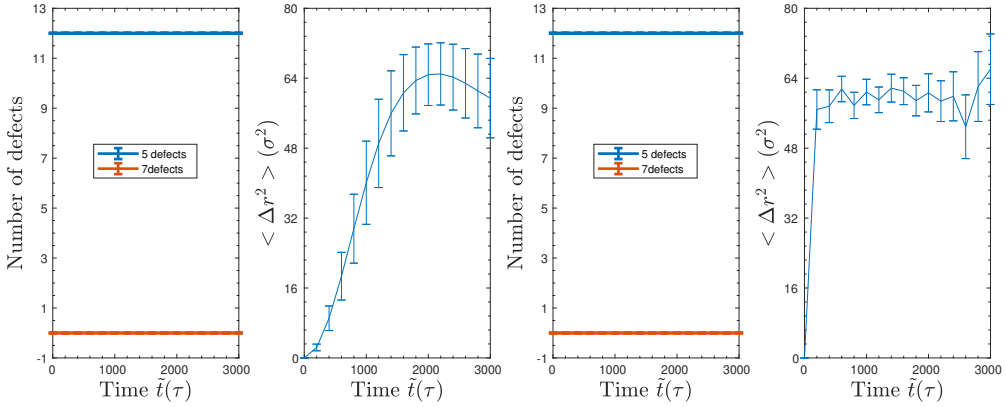


(a) (b)

Figure 4.14: Number of total defects and MSD for the magic number of 482 athermal active particles (corresponding to $T^\star = 0$) for the extremal cases of a) $F = 0.5$, and b) $F = 3.5$.

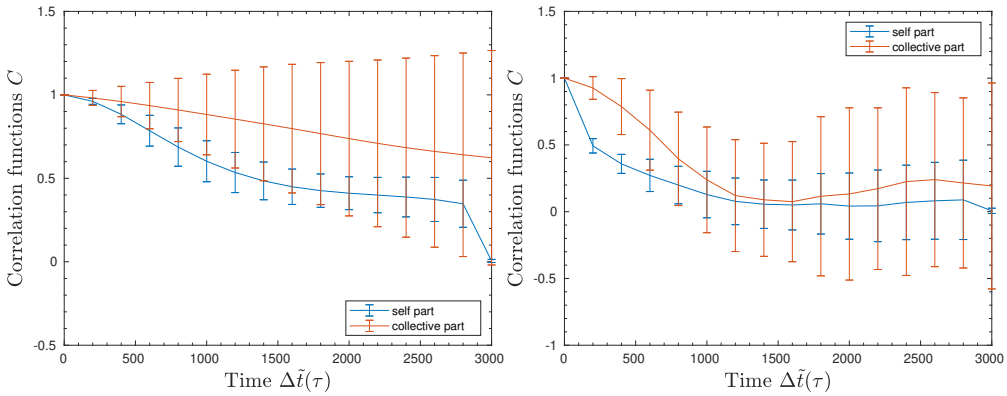


Figure 4.15: Autocorrelation functions for the collective rotation and normalised angular velocities of individual particles of the magic number configuration of 482 athermal active particles (corresponding to $T^\star = 0$), shown for the extremal cases of a) $F = 0.5$, and b) $F = 3.5$.

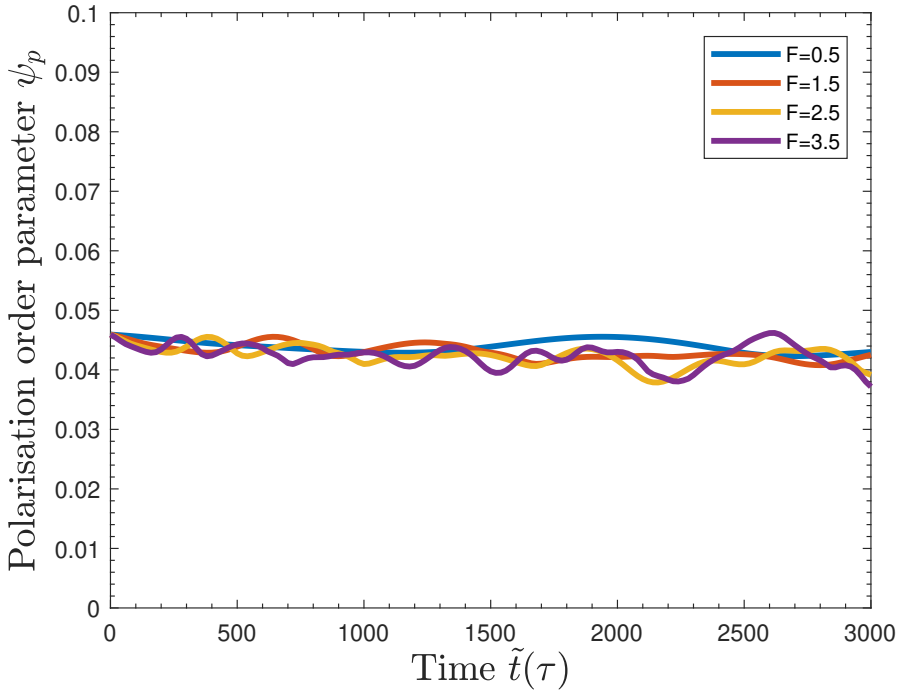


Figure 4.16: Effect of activity on the polarisation order parameter $\psi_p$ for the magic number configuration of 482 athermal particles (corresponding to $T^\star = 0$).

## 4.3 The role of temperature

To determine the effects temperature has on the system properties, the influence of temperature is isolated by performing simulations on Brownian passive particles, corresponding to $F = 0$ and a range of temperature values $T^\star = 0.5, 1.0, 1.5, 2.0, 2.5$, such that no self-propulsion is present. To make a fair comparison between the effects of activity and temperature the same metrics, namely the MSD, total number of defects, the composition of scars, correlation functions and order parameters are tracked over time to quantify the system's dynamics and crystalline structure. The polarisation order parameter $\psi_p$ does not have the same physical meaning as it does for activity, but since each particle has been initialised with an orientation vector according to the method discussed in chapter 3, $\psi_p$ is a useful tool for measuring the effects of the angular diffusion in equation (2.15). Analogous to the simulations for active athermal particles, visual inspection of the trajectories is performed from both a top and front view of the sphere to support these findings on a visual level. For the randomly initialised configurations $N = 300, 500, 800$ particles have been simulated, where the case for 500 particles will be discussed in detail below, and similar results for the other simulations can be found in appendix F.3.

### Correlation functions

In stark contrast to the activity simulations, no collective motion emerges for passive Brownian particles, which is quantised by the time dependent normalised angular velocity field and the trace the collective rotation vector $\vec{\omega}$ sweeps out over time, see figure 4.17. The normalised angular velocity field $\hat{\omega}_a$ is completely unorganised and shows no signs of collectivity or domain forming, with the resulting collective rotation vector $\vec{\omega}$ pointing in a random direction with respect to the normalised angular velocity field. The different rotation states swept out by $\vec{\omega}$ over time further illustrates the randomness of $\vec{\omega}$, which spans out a vast majority of different directions, forming a sphere of uniform occupancy, with no signs of the observed *coning* behaviour present during the activity simulations. The random uniform nature of $\vec{\omega}$ is perfectly captured by the correlation functions, which are both practically zero for all time delays with sufficient time origins for reasonable averaging. The correlation functions attain the value of 1 at zero time delay, since any vector is perfectly correlated with a copy of itself, see figure 4.18. This is also confirmed by visual inspection of the trajectories, which shows that the crystal on the sphere performs jerky movements, as a result of the net random kick of all particles, which correspond to small, but uncorrelated, rotations because the motion is confined to the surface to the sphere. Since this random behaviour occurs for both randomly intialised configurations and magic number configurations, further results about the correlation functions are not shown.

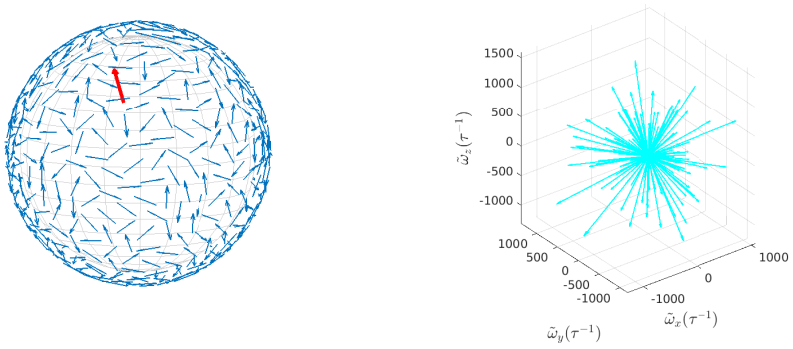


(a) (b)

Figure 4.17: Typical snapshots for the behaviour of the angular velocities for the randomly initialised system of 500 passive Brownian particles (corresponding to $F = 0$), showing a) the normalised angular velocity field with the red arrow indicating $\vec{\omega}$, and b) the collective angular velocity vector $\vec{\omega}$ of each frame plotted from the origin.

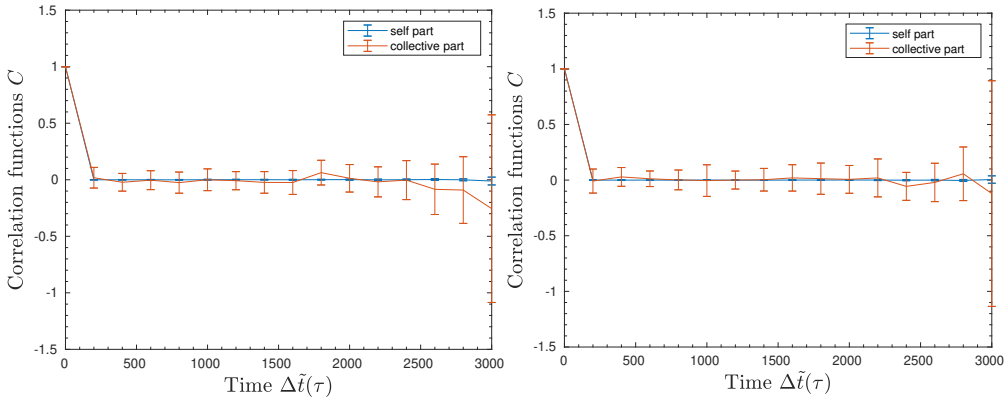


(a) (b)

Figure 4.18: Correlation functions for both the individual normalised angular velocities and the collective angular velocity for the randomly initialised system of 500 passive Brownian particles (corresponding to $F = 0$) , for the extremal cases of a) $T^\star = 0.5$, and b) $T^\star = 2.5$. The growth in uncertainty for the delay time of $\Delta\tilde{t} = 3000\tau$ is due to a lack time origins for averaging, such that the statistics are only over a single time origin for the 30 independent realisations.

## Defect structure and MSD

The effects of temperature on the crystal are once again monitored by the total defects, scar composition and the bond orientational order parameter. For the randomly initialised configurations the total number of defects shows a decrease as temperature increases, and for all temperatures the curve of the MSD starts off linearly according to the diffusion driven regime, but eventually subdues to the sublinear regime as a result of the restoring force of the potential, see figure 4.19.

A clear trend in the increase of the MSD with increasing temperature is visible, corresponding to greater thermal fluctuations. This behaviour is directly noticeable in the visual inspection of the trajectories, where the paths of some tagged particles have been trailed, showing a clear increase in the surface patch traced out by these tagged particles, see figure 4.20. For low temperatures the tagged particles have very weak diffusion and practically leave circular traces around their initial positions. At higher temperatures the shape of traces loses its regular character with the random walk feature becoming more prevalent, and the traces significantly increase in area.

The statistically significant decrease in the total number of defects shown in figure 4.19 is also reflected in the scar compositions, where increasing the temperature results in the promotion of smaller scars of length 3 at the cost of larger scars of length 5 and 7, see figure 4.21. These scar compositions also show that isolated defects are not favourable, as these are quickly converted to scars of length 3 by the thermal fluctuations of the lattice surrounding them. These scar dynamics follow from the requirement of the Euler characteristic that there must be a net topological charge of $+2$ on the sphere, corresponding to 12 five-fold defects. As scars of an odd length always have one excess five-fold defect over the seven-fold defects, they correspond to a net topological charge of $+1/6$ identical to an isolated defect, whereas defect dipoles contribute a net topological charge of zero and do not contribute at all to screen the curvature, making them highly unfavourable. Although figure 4.21 is a useful and accurate statistical representation of the scar dynamics, it does not encompass the complete scar dynamics. Visual inspection of the trajectories show that under the influence of fluctuations the lattice is continuously stretching and compressing the hexagonal, pentagonal and heptagonal units which results in a reshaping of the scars. Since both five-fold and seven-fold defects disrupt hexagonal order, the hexagonal units close to a scar will be slightly stronger deformed, which in combination with the stretching and compression from thermal fluctuations can cause the defect to 'hop' from one particle to one of its neighbours in the deformed hexagonal unit. This effectively does not contribute to a decrease or increase in the number of scars, but a change in orientation of the scar. For the larger scars (of length 5 and up) reshaping is not the only response to the fluctuations, but the scars can also break up into smaller scars, often dissolving into defect dipoles or isolated defects. If two scars are located closely next to each other, the preference of the system for scars of length 3 and 5 allows for a fusion of these detached *subscars*, thus resulting in an exchange of defects between scars. These effects are illustrated in figure 4.22, which shows the lattice of 3 subsequent trajectories and displays the dissolving and reshaping behaviour of the scars. The scar of length 5 shown near the equator initially consist out of a $5-7$ defect dipole and scar of length 3, which then merge to form a linear stretched out scar of length 5, and then reshape to a more compact form consisting of a closed triangle with 2 attached 'limbs' of 1 defect long at each side. The scar of length 3 beneath the equator on the other hand, only changes its orientation but does not reshape of dissolve at all, since these are the smallest possible scars.

## Order parameters

Overall, despite the decrease of the number of defects for increasing temperature, which results in an increase in the bond orientational order parameter, $|\psi_6|$ monotonically decreases as temperature increases, see figure 4.23. This decrease in $|\psi_6|$ can be attributed to the other effects caused by thermal fluctuations, namely the constant reshaping of the scars, the additional deformations a scar imposes on its neighbouring hexagonal units, and the overall increase of thermal fluctuations throughout the crystal. All these factors lead to stronger deformations of the hexagonal units which in turn lower $|\psi_6|$.

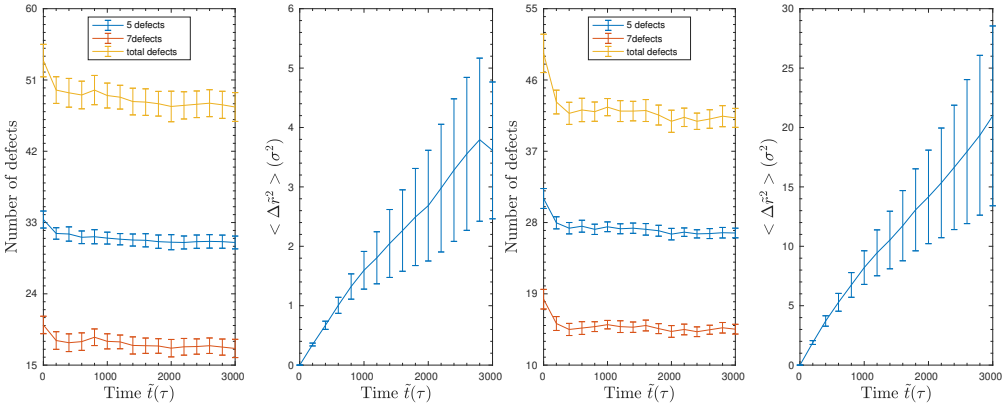


(a) (b)

Figure 4.19: The evolution of the MSD and total number of defects for the randomly initialised system of 500 passive Brownian particles (corresponding to $F = 0$) and the extremal cases of a) $T^\star = 0.5$, and b) $T^\star = 2.5$.

Lastly, the polarisation order parameter $\psi_p$ is virtually zero as a result from the random initialisation, with small chaotic fluctuations caused by the random angular kicks, confirming that random kicks can neither increase nor decrease the order of particle orientations, see figure 4.24.

A movie for a simulation at a intermediate temperature of $T^\star = 1.5$, is available on YouTube via `https://youtu.be/M2kcy342osI` which shows the triangulated lattice, and the corresponding particles on the sphere, where some particles have been tagged and their paths have been traced. In this movie the thermal fluctuations over the whole lattice and the reshaping/reorientation of the scars is clearly visible in the triangulation diagram, along with the jerky rotation of the sphere.

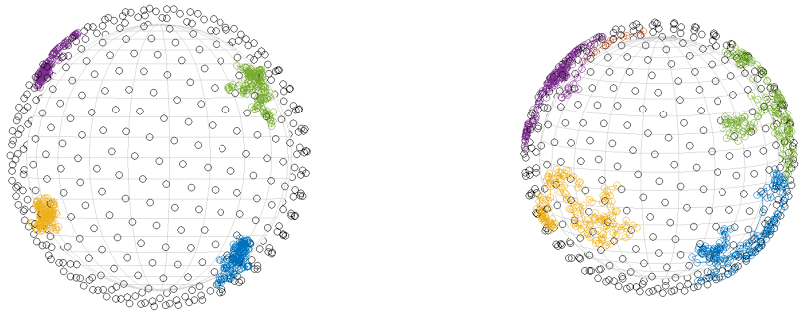

(a) (b)

Figure 4.20: Paths traced by the tagged by the tagged particles of a single realisation for a randomly initialised system of 500 passive Brownian particles (corresponding to $F = 0$), for the extremal cases of a) $T^\star = 0.5$, and b) $T^\star = 2.5$.

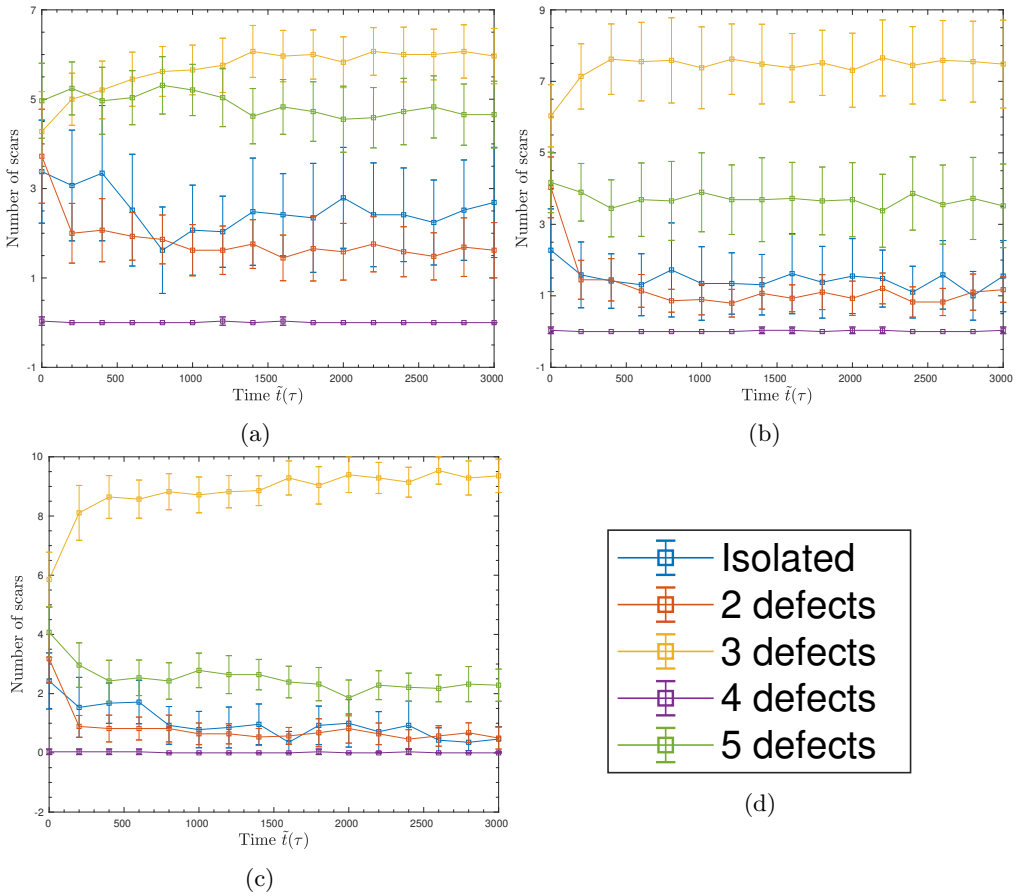


Figure 4.21: Evolution of the scar composition over time for the randomly initialised system of 500 passive Brownian particles (corresponding to $F = 0$) for temperatures of a) $T^\star = 0.5$, b) $T^\star = 1.5$, and c) $T^\star = 2.5$. The legend of figure d) applies to figures a)-c).

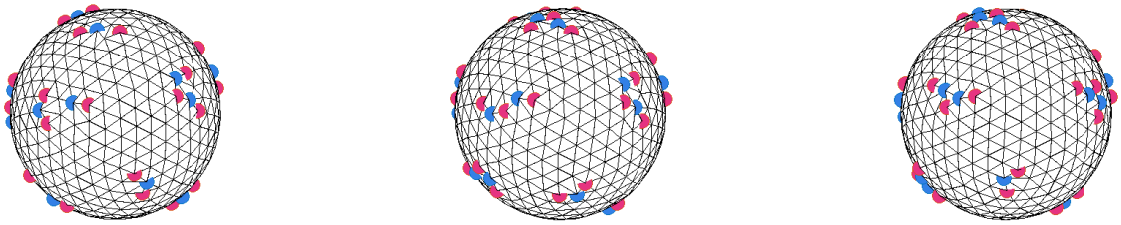

Figure 4.22: Snapshots of the triangulation of the diagram for 3 subsequent trajectories of a realisation for randomly initialised 500 passive Brownian particles (corresponding to $F = 0$),with a time difference of $20\tau$ in between snapshots.

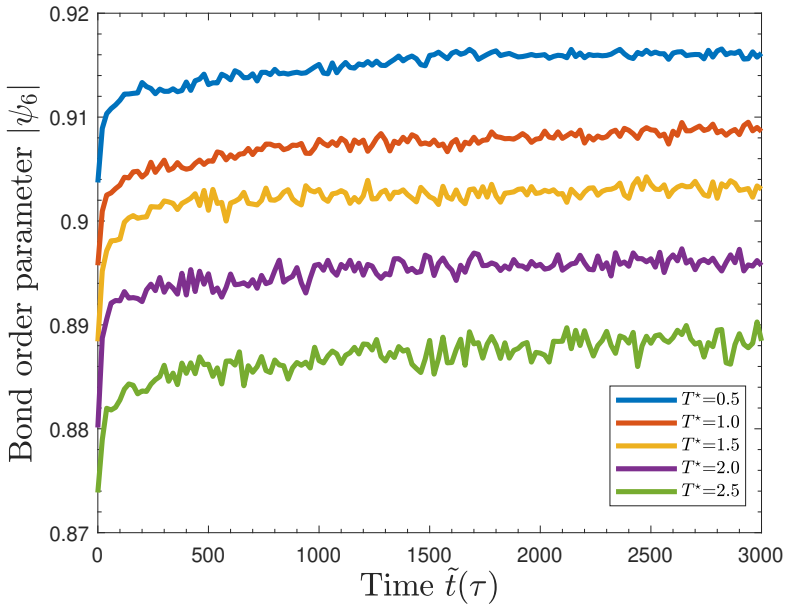


Figure 4.23: Evolution of the bond-orientational order parameter $|\psi_6|$ for the randomly initialised system of 500 passive Brownian particles (corresponding to $F = 0$) as a function of temperature. The initial increase at short times is due to the steep decrease in total defects shortly after equilibration.

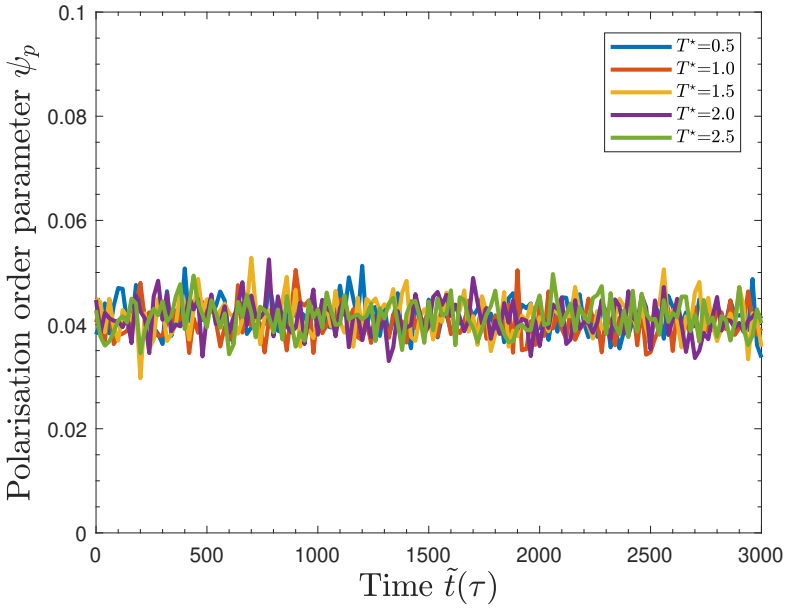


Figure 4.24: Evolution of the polarisation order parameter $|\psi_p|$ for the randomly initialised system of 500 passive Brownian particles (corresponding to $F = 0$) as a function of temperature.

## Specialities for the magic number configurations

For the magic number configurations $122, 272, 482,$ and $752$ passive Brownian particles have been simulated at $F = 0$ over the same range of temperature values as the randomly initialised configurations. The case of 482 particles is compared to the randomly initialised case of 500 particles below, with similar results for $122, 272, 752$ particles available in appendix F.3.
For the magic number configurations the influence of temperature is in most regards identical to the randomly initialised configurations, with the exception of the response of the number of defects to thermal fluctuations. For the lowest temperature considered of $T^\star = 0.5$ the thermal fluctuations are unable deform the lattice sufficiently to spawn additional defects, and the number of defects remain the original 12 five-fold defects, see figure 4.25. As temperature increases to $T^\star = 1.0$ the stretching and compression effects are strong enough to introduce additional defects, with some of the initial 12 defects being converted into scars of length 3 or greater, with a strong preference for scars of length 3, see figure 4.26. As the temperature is increased beyond $T^\star = 1.0$ the generation of scars of rapidly increases until almost all isolated defects have vanished. Visual inspection of the trajectories shows that the scars introduced by these increasing fluctuations stay close to the initial lattice site of the original five-fold defect from which they emerged, and do not always include the particle which was the original five-fold defect as one of the defects in the scar, as a result of the hopping mechanism explained above. This is in contrast with the low temperature case where the original 12 five-fold defects remain fixed throughout the whole simulation range of $3000\tau$ without hopping.

For the magic number configurations the bond orientational order parameter $|\psi_6|$ does not follow a mononotic relation with temperature in contrast to the randomly initialised configurations, see figure 4.27. For the low temperature case of $T^\star = 0.5$ $|\psi_6|$ remains virtually constant with negligible fluctuations due to small lattice reformations. For the next temperature value of $T^\star$ $|\psi_6|$ initially follows the trend as in the low temperature simulation, but starts to increase after $\sim 1700\tau$. Inspection of the scar composition for the $T^\star = 1$ shows that at around $\sim 1700\tau$ the fluctuations manage to statistically convert 1 isolated defect into a scar of length 3, after which a gradual conversion of statistical conversion of another isolated defect into a scar of length 3 occurs, whereafter the scar composition remains statistically steady at $\sim 10$ isolated defects and $\sim 2$ scars of length 3, see figure 4.26. Identically for the higher temperatures, the increase in $|\psi_6|$ after the initial drop is due to the emergence of scars of length 3 created from the original 12 five-folds defects. This result is counter-intuitive; the degree of crystallinity increases due to an increase in topological defects. This result is however warranted, since the visual inspection of the trajectories show that in this transition regime of $T^\star = \{1.0, 1.5\}$ the thermal fluctuations can distort the lattice sufficiently to sternly deform the hexagonal units, which result in a low local bond orientational order parameter $|q_6|$. The additional defects resulting from these increasing deformations are not perfect pentagons or hexagons either, but are deformed as well, where the degree of deformation on the hexagonal units is large enough to have a lower $|q_6|$ value than these deformed pentagons or hexagons, resulting in an overall increase of $|\psi_6|$ by the introduction of defects. However, when only considering the temperatures for which the scar formation dynamics are slow $T^\star = \{0.5, 1.0\}$ or fast ($T^\star = \{1.5, 2.0, 2.5\}$), the same general decreasing trend of $|\psi_6|$ with an increase in temperature is obtained as for the randomly initialised configurations. For the magic number configurations the angular kicks produce the same effects as for the randomly initialised configurations resulting in an evenly chaotically fluctuating polarisation order parameter with a mean value of virtually zero indicating total orientational disorder, see figure 4.28.

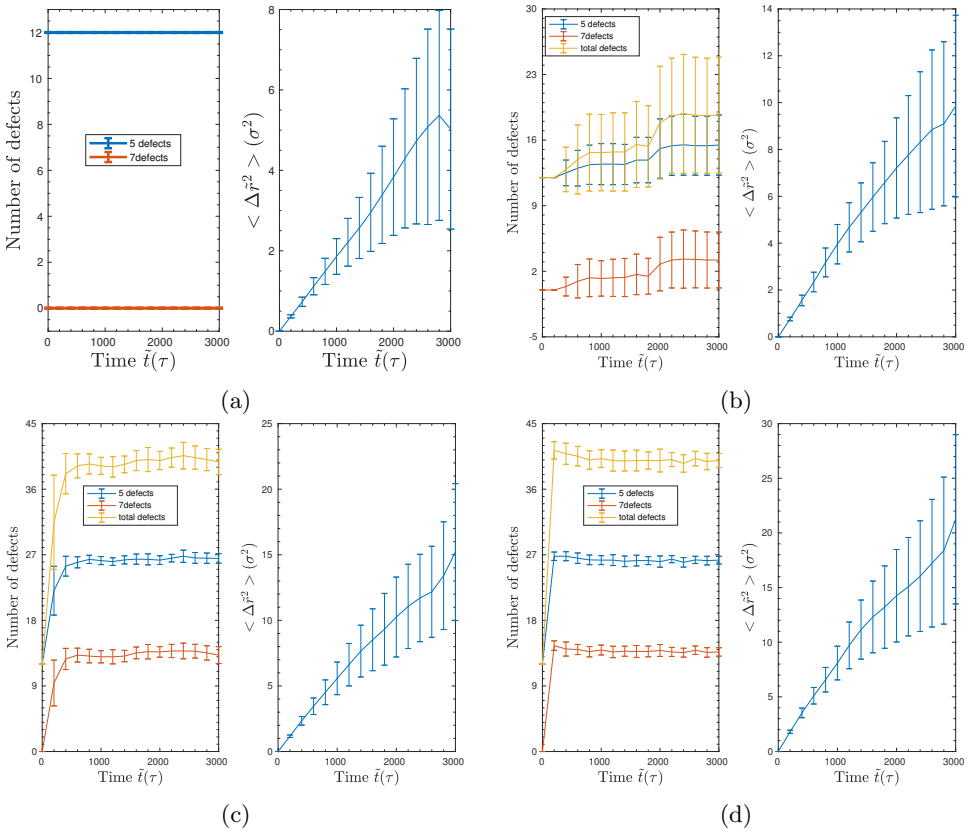


Figure 4.25: The evolution of the MSD and total number of defects for the magic number configuration of 482 passive Brownian particles (corresponding to $F = 0$) and the cases of a) $T^\star = 0.5$, b) $T^\star = 1.0$, c) $T^\star = 1.5$, and d) $T^\star = 2.5$. In figure a) the plot for the total number of defects is not shown as it precisely coincides with the plot for the 5-fold defects.

A movie for a simulation at the threshold temperature for scar formation of $T^\star = 1.5$, is available on YouTube via `https://youtu.be/RDn_2-0mVJo` which shows the triangulated lattice, and the corresponding particles on the sphere, where some particles have been tagged and their paths have been traced. In this movie the thermal fluctuations over the whole lattice and the emergence of scars of length 3 and 5 are visible in the triangulation diagram after about 50 seconds, corresponding to a simulation time of $2000\tau$.

## Summary

Overall the role of temperature for passive Brownian systems can be summarised as follows:

i The thermal fluctuations cause the sphere to perform an uncorrelated jerky rotation as result from the net thermal fluctuation being non-zero as the crystal consists of a finite number of particles.

ii Temperature has a significant effect on the structural defects of the crystal. As temperature increases the scar composition shows a clear preference for short scars of length 3.

iii For the randomly initialised configuration increasing temperature leads to a monotonic decrease in the total number of defects and the degree of crystallinity (quantified by the bond orientational order parameters $|\psi_6|$).

iv For the magic number configurations there is threshold temperature at which these minimal defect configurations start to form scars, and when the temperature is increased above this threshold $|\psi_6|$ and the scar composition behave identically as for the randomly initialised configurations.

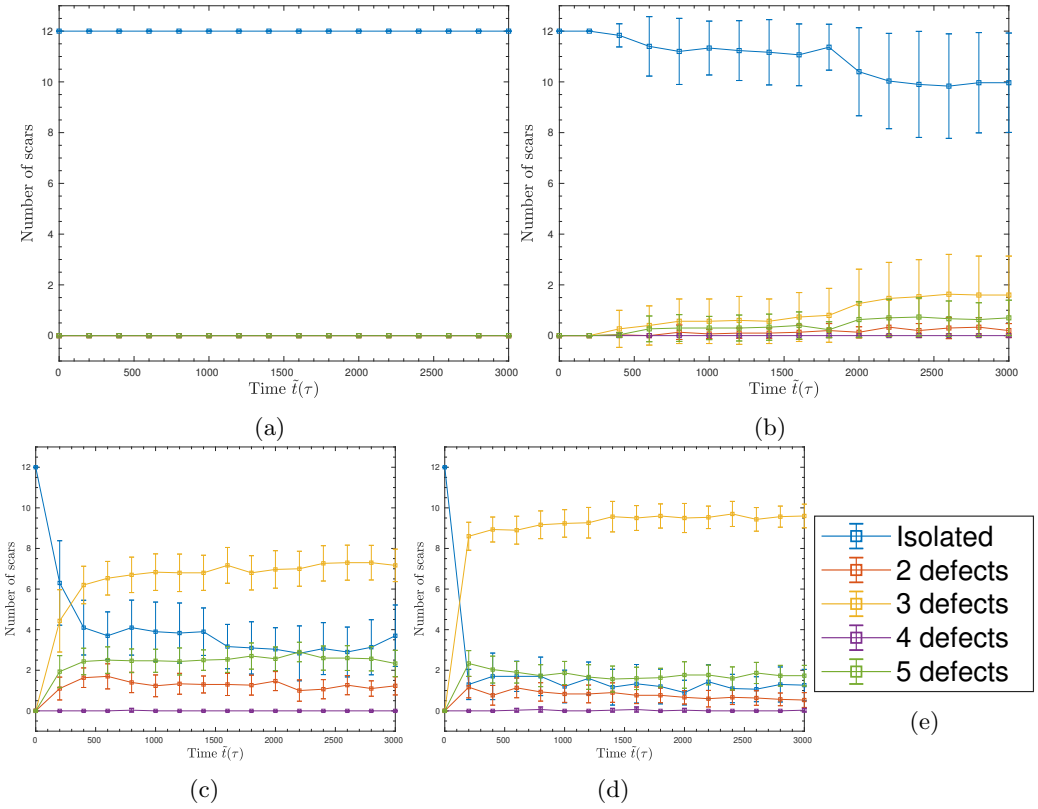


Figure 4.26: Evolution of the scar composition over time for the magic number configuration of 482 passive Brownian particles (corresponding to $F = 0$) for temperatures of a) $T^\star = 0.5$, b) $T^\star = 1.0$, c) $T^\star = 1.5$, and d) $T^\star = 2.5$. At the temperature of $T^\star = 1.0$ thermal fluctuations become strong enough to introduce additional defects to the lattice. The legend of figure e) applies to figures a)-d).

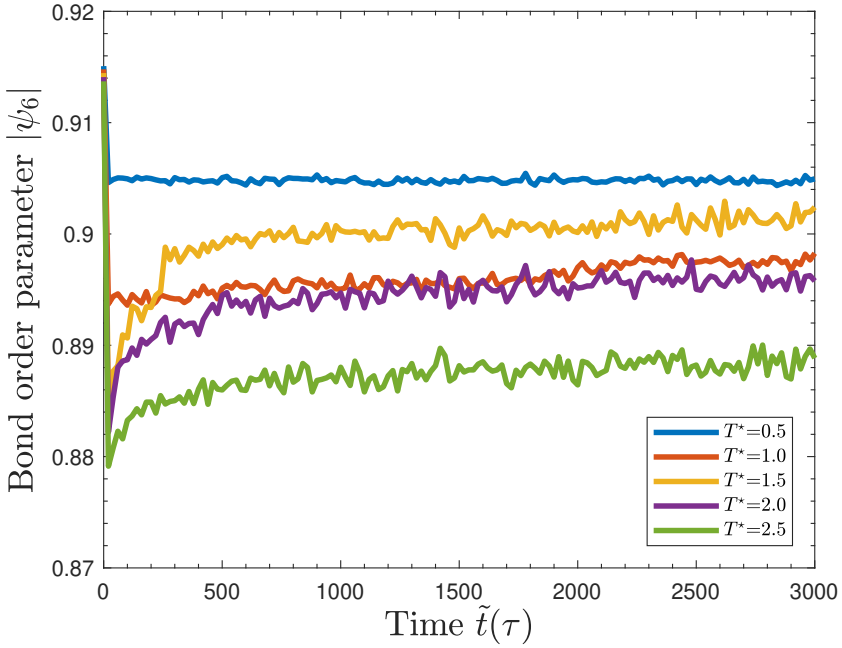


Figure 4.27: Evolution of the bond-orientational order parameter $|\psi_6|$ for the magic number configuration of 482 passive Brownian particles (corresponding to $F = 0$) as a function of temperature.

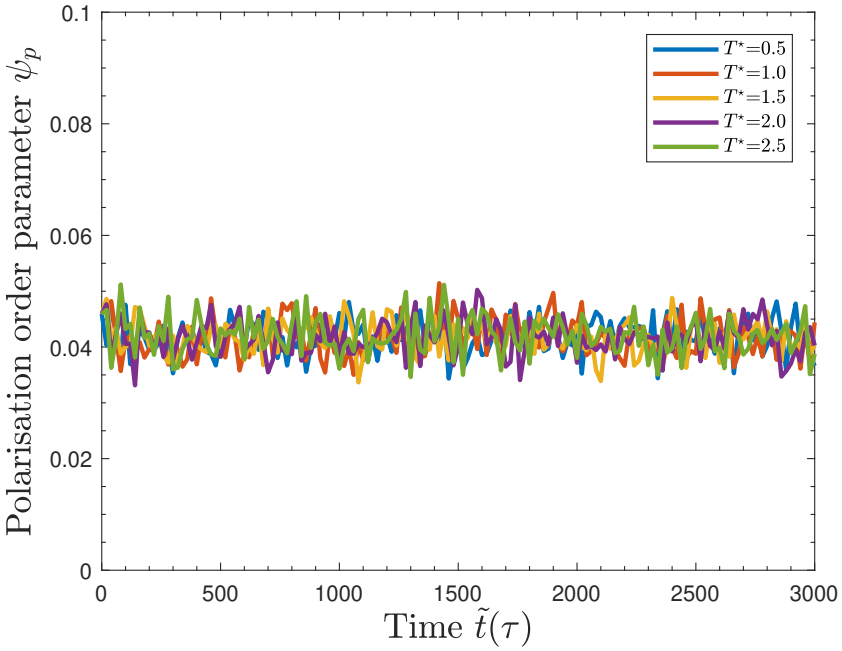


Figure 4.28: Evolution of the polarisation order parameter $\psi_p$ for the magic number configuration of 482 passive Brownian particles (corresponding to $F = 0$) as a function of temperature.

# Chapter 5

# Conclusions, discussion and outlook

In this final chapter of the report, the main results from the simulations presented in chapter 4 will be briefly recapitulated, and these results will be put in a broader context. The results for the magic number configurations will be compared to the results fro the randomly initialised configurations, and the results for passive Brownian particles and athermal active particles will be compared to see if one can act as a proxy for the other. Lastly, suggestions for improvement on the present work and an outlook for future research are given.

## Main conclusions

For the simulations on athermal active particles presented in section 4.2, it was found that activity has negligible influence on the number of defects and scar composition of the crystal, but introduces a collective rotation of the sphere. By visual inspection of the trajectories it has been observed that the scars in the crystal act like an attractor for the axis of this collective rotation, which is non-steady and translates over the surface of the sphere. For the simulations on passive Brownian particles presented in section 4.3, it was found that temperature influences the scar composition of the crystal, with a preference of the crystal to form shorter scars as the temperature is increased. Additionally, as a result from the net random walk of the particles, the spherical crystal was found to perform an uncorrelated jerky rotation.

## Contrast between magic number configurations and randomly initialised configurations

The magic number configurations are already interesting in their own right as they are a symmetric and equidistantly minimal structural defect crystal on the sphere, the magic number configurations have also shown interesting results in the performed simulations when compared to their randomly initialised counterparts. In the calibration simulations presented in section 4.1, which are performed for athermal passive particles to determine the equilibration time of the potential, the uniqueness of the magic number configurations already emerge. Both starting

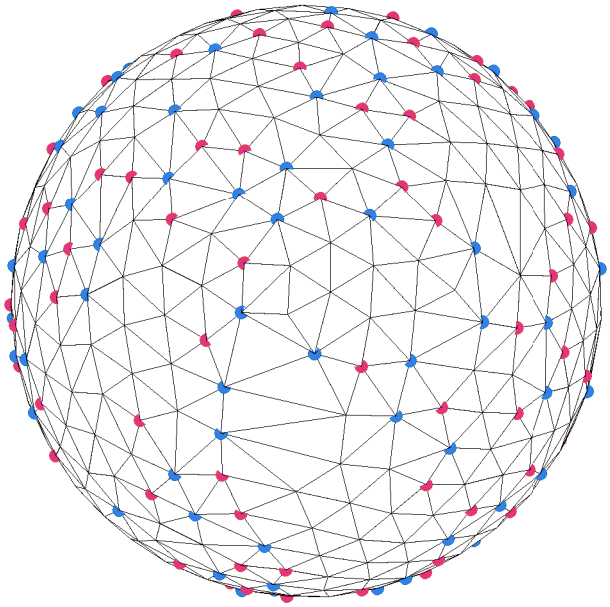

Figure 5.1: Snapshot of the Delaunay triangulation diagram for one of the randomly initialised configurations of 482 particles used to obtain the calibration time at $\tilde{t} = 0$. Besides the vast amount of defects, most of the non-defect particles are organised in severely deformed hexagonal units, corresponding to an unphysical highly stressed crystal.

configurations were simulated for the same number of particles and the equations of motion are completely deterministic, such that only initial positions determine the dynamics. Whereas the initial positions for the magic numbers correspond to the minimally required 12 five-fold defects, the initial positions of the randomly initialised configurations correspond to unphysical situations with many closely situated defects and severely deformed hexagonal units, see figure 5.1. In both cases the potential will relax the system to the lowest accessible energy minimum. However, the energy landscape for a system of large $N$ will have a complicated rugged shape with a collection of local minima separated by energy barriers [8], see figure 5.2. In the case of magic number configurations the initial positions already corresponds to one of these local energy minima and the system cannot traverse through different states, whereas the unphysical initial configuration for the completely randomly initialised systems does not correspond to a local minimum, and will have a high initial energy resulting from the large stress generated by the unphysical state of the crystal. Therefore, these randomly initialised configurations can traverse to a multitude of local energy minima until it reaches a local minimum state, where it will remain. The configuration of 12 five-fold defects, which should be attainable for both configurations since they contain the same number of particles, thus corresponds to a deeper local minimum which is inaccessible for the randomly initialised configurations, and could possibly be the global energy minimum of the ground state [34].

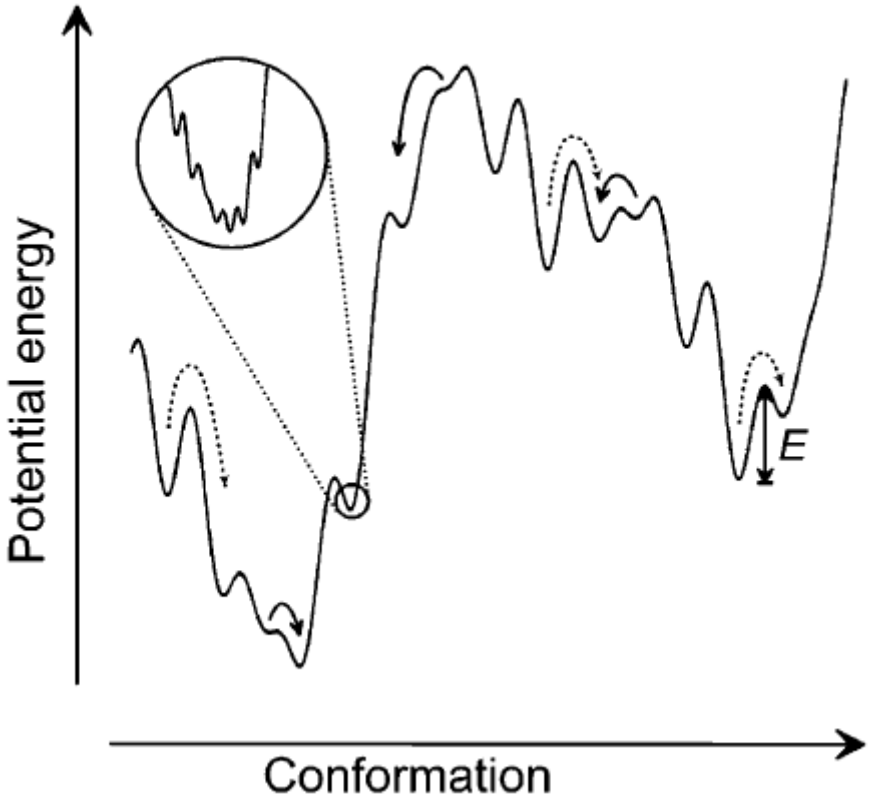


Figure 5.2: Example of a rugged potential energy landscape, showing multiple local minima and the global minimum corresponding to the ground state. The solid black arrows correspond to allowed transitions to another local minimum, whereas the dotted lines correspond to forbidden transitions to another local minimum barred by an energy barrier greater than the initial energy of the system. The conformation is a one dimensional representation of the $3N$ particle coordinates. Figure adapted from [39].

Additonally, the temperature simulations for passive Brownian particles reveal that the magic number configurations do not all correspond the system ground state. For the largest magic number configuration of 752 particles a temperature of $T^\star = 1.0$ is sufficient to generate scars from the onset of the simulation, whereas for the magic number of 482 a temperature of $T^\star = 1.0$ is only marginally able to produce scars after a period of $\sim 1700\tau$. This trend is continued onto the next magic number configuration of 272 contains scars after a temperature of $T^\star = 1.5$ is reached. This behaviour is consistent with the observation that for colloidal systems of the order $N \sim 300$ scar formation becomes increasingly relevant for curved surfaces [24, 38]. Furthermore $N \sim 300$ is also the boundary for which the magic number configurations are believed to become meta stable, as introducing additional defects for large $N$ systems can effectively lower the overall energy if the number of original defects is low [34], which is in perfect agreement with the emergence of scars for the magic number configuration of 272 particles and above, but not for the magic number configuration of 122 particles.

The magic number configurations also provided an unique opportunity to determine the attractor-like property of defects and scars on the axis of collective rotation observed in the simulations of athermal active particles. As activity has no effect on the structural defects in the crystal, the defects in the crystal remain the 12 five-fold defects which are spread symmetrically and equidistantly over the sphere. As for the randomly initialised configurations it was found that the rotation axis is attracted towards the longest scars, suggesting that the attractor strength is proportional to the length of the scar. If this is true, then it is to be expected that for symmetrically and equidistantly isolated defects the attractors stabilise the rotation axis in their centre of gravity, as is observed in the magic number simulations.

## Activity versus temperature

A comparison of the activity simulations for athermal active particles and temperature simulations of passive Brownian particles between systems of identical size show that there is no activity equivalence for temperature, i.e. there is no mapping between activity and temperature that allows one to predict the behaviour of an active system if the response of the equivalent passive system to temperature is known. This is captured by the opposing trend in the bond orientational order parameter $|\psi_6|$ which is increasing for increasing activity, but decreasing for increasing temperatures. The scar decomposition also show vastly different behaviours, whereas the scar composition in active systems is practically frozen and undergoes only marginal changes, the scar composition noticeably changes when the temperature increases, with a favouritism for shorter scars over longer scars or isolated defects, and a strong suppression of defect dipoles. Additionally, the fluctuations in the polarisation order parameter $\psi_p$ significantly differ: whereas the gradual fluctuations in the case of activity is caused by the projection of the orientation vectors $\hat{u}_a$ onto the local tangent while the sphere rotates, the fluctuations in $\psi_p$ for the temperature simulations are due to the random angular kicks and fluctuate chaotically as a result of the uncorrelated nature of the fluctuations. However, the mean values of $\psi_p$ of each system size coincide for both simulations as a result from statistical averaging and the central limit theorem. Furthermore, a comparison of the correlation functions between activity and temperature shows that the striking increase in the uncertainty in the activity simulations results from the independent evolutions of the rotational states $\vec{\omega}$ spans for each realisation. For the temperature simulations there is a random independent jerky rotation of the sphere, but the uncertainty in the correlation nevertheless remains constant, showing that this increase in uncertainty over time is a result from the unexpected translation of $\vec{\omega}$ over the sphere under the influence of scars. The changes in the bond orientational order parameter $|\psi_6|$ are marginal, with differences confined to 0.01 and 0.03 for the activity and temperature simulations respectively. The degree of crystallinity thus remains statistically constant as either activity or temperature is increased, which can be verified experimentally.

## Improvements on present work

The most interesting results of the present work is the unexpected behaviour of the translation of the rotation axis under the influence of what most reasonably is an attractor property of scars and defects. This behaviour is peculiar as the equations of motion for athermal active particles are completely deterministic and eventually these should converge to an equilibrium state where the rotation axis should remain fixed. Prolonged time simulations up to $10000\tau$ were

performed for the systems of 482 and 500 particles to verify whether a rotational equilibrium will emerge outside the considered timescale of $3000\tau$. However, even after a period of $10000\tau$ the translational motion of $\vec{\omega}$ over the sphere persisted. However, observations alone are not sufficient to understand the complete behaviour of the rotation axis, as the attractor-like property of defects cannot explain the increases and decreases in magnitude in $\vec{\omega}$ nor can it be explained why the rotation axis does not remain steadily at a scar, but eventually continues to translate over the defect-free region of the crystal until it is attracted and stabilised by another scar. To improve one this, the position of the rotation axis could be spatially correlated with the location of scars to quantify and formally proof the attractor property of the scars. Additionally, it should be noted the simulations for these active systems were performed at zero temperature, as this is the most systematic method of investigating the role of activity on the system properties by isolating any activity from temperature. However, it should be noted that such an active matter system at zero temperature is an unphysical phenomena, as dissipative systems cannot be sustained at absolute zero.

In the present work scars up to a length of 10 defects have been tracked in the present work for all simulations. This criterion is amply sufficient to track all regular scars in the crystal for all simulated systems. In the figures for the scar composition scars up to a length of 5 defects have been shown as larger scars do not significantly exist in the crystal, with the exception of the largest system of 800 particles presented in appendix F.3, where scars up to a length of 7 defects noticeably appear. Furthermore, as it has been found that higher temperatures further suppress the existence of larger scars in favour of smaller scars, there is no need to track scars of greater length. However, the lattice deformations caused by stretching and compression of the hexagons, pentagons and heptagons can introduce rare occurrences of extremely compact large defect structures up to a size of 11, which happen more often as temperature increases and larger systems are considered, [5] see figure 5.3.
Finally, it should be also noted that the analysis method used to find the length of scars is not 100% infallible. For all regular scars the correct length is found, and even the rare occurrence of the star-shaped defect of length 11 is handled correctly, however when large compact closed defect structures have a tail consisting of a linear sub-scar, the code used for finding the length of all scars cannot correctly resolve the scar length and is terminated for that trajectory. A similar problem occurs for scars consisting almost purely out of connected triangles and squares, see figure 5.4. However, since these situations of highly compact large scars are energetically unfavourable, these rare situations have no impact on the presented results as the scar composition is ensemble averaged over all 30 independent realisations.

## Outlook

The original goal of this work was to investigate the unexplored combined effect of activity and temperature on a crystal of active particles, however in order to do this first the isolated effects of temperature and activity themselves had to be known in absence of the other, which required an extensive amount of simulations. It remains thus unknown what the effect of thermal fluctuations on the active crystal would be. It might be that thermal fluctuations are able to bring balance to the rotation axis through angular diffusion and get the system into a rotational equilibrium state.

[5] More often in this context still amounts to occurring at most at 4 trajectories in less than 20% of the independent configurations for the largest system of 800 particles at the highest temperature of $T^\star = 2.5$

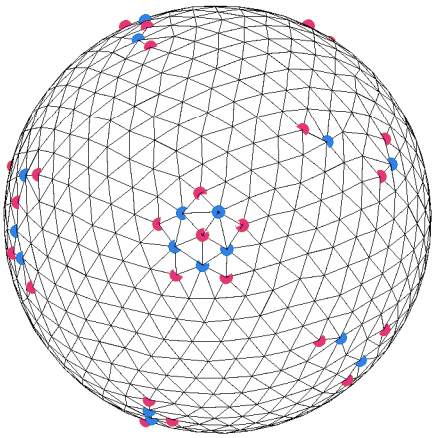

Figure 5.3: The extremely compact scar of length 11 which takes the form of a star, occurring in a realisation of the system for 800 particles as a result of fluctuations at a temperature of $T^\star = 2.5$.

(a) (b)

Figure 5.4: Two examples rare occurrences of complicated scars which are not resolved correctly in the analysis, a) a long scar build up from closed triangles and closed squares in the system of 500 particles, and b) a compact closed structure of 6 scars with a tailing linear scar in the system of 800 particles.

Future work should focus on this coupling of temperature and activity, to see if this might produce a significant effect on the bond orientational order parameter $|\psi_6|$, especially since $F$ and $T^\star$ have opposite effects. When performing these simulations it becomes important to consider a range of mobility coefficients $D_T^\star, D_R^\star$ to differentiate between the relative influences of the rotational fluctuations, influencing the direction of the self-propulsion, and the Brownian motion which results in the local stretching and compression of the lattice.

For future simulations of the active crystal it might also be fruitful to consider the effect a simplistic minimal alignment rule might have on the behaviour of the rotation axis. In the original Vicsek model for active matter each particle is equipped with the simple alignment rule that its orientation angle $\varphi_a$ should be the average of the orientation angles of its neighbours, which results into the collective motion properties of the Vicsek model [40]. This alignment rule one its own also presents an interesting situation when applied to the sphere. According to the hairy ball theorem it is impossible to obtain a continuously aligned vector field on the sphere, as the topology of the sphere requires two singularities to occur in the vector field [14, 21]. Thus supplying an alignment rule to these particles will result in additional geometrical frustration of the system.
Consistent collective rotation behaviour has been reported for active rods which experience torques about their axis, where the torques act as an aligning agent, indicating that the lack of alignment interaction can be a plausible cause in the interesting behaviour of the translation of $\vec{\omega}$ over the sphere [8]. Such a minimal alignment rule like in the Vicsek model could mimic the effect of a torque for the active particles considered here, and change this unexpected behaviour of the collective rotation to a coherent steady rotation.

# Bibliography


[1] Edward B Saff and A BJ Kuijlaars. Distributing many points on a sphere. *The mathematical intelligencer*, 19(1):5–11, 1997.

[2] Steve Smale. Mathematical problems for the next century. *The mathematical intelligencer*, 20(2):7–15, 1998.

[3] J.J. Thomson F.R.S. XXIV. On the structure of the atom: an investigation of the stability and periods of oscillation of a number of corpuscles arranged at equal intervals around the circumference of a circle; with application of the results to the theory of atomic structure. *The London, Edinburgh, and Dublin Philosophical Magazine and Journal of Science*, 7(39):237–265, 1904.

[4] Charles Kittel, Paul McEuen, and Paul McEuen. *Introduction to solid state physics*. Wiley New York, 2005.

[5] AR Bausch, Mark John Bowick, A Cacciuto, AD Dinsmore, MF Hsu, DR Nelson, MG Nikolaides, A Travesset, and DA Weitz. Grain boundary scars and spherical crystallography. *Science*, 299(5613):1716–1718, 2003.

[6] John P Hirth and Jens Lothe. *Theory of dislocations*. John Wiley\& Sons, 1982.

[7] M Cristina Marchetti, Jean-François Joanny, Sriram Ramaswamy, Tanniemola B Liverpool, Jacques Prost, Madan Rao, and R Aditi Simha. Hydrodynamics of soft active matter. *Reviews of Modern Physics*, 85(3):1143, 2013.

[8] Liesbeth MC Janssen, Andreas Kaiser, and Hartmut Löwen. Aging and rejuvenation of active matter under topological constraints. *Scientific reports*, 7(1):5667, 2017.

[9] HH Wensink and H Löwen. Emergent states in dense systems of active rods: from swarming to turbulence. *Journal of Physics: Condensed Matter*, 24(46):464130, 2012.

[10] Rastko Sknepnek and Silke Henkes. Active swarms on a sphere. *Physical Review E*, 91(2):022306, 2015.

[11] Andreas M Menzel and Hartmut Löwen. Traveling and resting crystals in active systems. *Physical review letters*, 110(5):055702, 2013.

[12] Henricus H Wensink, Jörn Dunkel, Sebastian Heidenreich, Knut Drescher, Raymond E Goldstein, Hartmut Löwen, and Julia M Yeomans. Meso-scale turbulence in living fluids. *Proceedings of the National Academy of Sciences*, 109(36):14308–14313, 2012.

[13] Eliseo Ferrante, Ali Emre Turgut, Marco Dorigo, and Cristian Huepe. Collective motion dynamics of active solids and active crystals. *New Journal of Physics*, 15(9):095011, 2013.

[14] Simon Praetorius, Axel Voigt, Raphael Wittkowski, and Hartmut Löwen. Active crystals on a sphere. *Physical Review E*, 97(5):052615, 2018.

[15] Felix C Keber, Etienne Loiseau, Tim Sanchez, Stephen J DeCamp, Luca Giomi, Mark J Bowick, M Cristina Marchetti, Zvonimir Dogic, and Andreas R Bausch. Topology and dynamics of active nematic vesicles. *Science*, 345(6201):1135–1139, 2014.

[16] Aparna Baskaran and M Cristina Marchetti. Hydrodynamics of self-propelled hard rods. *Physical Review E*, 77(1):011920, 2008.

[17] Leonardo Apaza and Mario Sandoval. Brownian self-driven particles on the surface of a sphere. *Physical Review E*, 96(2):022606, 2017.

[18] Julian Bialké, Thomas Speck, and Hartmut Löwen. Crystallization in a dense suspension of self-propelled particles. *Physical review letters*, 108(16):168301, 2012.

[19] Leonardo Apaza and Mario Sandoval. Active matter on riemannian manifolds. *Soft matter*, 14(48):9928–9936, 2018.

[20] Yaouen Fily, Aparna Baskaran, and Michael F Hagan. Active particles on curved surfaces. *arXiv preprint arXiv:1601.00324*, 2016.

[21] Perry W Ellis, Daniel JG Pearce, Ya-Wen Chang, Guillermo Goldsztein, Luca Giomi, and Alberto Fernandez-Nieves. Curvature-induced defect unbinding and dynamics in active nematic toroids. *Nature Physics*, 14(1):85, 2018.

[22] Pablo A Vieira and Daniel J Lacks. Particle packing in soft-and hard-potential liquids. *The Journal of chemical physics*, 119(18):9667–9672, 2003.

[23] Michael Paul Hobson, George P Efstathiou, and Anthony N Lasenby. *General relativity: an introduction for physicists*. Cambridge University Press, 2006.

[24] William TM Irvine, Vincenzo Vitelli, and Paul M Chaikin. Pleats in crystals on curved surfaces. *Nature*, 468(7326):947, 2010.

[25] Rodrigo E Guerra, Colm P Kelleher, Andrew D Hollingsworth, and Paul M Chaikin. Freezing on a sphere. *Nature*, 554(7692):346, 2018.

[26] Miha Brojan, Denis Terwagne, Romain Lagrange, and Pedro M Reis. Wrinkling crystallography on spherical surfaces. *Proceedings of the National Academy of Sciences*, 112(1):14–19, 2015.

[27] Pawel Romanczuk, Markus Bär, Werner Ebeling, Benjamin Lindner, and Lutz Schimansky-Geier. Active brownian particles. *The European Physical Journal Special Topics*, 202(1):1–162, 2012.

[28] John D Weeks, David Chandler, and Hans C Andersen. Role of repulsive forces in determining the equilibrium structure of simple liquids. *The Journal of chemical physics*, 54(12):5237–5247, 1971.

[29] Alon Kipnis, Andrea J Goldsmith, and Yonina C Eldar. The distortion-rate function of sampled Wiener processes. *IEEE Transactions on Information Theory*, 65(1):482–499, 2019.

[30] Benedict Leimkuhler and Sebastian Reich. *Simulating hamiltonian dynamics*, volume 14. Cambridge university press, 2004.

[31] James Welty, Gregory L Rorrer, and David G Foster. *Fundamentals of momentum, heat and mass transfer*. Wiley Global Education, 2014.

[32] Alessandro Patti and Alejandro Cuetos. Brownian dynamics and dynamic Monte Carlo simulations of isotropic and liquid crystal phases of anisotropic colloidal particles: A comparative study. *Physical Review E*, 86(1):011403, 2012.

[33] Kazuhiko Ohno, Tomoki Nitta, and Hiroto Nakai. SPH-based fluid simulation on GPU using Verlet list and subdivided cell-linked list. In *2017 Fifth International Symposium on Computing and Networking (CANDAR)*, pages 132–138. IEEE, 2017.

[34] Mark J Bowick, Angelo Cacciuto, David R Nelson, and Alex Travesset. Crystalline particle packings on a sphere with long-range power-law potentials. *Physical Review B*, 73(2):024115, 2006.

[35] Cris Cecka. Thomson applet. url:`http://thomson.phy.syr.edu/thomsonapplet.php`. Accessed: 08-05-2019.

[36] Boris Delaunay et al. Sur la sphere vide. *Izv. Akad. Nauk SSSR, Otdelenie Matematicheskii i Estestvennyka Nauk*, 7(793-800):1–2, 1934.

[37] G Briand and Olivier Dauchot. Crystallization of self-propelled hard discs. *Physical review letters*, 117(9):098004, 2016.

[38] Peter Lipowsky, Mark J Bowick, Jan H Meinke, David R Nelson, and Andreas R Bausch. Direct visualization of dislocation dynamics in grain-boundary scars. *Nature materials*, 4(5):407, 2005.

[39] Lilia Milanesi, Jonathan P Waltho, Christopher A Hunter, Daniel Shaw, Godfrey Beddard, Gavin D Reid, Sagarika Dev, and Martin Volk. Measurement of energy landscape roughness of folded and unfolded proteins. *Proceedings of the National Academy of Sciences*, 109:19563–19568, 11 2012.

[40] Tamás Vicsek, András Czirók, Eshel Ben-Jacob, Inon Cohen, and Ofer Shochet. Novel type of phase transition in a system of self-driven particles. *Physical review letters*, 75(6):1226, 1995.

[41] Dieter Kotschick. The topology and combinatorics of soccer balls: when mathematicians think about soccer balls, the number of possible designs quickly multiplies. *American Scientist*, 94(4):350–357, 2006.

[42] F Debbasch and M Moreau. Diffusion on a curved surface: a geometrical approach. *Physica A: Statistical Mechanics and its Applications*, 343:81–104, 2004.

[43] David Chandler. *Introduction to modern statistical mechanics*. Oxford university press, 1987.

[44] Michael Wilkinson and Alain Pumir. Spherical ornstein-uhlenbeck processes. *Journal of Statistical Physics*, 145(1):113, 2011.

[45] David J Griffiths. *Introduction to electrodynamics; 4th ed.* Cambridge University Press, 2017.

# Acknowledgements

I would like to thank G. Bonné for sharing useful applications, settings and tips for getting started in Linux. Furthermore, I would like to thanks B. de Braaf and S. Ciarella for sharing feedback on the usage of the computer cluster. Additionally I would like to express my gratitude towards the Stack Overflow and MatLab Answer communities for actively posing and answering questions.

Last, but definitively not least, I would like to give my special thanks to Dr. L.M.C. Janssen for sharing her extensive knowledge and expertise on the field of active matter, and foremost her flexibility in allowing me to define, shape and execute this research project according to my own vision.

# Appendix A

# The Euler characteristic on a sphere

The Euler characteristic is a number which describes the surface of objects build out of polyhedrons and is given by

$$\chi = F - E + V \tag{A.1}$$

where $\chi$ is the Euler characteristic, $F$ the total number of faces, $E$ the total number of edges, and $V$ the number total of vertices [1]. If the surface would be build solely out of $m$ hexagons and $n$ pentagons, then $F, E, V$ take on the values [41]

$$\begin{cases} F = m + n \\ E = \frac{5m+6n}{2} \\ V = \frac{5m+6n}{3} \end{cases} \tag{A.2}$$

as the total number of faces is simply the total number of polygons tiled on the surface, each hexagon has 6 vertices and each pentagon has 5 vertices, but since the total surface is covered by these polygons, each edge of a polygon is connected to the edge of another, and each vertex also serves as the vertices of 2 neighbouring polygons. Substituting equation (A.2) into equation (A.1) gives

$$\chi = m\big(1 - \frac{6}{2} + \frac{6}{3}\big) + n\big(1 - \frac{5}{2} + \frac{5}{3}\big) = \frac{n}{6}. \tag{A.3}$$

As the value of the Euler characteristic takes on the value $\chi = 2$ on the sphere, equation (A.3) gives there are 12 pentagons needed to tile the surface of a sphere.

# Appendix B

# Derivation of the EoM for Brownian motion

As a point of departure consider the Ornstein–Uhlenbeck process for Brownian motion of a non interacting passive particle [42], labelled by $a$

$$\dot{\vec{r}}_a(t) = \frac{\vec{p}_a(t)}{m_a} \tag{B.1a}$$

$$\dot{\vec{p}}_a(t) = -\xi\vec{p}_a(t) + \vec{\tilde{\sigma}}_a(t) \tag{B.1b}$$

where $\vec{r}_a$ denotes a particle position, $\vec{p}_a$ its momentum, $m_a$ its mass, $\xi$ denotes the momentum friction coefficient, and $\vec{\sigma}_a$ denotes the influence from momentum fluctuations. In the delta function approximation the fluctuations caused by $\vec{\tilde{\sigma}}_a$ occur on a much fast scale than the diffusive motion and are correlated by

$$\left\langle \vec{\tilde{\sigma}}_a(0) \cdot \vec{\tilde{\sigma}}_a(t) \right\rangle = 2m_a k_b T \xi \delta(t) \tag{B.2}$$

where $k_b$ denotes the Boltzmann constant and $T$ the temperature. Taking the dot product of equation (B.1b) with $\vec{p}_a(0)$ and averaging gives

$$\frac{\mathrm{d}\left\langle \vec{p}_a(0) \cdot \vec{p}_a(t) \right\rangle}{\mathrm{d}t} = -\xi \left\langle \vec{p}_a(0) \cdot \vec{p}_a(t) \right\rangle + \left\langle \vec{p}_a(0) \cdot \vec{\tilde{\sigma}}_a \right\rangle \tag{B.3}$$

however, since the fluctuations are random they are uncorrelated with respect to any deterministic variable: $\left\langle \vec{p}_a(0) \cdot \vec{\tilde{\sigma}}_a \right\rangle = \left\langle \vec{p}_a(0) \right\rangle \cdot \left\langle \vec{\tilde{\sigma}}_a \right\rangle = 0$ since the expectation of a fluctuation term always vanishes. Then equation (B.3) reduces to a simple ODE and can be integrated to give the autocorrelation

$$\left\langle \vec{p}_a(0) \cdot \vec{p}_a(t) \right\rangle = \left\langle p_a^2(0) \right\rangle \exp(-\xi t). \tag{B.4}$$

The value of $\left\langle p_a^2(0) \right\rangle$ can be expressed in terms of the translational diffusion constant $D$ via the Green-Kubbo relation [43]

$$D = \frac{1}{3}\int_0^\infty dt \left\langle \vec{v}_a(t) \cdot \vec{v}_a(0) \right\rangle = \frac{1}{3m_a^2}\int_0^\infty dt \left\langle \vec{p}_a(t) \cdot \vec{p}_a(0) \right\rangle = \frac{1}{3\xi m_a^2}\left\langle p_a^2 \right\rangle \tag{B.5}$$

where in equation (B.1a) was substituted in going from the second to third equality. And the value of $\langle p_a^2 \rangle$ can be obtained from the Maxwell-Boltzmann distribution

$$P(\vec{v})d^3\vec{v} = \big(\frac{m}{2\pi k_b T}\big)^{3/2} \exp\bigg(-\frac{m\sum_i v_i^2}{2k_b T}\bigg) d^3\vec{v} \tag{B.6}$$

where $d^3\vec{v} = dv_x dv_y dv_z$. This velocity distribution can be converted to a momentum distribution according to

$$P(\vec{p})d^3\vec{p} = P(\vec{v})\frac{\mathrm{d}^3\vec{v}}{\mathrm{d}^3\vec{p}} d^3\vec{p} = \big(\frac{1}{2m\pi k_b T}\big)^{3/2} \exp\bigg(-\frac{\sum_i p_i^2}{2mk_b T}\bigg) d^3\vec{p}. \tag{B.7}$$

By performing a coordinate transformation to substitute the components of $\vec{p}$ for the length of the momentum $\|\vec{p}\| \equiv p$ by $d^3\vec{v} = 4\pi p^2 dp$, $\langle p^2 \rangle_a$ is given by

$$\langle p_a^2 \rangle = \int_0^\infty dp\ p^2 P(p) = 4\pi \big(\frac{1}{2m\pi k_b T}\big)^{3/2} \int_0^\infty dp\ p^4 \exp\bigg(-\frac{p^2}{2m_a k_b T}\bigg). \tag{B.8}$$

Performing the substitution $u = \frac{p}{\sqrt{2m_a k_b T}}$ to rewrite this into the standard integral $\int_0^\infty du\, u^4 \exp\big(-u^2\big) = \frac{3\sqrt{\pi}}{8}$ yields

$$\langle p_a^2 \rangle = 3m_a k_b T \tag{B.9}$$

such that the diffusion constant is given by

$$D = \frac{k_b T}{m_a \xi}. \tag{B.10}$$

To obtain the Langevin equation, equation (B.1a) is substituted into equation (B.1b) giving

$$\frac{\mathrm{d}m_a \dot{\vec{r}}_a}{\mathrm{d}t} = -\gamma \dot{\vec{r}}_a + \vec{\sigma}_a \tag{B.11}$$

where $\gamma \equiv m_a \xi$ is the velocity drag coefficient. The fluctuations $\vec{\sigma}_a$ can be expressed using equation (B.2) and considering a small interval $\Delta t \approx 0$ such that $\delta(t) \approx \Delta t$, such that $\vec{\sigma}_a = \sqrt{2\gamma k_b T \Delta t} * \vec{\zeta}$ where $\vec{\zeta}$ is a random vector whose components have zero mean and unity variance [32]. Then the equation Langevin equation for a non-interacting passive particle is obtained

$$m_a \ddot{\vec{r}}_a = -\gamma \dot{\vec{r}}_a + \sqrt{2\gamma k_b T \Delta t} * \vec{\zeta}. \tag{B.12}$$

For the angular dynamics a similar analysis can be done where the instead of the momenta, angular velocities $\omega_a$ are considered [44], and the result is expressed in terms of the orientation angle $\varphi_a$, yielding

$$\gamma_R \dot{\varphi}_a = \sqrt{2\gamma_R k_b T \Delta t} * \eta \tag{B.13}$$

where $\gamma_R$ is the rotational friction coefficient and $\eta$ is again a random variable of zero mean and unity variance, but is uncorrelated to the components of $\vec{\zeta}$. Similarly to the translational case (equation (B.10)), the rotational diffusion coefficient is then given by

$$D_R = \frac{k_b T}{\gamma_R}. \tag{B.14}$$

# Appendix C

# Determining the constraint force

The constraint that all particles should lie in the sphere is given by

$$g(x_a, y_a, z_a) = x_a^2 + y_a^2 + z_a^2 - R^2 = 0 \tag{C.1}$$

which, despite the implicit time dependence of the particle's coordinates, does not explicitly depend on time, since the radius of the sphere itself is fixed. For such a holonomic, scleronomic constraint the corresponding constraint force is given by

$$\vec{F}_{con} = -\lambda \boldsymbol{\nabla} g(\vec{r}) \tag{C.2}$$

where $\lambda$ is an unknown parameter depending on the constraint and the EoM itself, similarly to how an undetermined Lagrange multiplier depends on the constraint and the function to be optimised in an optimisation problem. The minus sign in equation (C.2) has been introduced as convenience and similarity with $\vec{F} = -\boldsymbol{\nabla} V$ for interaction forces, such that by analogy the constraint can be interpreted as an equipotential surface of an iso-potential described by $g$. Since $\boldsymbol{\nabla} g$ described the direction of steepest ascend, the constraint force will always be normal to the (iso) equipotential surface. An intuitive example of a constraint force obeying (C.2) is the gravitational force, $\vec{F}_g = m_g \boldsymbol{\nabla} \Phi$, where $\Phi$ is the gravitational potential, and the gravitational mass $m_g$ is the $\lambda$, which keeps all objects without any excess kinetic energy bound to the surface of Earth, and thus clearly acts perpendicular to the surface described by the equipotential surface of $\Phi$.
Consider the derivative of $g$

$$\frac{\mathrm{d}g(\vec{r}_a)}{\mathrm{d}t} = \boldsymbol{\nabla} g \cdot \frac{\mathrm{d}\vec{r}_a}{\mathrm{d}t} = \boldsymbol{\nabla} g \cdot \ \dot{\vec{r}}_a = 0 \tag{C.3}$$

which confirms the intuition that any motion under a constraint force is tangential to the equipotential surface, as $\boldsymbol{\nabla} g$ is normal to the equipotential surface. For the constraint of equation (C.1) $\boldsymbol{\nabla} g = 2\vec{r}_a$, and thus $\vec{r}_a \cdot \dot{\vec{r}}_a = 0$. Plugging the constraint force into the EoM (equation (2.10a)) gives

$$m_a \ddot{\vec{r}}_a = -\gamma \dot{\vec{r}}_a + \vec{F}_{act,a} + \vec{F}_{int,a} - 2\lambda \vec{r}_a + \sqrt{2\gamma k_b T \delta(t)} * \vec{\zeta} \tag{C.4}$$

and then taking the dot product of equation (C.4) with $\dot{\vec{r}}_a$ gives

$$m_a \ddot{\vec{r}}_a \cdot \vec{r}_a = \left(\vec{F}_{int,a} + \sqrt{2\gamma k_b T \delta(t)} * \vec{\zeta}\right) \cdot \vec{r}_a - 2\lambda r_a^2 \tag{C.5}$$

where $\vec{r}_a \cdot \dot{\vec{r}}_a = 0$ and the fact that $\hat{u}$ lies in the tangent plane of each particle (such that $\hat{u} \cdot \vec{r}_a = 0$) were used to cancel the contributions of the friction force and activity. Now using the product rule

$$\ddot{\vec{r}}_a \cdot \vec{r}_a = \frac{\mathrm{d}\dot{\vec{r}}_a}{\mathrm{d}t} \cdot \vec{r}_a = \frac{\mathrm{d}\dot{\vec{r}}_a \cdot \vec{r}_a}{\mathrm{d}t} - \dot{\vec{r}}_a \cdot \frac{\mathrm{d}\vec{r}_a}{\mathrm{d}t} = -\dot{r}_a^2 \tag{C.6}$$

such that equation (C.5) can be solved for $\lambda$

$$2\lambda = \frac{1}{r_a^2}\Big[m_a \dot{r}_a^2 + \big(\vec{F}_{int,a} + \sqrt{2\gamma k_b T \delta(t)} * \vec{\zeta}\big) \cdot \vec{r}_a\Big]. \tag{C.7}$$

Substituting the solution for $\lambda$ back into the EoM of (C.4) and using $\frac{\vec{r}_a}{r_a} = \hat{r}$ the EoM has been rewritten without any unknowns:

$$m_a \ddot{\vec{r}}_a = -\gamma \dot{\vec{r}}_a + \vec{F}_{act} + \Big[\vec{\mathcal{F}} - \big(\vec{\mathcal{F}} \cdot \hat{r}\big)\hat{r}\Big] - m_a \dot{r}_a^2 \hat{r} \tag{C.8}$$

where $\mathcal{F} = \vec{F}_{int,a} + \sqrt{2\gamma k_b T \delta(t)} * \vec{\zeta}$ has been used a short hand notation. Equation (C.8) gives the intuitive results that the constraint force cancels the radial components of the interaction force and thermal fluctuations, such that at all times all motion remains constraint to the surface of the sphere.

# Appendix D

# Spherical coordinates

Throughout this report, an extensive amount of coordinate transformations between spherical coordinates $(r, \theta, \phi)$ and Cartesian coordinates $(x, y, z)$ is used to translate quantities between these reference frames. The advantage of doing this is that the Cartesian basis vectors are position independent and thus serve as an absolute measure of e.g. the force or the position at every point in space in these directions. However on the spherical manifold, it is more convenient to express quantities in terms of the radius, polar angle $(\theta)$, and azimuthal angle $(\phi)$.
Here a short overview is given about the relations between these coordinate transformations:

$$\begin{cases} x = r\sin(\theta)\cos(\phi) \\ y = r\sin(\theta)\sin(\phi) \\ z = r\cos(\theta) \end{cases} \quad \begin{cases} r = \sqrt{x^2 + y^2 + z^2} \\ \theta = \arccos\left(\frac{z}{r}\right) \\ \phi = \arctan\left(\frac{y}{x}\right) \end{cases}, \tag{D.1}$$

and their normalised unit vectors:

$$\begin{cases} \hat{x} = \sin(\theta)\cos(\phi)\ \hat{r} + \sin(\theta)\sin(\phi)\ \hat{\theta} - \sin(\phi)\ \hat{\phi} \\ \hat{y} = \cos(\theta)\cos(\phi)\ \hat{r} + \cos(\theta)\sin(\phi)\ \hat{\theta} + \cos(\phi)\ \hat{\phi} \\ \hat{z} = \cos(\theta)\ \hat{r} - \sin(\theta)\ \hat{\theta} \end{cases}$$
$$\begin{cases} \hat{r} = \sin(\theta)\cos(\phi)\ \hat{x} + \sin(\theta)\cos(\phi)\ \hat{y} + \cos(\theta)\ \hat{z} \\ \hat{\theta} = \cos(\theta)\cos(\phi)\ \hat{x} + \cos(\theta)\cos(\phi)\ \hat{y} - \sin(\theta)\ \hat{z} \\ \hat{\phi} = -\sin(\phi)\ \hat{x} + \cos(\phi)\ \hat{y} \end{cases} . \tag{D.2}$$

These relations can be found in just about any textbook involving vector calculus, e.g. [45].

# Appendix E

# Details of cell listing on sphere

As described in section 3.3 of the main text, the sphere is subdivided into segments of arc length $l_r$, which is motivated by the fact that three particles separated by the Euclidean distance $r_c$ are separated by a distance $l \geq 3r_c$ on the spherical surface. For convenience $l_r$ is chosen such that $l = 3l_r$ exactly. Thus unlike the flat Euclidean plane where all interactions are limited to the square box of $3r_c \times 3r_c$ centred around the cell $(i, j)$, on the sphere the interactions are limited to the area spun by $3l_r \times 3l_r$ centred around the cell $(i, j)$. The angular width of a cell follows from trigonometry for two particles separated by $r_c$ on a sphere of radius $R$

$$\alpha = 2 \arcsin\Big(\frac{r_c}{2R}\Big), \tag{E.1}$$

and the arc length $l_r$ is then given by the fraction of the great circle encompassed by the angular width $\alpha$

$$l_r = 2\pi R \frac{\alpha}{2\pi}. \tag{E.2}$$

See figure E.1a and E.1b.

A straightforward method for dividing the surface of the sphere into cells is by using the intersections of Cartesian planes with the surface as cell boundaries. Then cuts in the $z$ axis are determined by the intersection of the sphere with planes parallel to the $xy$ plane, and correspond to cuts at constant $z$, and constant spacing $\Delta z$. By analogy with geography, these intersections form lines of constant latitude, e.g. the Tropic of Cancer, the Tropic of Capricorn, the Arctic circle and the Antarctic circle, and hence give a way of identifying $i$. By analogy one would be quick to identify $j$ with a line of constant $\phi$, i.e. a meridian at the Earth surface, see figure E.2. Then practically the same situation as for the 2D flat Euclidean plane is recovered where each cell $i, j$ can only interact with the cells $i' \in \{i-1, i+1\}, j' \in \{j-1, j+1\}$, with the exceptions at the poles where at the North- and South pole respectively $i-1, i+1$ do not exist.

However for a given $(i, j)$ the cell is located both at the 'front' and in the 'back' of the sphere, which in case $R < \frac{r_c}{2}$ are able to interact over the surface sphere. If however $R > \frac{r_c}{2}$, cells around the equator and prime meridian will not have an interaction with their counterparts on the opposite side. See figure

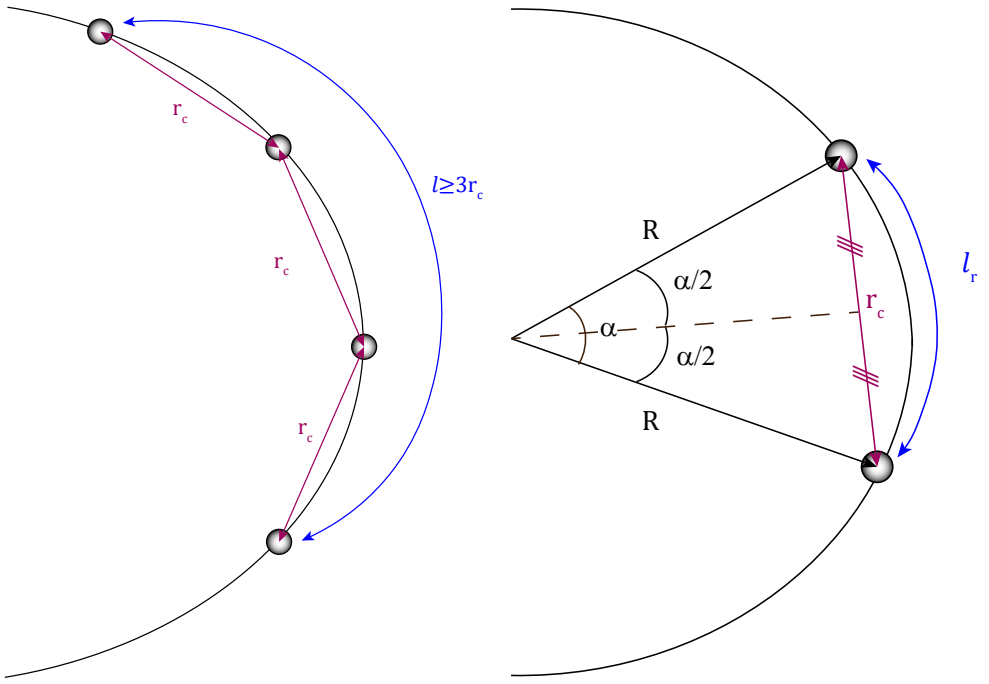


(a) (b)

Figure E.1: Determination of arclength segment $l_r$, a) gives an exaggerated representation of the difference between the arclength and Euclidean distance of $3r_c$ and b) portrays the geometry with the angular width $\alpha$.

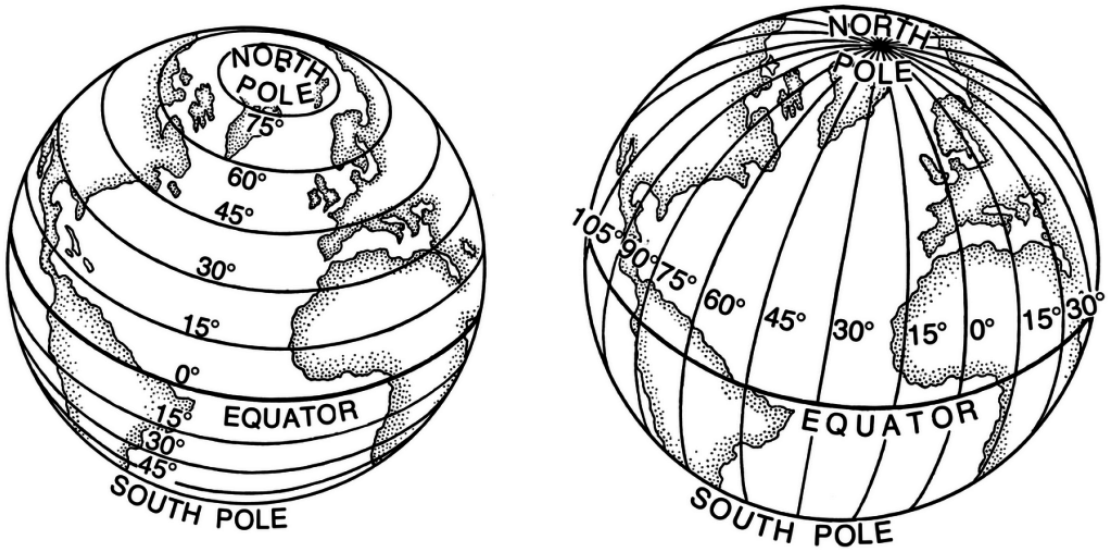


Figure E.2: Left: circles of latitude at Earth's surface corresponding to planes of constant $z$. Right: meridians at Earth's surface corresponding to planes of constant $\phi$. Source: `https://courses.lumenlearning.com/geophysical/chapter/geographic-grid-system/`

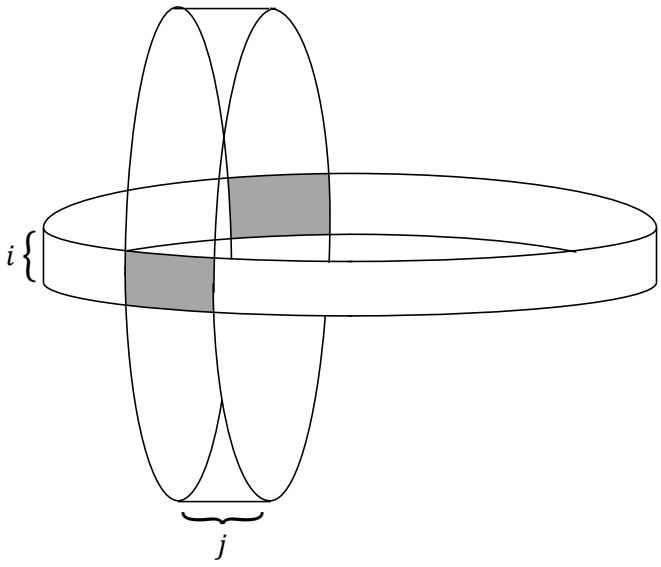


Figure E.3: The problem with sampling the surface of the sphere with only two indices: 2 cells appear at the front and in the back with the same $(i, j)$ index whereas the distance between these cells can exceed $r_c$.

This can be solved by choosing a different measure for $j$, e.g. the boundaries of a cell $j$ are determined by the intersection of the surface with $yz$ planes of constant $x$ and separation $\Delta x$. Then it is clear that for particles at the equator for which $(z_a = 0, |y_a| \ll |x_a|$, i.e. particles near the 'East' and 'West' can interact with their counterparts, where particles for which $z_a = 0, |y_a| \approx |x_a|$ will be out of range to interact with their counterparts at the opposite side (where a sphere of radius $R = r_c$ is begin considered). Then a third measure is required to differentiate between the 'front' and 'back' of the sphere. Since cuts in the $x$ axis and $z$ axis have already been used, the only available option is a cut in the $y$ axis, however only one cut is required since the sphere needs only be divided into two hemispheres to distinguish between the 'front' and the 'back'. Mathematically this is because $y$ is not an independent coordinate but depends on $x, z$ according to $y = \pm\sqrt{R^2 - x^2 - z^2}$, and the distinction between the 'front' and 'back' of the sphere is equivalent to the distinction between the positive and negative root. As $y = r\sin(\theta)\sin(\phi)$, and $\theta$ is already linked to $i$ since $z = r\cos(\theta)$, the distinction between the positive and negative root is caused by the sign of $\sin(\phi)$, which changes sign at $\phi = n\pi$, where $n \in \mathbb{N}$. Since physically $\phi \in [0, 2\pi)$, the cut thus occurs at $\phi = \pi$ and hence $k$ can be identified as

$$k = \lceil \frac{\phi}{\pi} \rceil, \tag{E.3}$$

using $k = 1$ as definition for the 'front' of the sphere and $k = 2$ as definition for the 'back' of the sphere.

Now the problem remains to identify $i, j$ given the particle coordinates. In order to (ab)use the symmetry of the sphere, $i$ and $j$ should be even, such that a cut always occurs at $z = 0$ and $x = 0$ respectively. The easiest way of dividing the sphere into cells is by choosing $i_{max} = j_{max} = n$ with $n$ and even positive integer, i.e. $n = 2m$, where $m \in \mathbb{N}$. As each cell has an arc length $l_r$ at

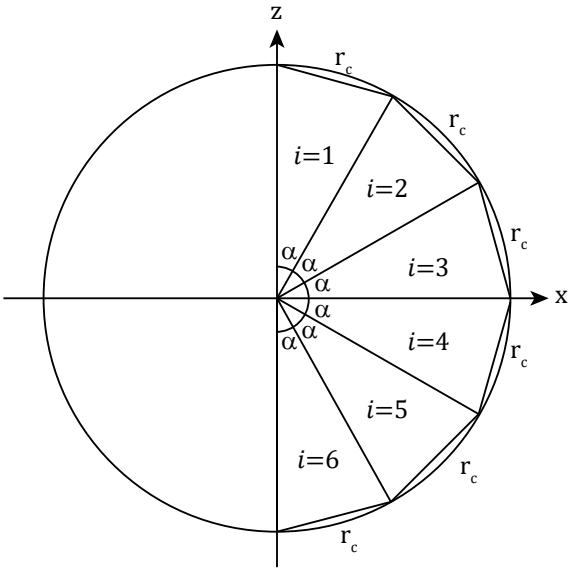


Figure E.4: Projection of the cell listing on the xz plane for the case $n = 6$, where each cell has an angular width $\alpha$ according to equation (E.6), and the $i$ index of the cells is mapped by equation (E.7).

both sides, $n$ is determined by the amount of times $l_r$ fits on the great circle

$$n_{arc} = \lfloor \frac{2\pi R}{l_r} \rfloor, \tag{E.4}$$

where the floor function ensures $l_r \geq r_c$. Then since this in both directions[6],

$$n = \frac{n_{arc}}{2}. \tag{E.5}$$

The corrected angular width corresponding to $n$ cells each in the $i, j$ direction is then

$$\alpha' = \frac{2\pi}{n_{arc}} = \frac{\pi}{n}. \tag{E.6}$$

From now on, for notational convenience, whenever $\alpha$ is used it refers to the corrected value of $\alpha'$ to keep all equations neat. Since the $z = r\cos(\theta)$, $i$ is sampled by the intersection of the sphere with a plane of constant $z$ it follows that $i$ can be identified as

$$i = \lceil \frac{\theta}{\alpha} \rceil \tag{E.7}$$

such that all particles with $R\cos(\alpha) < z_a \leq R$ are inside the cell with index $i = 1$, all particles with $R\cos(2\alpha) < z_a \leq R\cos(\alpha)$ are inside the cell with index $i = 2$, etc., etc., etc., see figure E.4.

Now only a measure for $j$ is still needed. As explained above $k$ is linked to sign of the Cartesian coordinate $y_a$ and $i$ is linked to the Cartesian coordinate $z_a$. In the upper half of the $xy$ plane

[6]Here it was assumed that $n_{arc}$ is divisible by 4, such that $n$ is an even integer, but if this is not cased $n_{arc}$ has to be corrected for its remainder after dividing by 4.

$k = 1$ is valid and the angle spun between the positive and negative $x$-axis is $\pi$, which is precisely the range for $\theta$ which is divisible into $n$ segments of $\alpha$, thus the same can be done for the angle $\phi$ in the upper half of the $xy$ plane. For clarity let's consider the specific example of $n = 6$ in the equatorial plane ($z = 0$). The left most $x$ coordinate $x = -R$ is used as the origin for $j$, corresponding to $\phi = \pi = 6\alpha$, then rotating by an angle of $\alpha$ to the right denotes the first cut in the $x$ direction on the sphere, thus corresponding to an angle of $\phi = 5\alpha$. The region $-R = R\cos(6\alpha) < x \leq R\cos(5\alpha)$ then corresponds to cells with index $j = 1$. Next rotating by $\alpha$ again, the region enclosed by $R\cos(5\alpha) < x \leq R\cos(4\alpha)$ then corresponds to cells with index $j = 2$, etc., etc., see figure E.5. Evidently particles with $x < 0$ are always in cells with index $1 \leq j \leq \frac{n}{2}$, and particles with $x > 0$ are always in cells with index $\frac{n}{2} + 1 \leq j \leq n$. It may seem like the angle $\phi$ is used as metric again, however this is not true, since the index $j$ cannot take any value but is constrained by the value of $i$. Furthermore, unlike the cells with index $i$ and $k$ which are defined by an angle, the cells with index $j$ do not have a fixed size. To see this dependence on the value of $i$, lets consider the projection of the cells $(i, k)$ in the $xy$ plane, since $x = R\sin(\theta)\cos(\phi)$, $y = R\sin(\theta)\sin(\phi)$, and for a given $i$, $\theta = i\alpha$, the equations for $x$ and $y$ become

$$x = \tilde{r}\cos(\phi), \quad y = \tilde{r}\sin(\phi) \tag{E.8}$$

where $\tilde{r} = R\sin(i\alpha)$. But these are just the standard equations for the parametrisation in polar coordinates. Since $i$ is discrete these projections from circles of radii $r \leq R$ in the equatorial plane, with all the area enclosed between 2 consecutive circles belonging to cells with index $i$, see figure E.6. The values for $i = 1, 2, 3$ are only visible, since the values of $i = 4, 5, 6$ overlap these correspond to negative $z$ coordinate which yield the same projection in the $xy$ plane. By inversion symmetry the projection of cells for $i = 3, 4;\ i = 2, 5;\ i = 1, 6$ overlap. From the figure it can be seen that the values of $j$ are constrained according to

$$j = \begin{cases} 3 \mid 4 & \text{if } i = 1 \vee 6 \\ 2, 3 \mid 4, 5 & \text{if } i = 2 \vee 5 \\ 1, 2, 3 \mid 4, 5, 6 & \text{if } i = 3 \vee 4 \end{cases} \tag{E.9}$$

where $\mid$ is used to explicitly differentiate between $x < 0 \mid x > 0$. Generalising the above scheme for arbitrary $n$ we have $j_{min} \leq j \leq j_{max}$ where

$$j_{min} = \frac{n}{2} - \min(i - 1, n - i) \quad x < 0 \tag{E.10a}$$

$$j_{max} = \frac{n}{2} \quad x < 0 \tag{E.10b}$$

$$j_{min} = \frac{n}{2} + 1 \quad x > 0 \tag{E.10c}$$

$$j_{max} = \frac{n}{2} + \min(i, n - i + 1) \quad x > 0 \tag{E.10d}$$

where the min function has to be used to distinguish between cases of $i < \frac{n}{2}, i > \frac{n}{2}$. Using the discussion above of using multiples of $\alpha$ to determine the cuts in the $x$-axis, the bin edge of a cell $j$ is determined by

$$BE = R\cos((n - j)\alpha), \tag{E.11}$$

which combined with the conditions of E.10 on $i$ finally give a method for assigning a particle with coordinate $x_a$ to the cell $j$ according to:

$$x_a \in \text{cell (i,j,k) if } x < BE \wedge j \leq j_{max}(i) \tag{E.12}$$

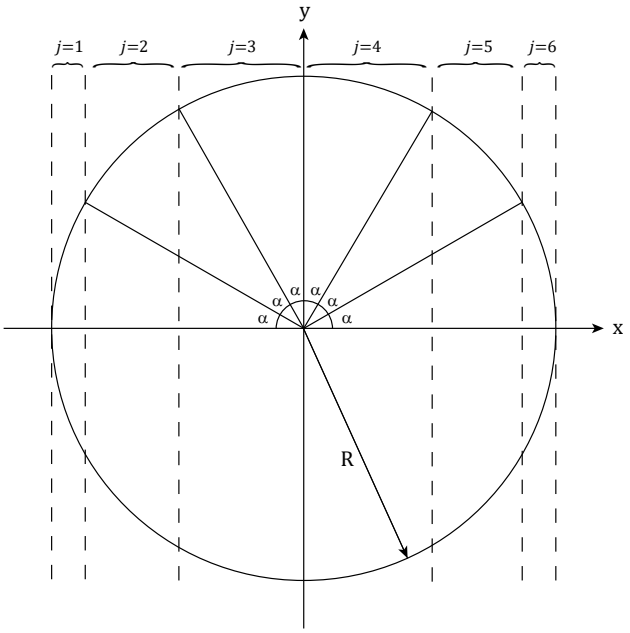


Figure E.5: Determination of the $j$ index value in the equatorial plane, where the projection of the sphere onto the $xy$ plane has a radius of $R$. Each cell boundary has an angular width $\alpha$, but in contrast to the $i$ and $k$ cell boundaries, the cells do not have a fixed size, but vary with $x$.

where the condition in equation (E.12) is evaluated starting at $j = j_{min}(i)$, and when not satisfied the value of $j$ is increased by 1 and the statement is reassessed.

Finally, now that $(i, j, k)$ can be determined, all that remains is to consider the values of $(i, j)$ for which an interaction with the other side of the sphere is possible. Again here the situation for $n = 6$ is considered and the results are then generalised to arbitrary $n$. The cell list for $n = 6$ is indicated in figure E.7. Interaction with the other side of the sphere become relevant if the cell $(i, j, 1)$ lies adjacent to cells of $(i, j, 2)$.

First consider the north pole where $i = 1$ and $j$ can take on the values $j = 3, 4$. Both cells are direct neighbours with their counterparts at the other side of the sphere and an interaction is possible. In the next layer of $i = 2$ $j$ can take on the values $j = 2, 3, 4, 5$. Visible at the western edge of the sphere is that the cell of $(2, 2, 1)$ is in contact with the cells $(1, 3, 2), (2, 2, 2), (3, 2, 2)$ at the other side and the cell $(2, 3, 1)$ is in contact with the cell $(2, 2, 2), (1, 4, 2)$, and thus for indices $j = 2, 3$ an interaction with the other side of the sphere is possible. Next for the layer of $i = 3$ the possible values for $j$ are $j = 1, 2, 3, 4, 5, 6$. Visible at the western edge of the sphere is that the cell of $(3, 1, 1)$ is in contact with the cells $(3, 1, 2), (4, 1, 2), (2, 2, 2)$ and the cell $(3, 2, 1)$ is in contact with the cell $(2, 2, 2)$. Thus the cells with an interaction with the other side of the sphere on the North-Western half of the hemisphere are obtained and listened in table E.1.

Due to the symmetry of the sphere, for cells beneath the equator this list is vertically mirrored, and for cells at the Eastern edge (not visible in figure due to orientation) the values of $j$ are merely shifted to $j' = n + 1 - j$ giving the full list of cells which can have an interaction with the other side of the sphere as in table E.2. Using the allowed values of $j$ on the west side of the

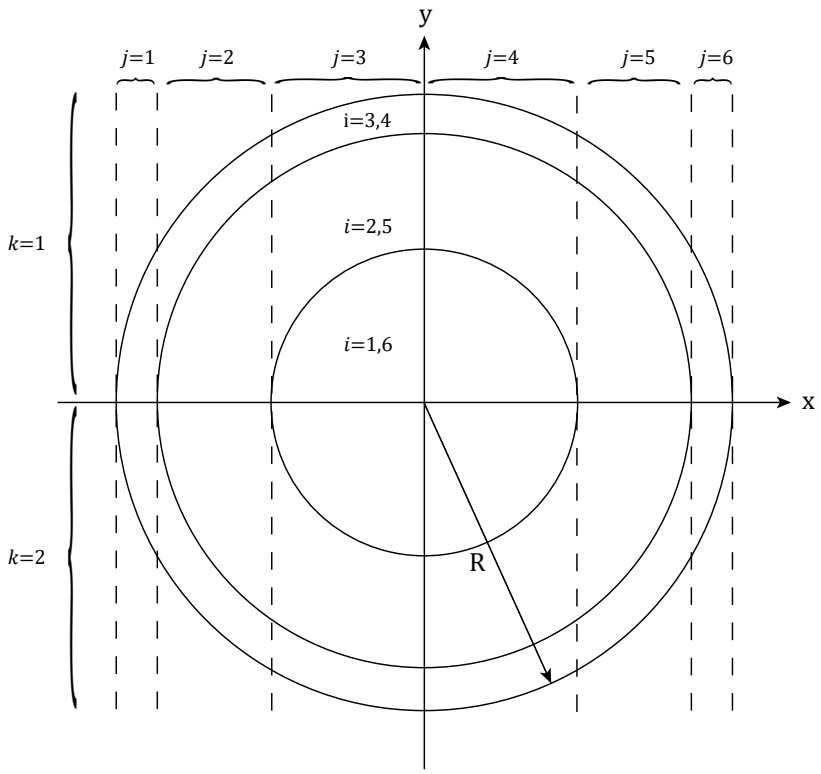


Figure E.6: Projection of the cell list onto the $xy$ plane, where the cells for $i = 1, 2, 3$ correspond to the drawn circles, but the cells for $i = 6, 5, 4$ have identical projections corresponding to the hemisphere of $z < 0$.

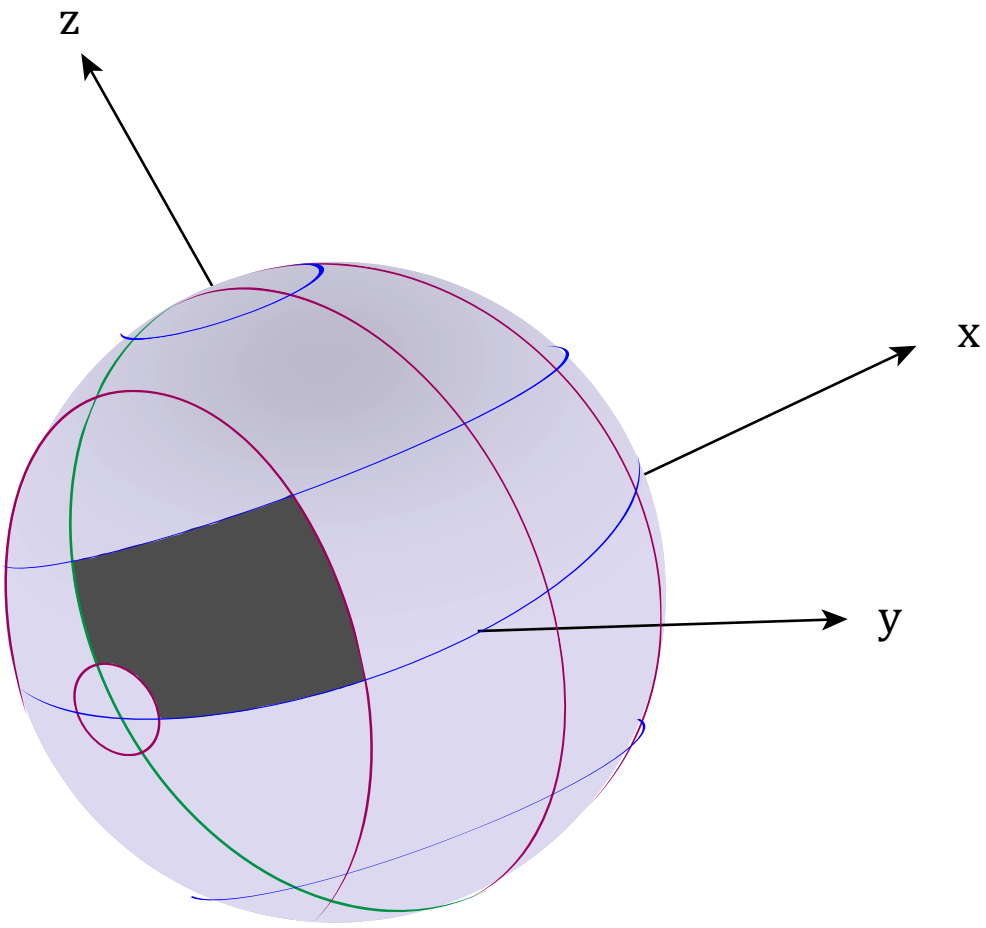


Figure E.7: Three dimensional representation of the cell listing on the surface of the sphere for $n = 6$. The blue lines correspond to the boundaries of cells with index $i$, the red lines correspond to the boundaries of cells with index $j$, and the green line is the boundary of cells with index $k$. Indicated in dark gray is the cell with index $(3, 2, 1)$.

Table E.1: List of $i$ and $j$ indices where interaction with the other side of possible, in the North-Western part of the hemisphere.

| $i$ index | Corresponding $j$ index |
|---|---|
| 1 | $3, 4$ |
| 2 | $2, 3$ |
| 3 | $1, 2$ |

Table E.2: List of $i$ and $j$ indices where interaction with the other side of possible, in the North-Western part of the hemisphere.

| $i$ index | Corresponding $j$ index west | Corresponding $j$ index east |
|---|---|---|
| 1 | $3, 4$ | $4, 3$ |
| 2 | $2, 3$ | $5, 4$ |
| 3 | $1, 2$ | $6, 5$ |
| 4 | $3, 4$ | $4, 3$ |
| 5 | $2, 3$ | $5, 4$ |
| 6 | $1, 2$ | $6, 5$ |

sphere the following rule is obtained

$$\frac{n}{2} \vee \frac{n}{2} + 2 = \begin{cases} i + j & \text{if } i \leq \frac{n}{2} \\ (n - i + 1) + j & \text{if } i \geq \frac{n}{2} + 1 \end{cases} \tag{E.13}$$

for cells which can have an interaction with the other side. Or by using the earlier states fact that at the east side of the hemisphere $j$ is given by $j' = n + 1 - j$, the general rule that interaction with the other side of the sphere is possible when

$$\min(i, n - i + 1) + \min(j, n - j + 1) = \frac{n}{2} + 1 \vee \frac{n}{2} + 2. \tag{E.14}$$

Which is precisely equation (3.7) as listed in section 3.3.
Finally in the 'bulk' it holds that the cell $(i, j, k)$ can have interactions with the cell $(i', j', k')$ where $i' \in \{i - 1, i + 1\}, j' \in j - 1, j + 1,$ and $k'$ determined by the condition in (E.14), however at the edges of the sphere $i - 1, i + 1, j - 1, j + 1$ make no sense at the North pole ($i = 1$), South pole ($i = n$), westernmost edge ($j = 1$) and easternmost edge ($j = n$), thus these conditions have to be replaced by $i'_{min} \leq i' \leq i'_{max},\ j'_{min} \leq j' \leq j'_{max},\ k'_{min} \leq k' \leq k'_{max}$ where

$$\begin{cases} i'_{min} = \min(1, i - 1) & \\ i'_{max} = \min(i + 1, n) & \\ j'_{min} = \min(1, j - 1) & \\ j'_{max} = \min(j + 1, n) & \\ k'_{min} = k'_{max} = k & \text{if (E.14)not holds} \\ k'_{min} = 1,\ k'_{max} = 2 & \text{if (E.14)holds} \end{cases} . \tag{E.15}$$

# Appendix F

# Supplementary data and results

In this appendix supplementary graphs for results are presented, which show the behaviour of the systems simulated, but not presented in chapter 4.

## F.1 Calibration

For the randomly initialised systems of $N = 122, 482, 752$ the defect evolution and MSD in the *passive static limit* are given in figure F.1. For the pre-relaxed magic number configurations of $N = 122, 482, 752$ the results are in figure F.2. With the exception of the randomly initialised $N = 122$ configuration, the order parameter asymptomatically reaches the $0.88 \sim 0.89$ value, whereas the $N = 122$ case only reaches a value of 0.80. This difference can be explained by considering the relative defect fraction (number of defects per particle), which is substantially higher in the $N = 122$ case (0.14) as compared to the $N = 482, 752$ cases $(0.11, 0.10)$, corresponding to less overall crystalline order. The $|\psi_6|$ results of the pre-relaxed magic number configurations can also be understood in terms of the relative defect fraction, since all these configurations have exactly 12 five-fold defects, the plateau value of $|\psi_6|$ will increase with particle number. Interestingly however is the case for the magic number of $N = 752$, which seems to increase rather than decrease from its initial value. Possible situations which can cause an increase in the bond orientational parameter are a decrease in the defects or a reorganisation at local particle level of bonds towards a more perfect hexagon. As the number of defects is constant only the latter option is possible and a visual inspection of the triangulation over time confirms that the crystal indeed reshapes from some coarse-grained hexagons to more fine-grained hexagons.

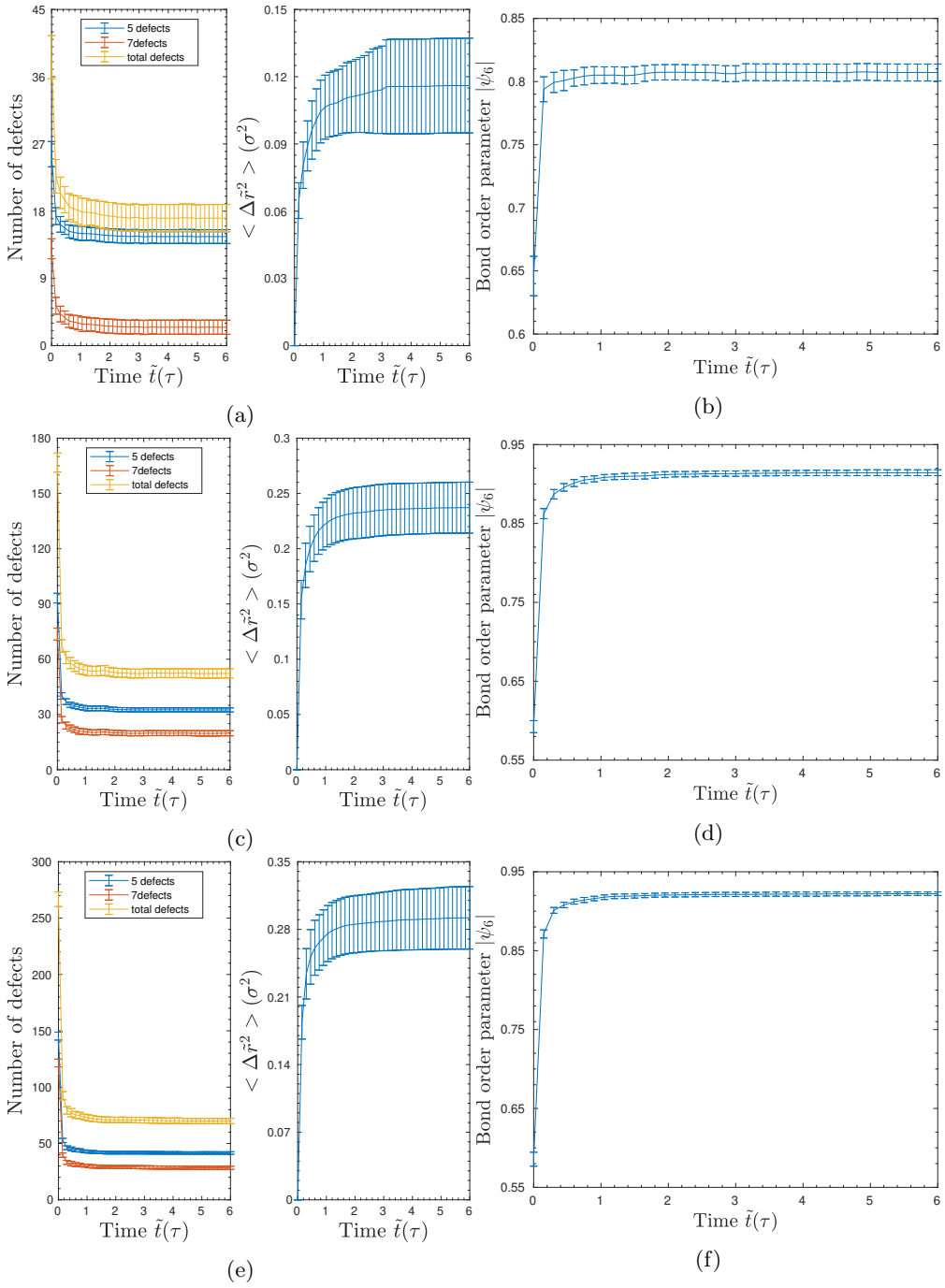


Figure F.1: Calibration results for the randomly intialised configurations of a)-b) 122 particles, c)-d) 482 particles, e)-f)752 particles. In the leftmost figure the number of defects and MSD are shown, in the rightmost figure the bond orientational order parameter $|\psi_6|$ is shown.

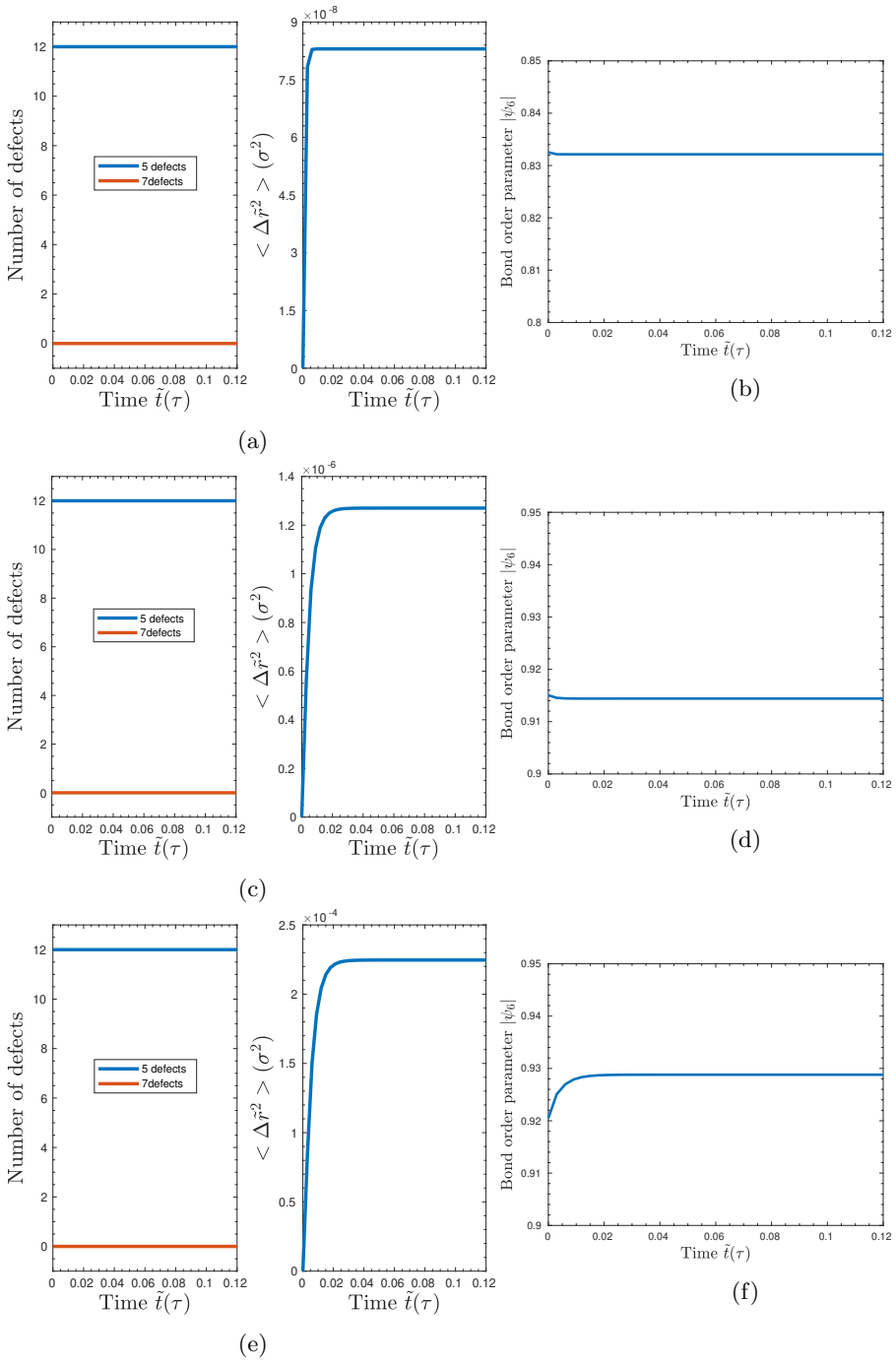


Figure F.2: Calibration results for pre-relaxed systems of a)-b) 122 particles, c)-d) 482 particles, e)-f) 752 particles. In the leftmost figure the number of defects and MSD are shown, in the rightmost figure the bond orientational order parameter $|\psi_6|$ is shown. For the defect figures the plot for the total defects is not shown, since for the magic number configurations this precisely coincides with the plot for the 5-fold defects.

## F.2 Activity

For the randomly initialised configurations of 300 and 800, the evolution of MSD and defect number, evolution of scar composition, and evolution correlation functions for the extremal cases of $F = 0.5$ and $F = 3.5$ are shown in figure F.3 and figure F.4 respectively. The behaviour of the bond orientational order parameter and polarisation order parameter as a function of activity are shown in figures F.5 and F.6 for 300 and 800 particles respectively. Just like the case of 500 particles, for low activity the number of defects remains constant after $200\tau$, but gradually decreases for high activity. In the low activity, the mean of the correlation functions follow the trends of being roughly 1 in case of the collective autocorrelation function and decreasing from 1 to $\frac{1}{3}$ for the self-part of the autocorrelation function. The uncertainties of both autocorrelation functions grow significantly over time due to the independent of the different random configurations where $\vec{\omega}$ traces out its own unique shape, similar to figure 4.9. The composition of scars shows a preference for larger scars over smaller scars as activity increases, and with the exception of dipole scars, only odd scar lengths are encountered. The surprisingly large number of dipole scars for 800 particles is confirmed by visual inspection to stem directly from the crystal structure itself. Many larger sized scars have a small dipole scar as a tail directly surrounding them, with a single hexagonal unit connecting the dipole scar and the larger scar, with the dipole and scar taking opposite vertices, see figure F.7. These relatively many defect dipoles are also reported in literature and emerge for larger spheres as the curvature becomes smaller [14]. For both system sizes, activity does increase the crystallinity of the lattice, as seen by the slight, but noticeable growth in $|\psi_6|$ which increases monotically with the self-propulsion strength.

For the remaining magic number configurations of $122, 272, 752$ particles, the number of defects remained 12 five-fold defects throughout all 30 independent realisations for orientation vectors at all considered self-propulsion strengths, also resulting in an identically constant behaviour of the bond orientational order parameter $|\psi_6|$ for all considered activity, see figure F.8. Remarkably, the plateau value of $|\psi_6|$ in each case is close to their respective plateau values in the *passive static limit* as described in above. Plots of the MSD, total defects and correlation functions can be found in figures F.9, F.10 , and F.11 respectively for $122, 272, 752$ particles. An interesting property of the magic number configurations at high activity can be seen in the autocorrelation function for the collective rotation, which unlike the completely randomised configurations does not have a monotonically increasing uncertainty, but can in fact even decrease, although the exact cause of this is unknown. The polarisation order parameter $\psi_p$ in each case shows the usual fluctuations and remains close to zero, ruling out the possibility of any alignment interaction, see figure F.8.

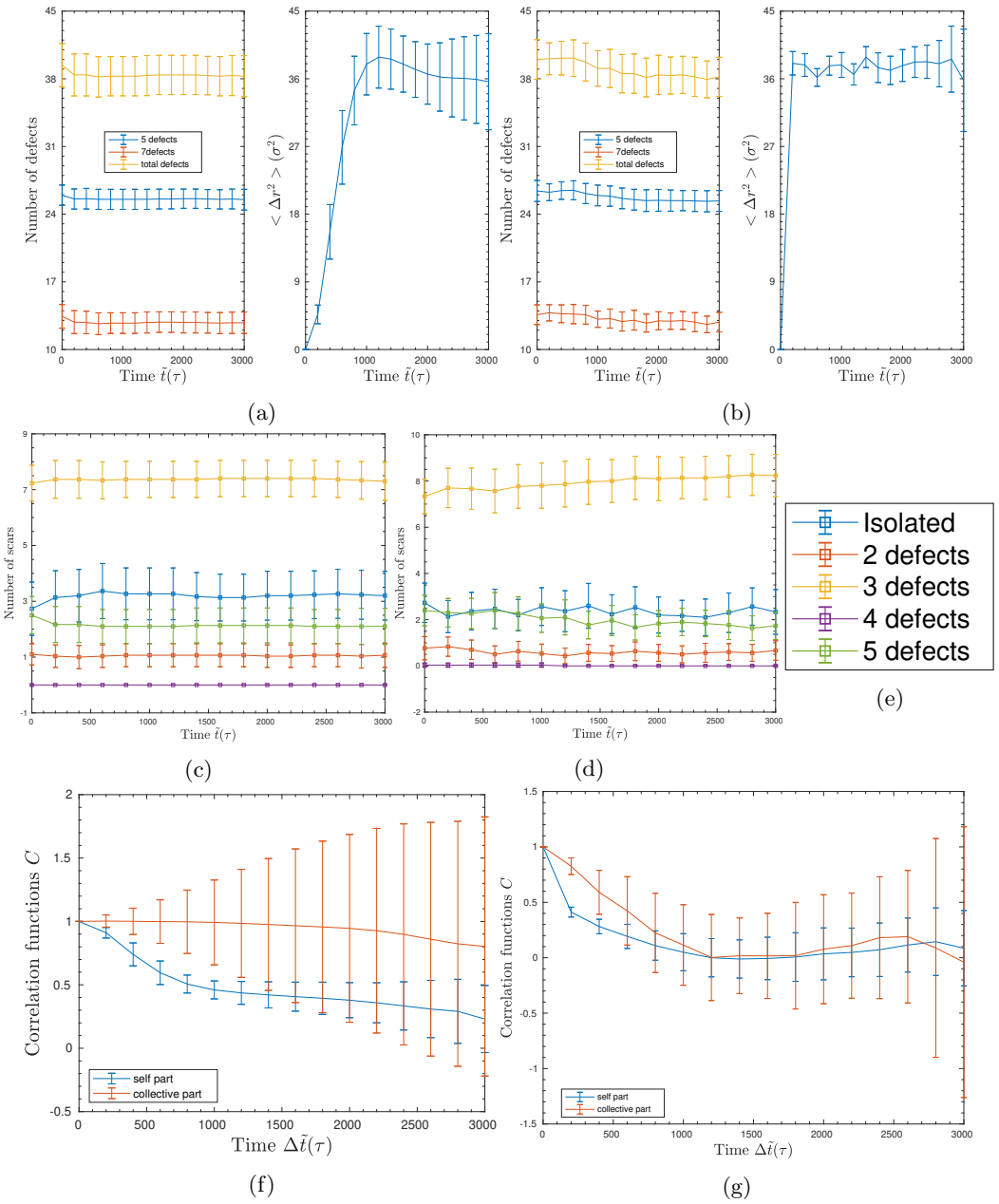


Figure F.3: Results of activity simulations for the the randomly initialised system of 300 athermal active particles (corresponding to $T^\star = 0$), showing a)-b): evolution of defects and MSD, c)-d): the composition of scars, f)-g): the correlation functions for the collective angular velocity and individual normalised angular velocities. The legend in figure e) applies to the scar composition plots of figures c)-d). Figures in the left column correspond to the extremal case of $F = 0.5$ and figures in the right column correspond to the extremal case of $F = 3.5$.

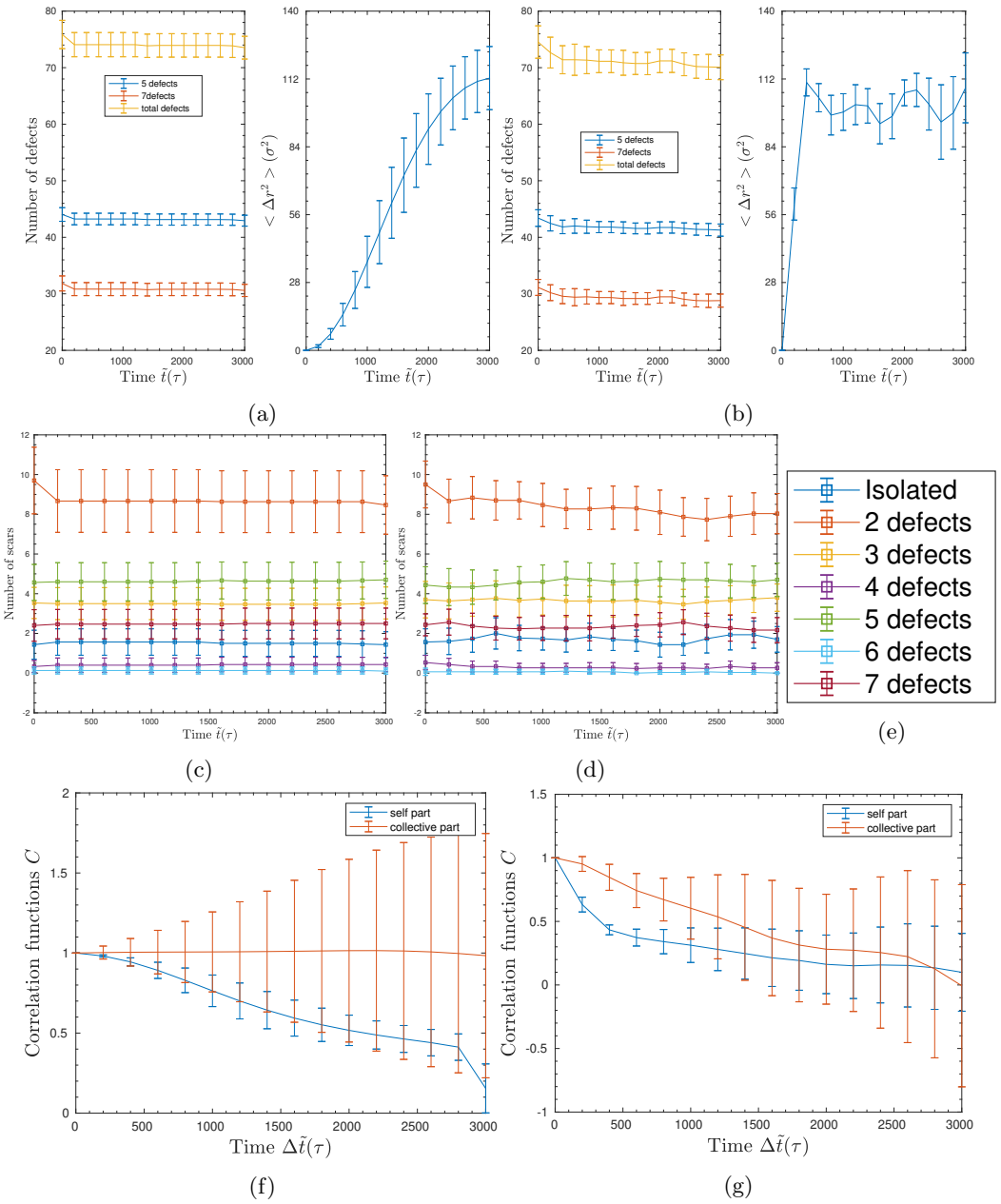


Figure F.4: Results of activity simulations for the the randomly initialised system of 800 athermal active particles (corresponding to $T^\star = 0$), showing a)-b): evolution of defects and MSD, c)-d): the composition of scars, f)-g): the correlation functions for the collective angular velocity and individual normalised angular velocities. The legend in figure e) applies to the scar composition plots of figures c)-d). Figures in the left column correspond to the extremal case of $F = 0.5$ and figures in the right column correspond to the extremal case of $F = 3.5$.

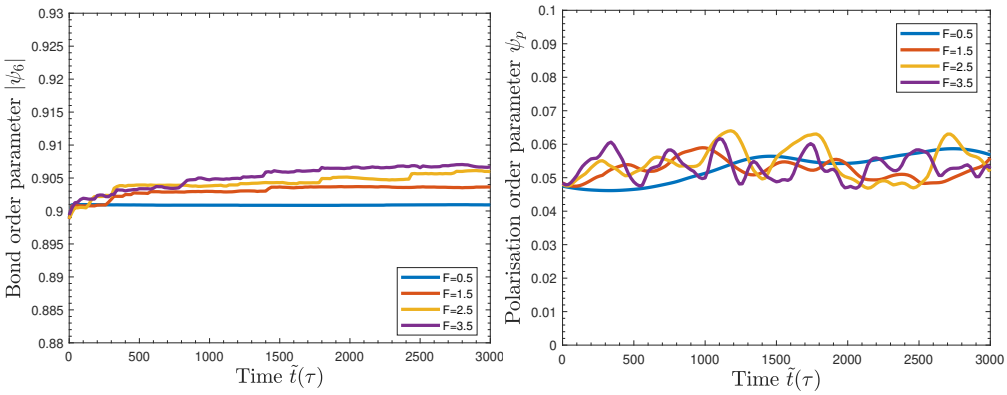


(a) (b)

Figure F.5: Behaviour of the order parameters as function of activity for 300 athermal active particles (corresponding to $T^\star = 0$), showing a) the bond orientational order parameter $|\psi_6|$, and b) the polarisation order parameter $\psi_p$. Errorbars have been suppressed for visibility.

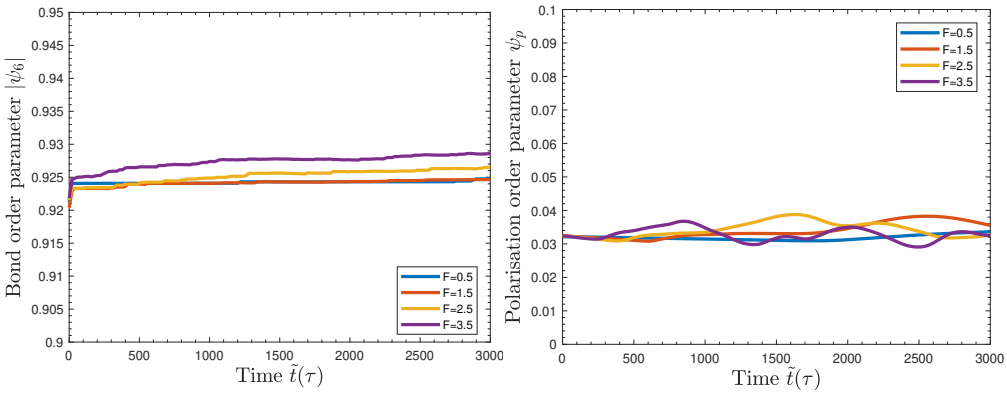


(a) (b)

Figure F.6: Behaviour of the order parameters as function of activity for 800 athermal active particles (corresponding to $T^\star = 0$), showing a) the bond orientational order parameter $|\psi_6|$, and b) the polarisation order parameter $\psi_p$. Errorbars have been suppressed for visibility.

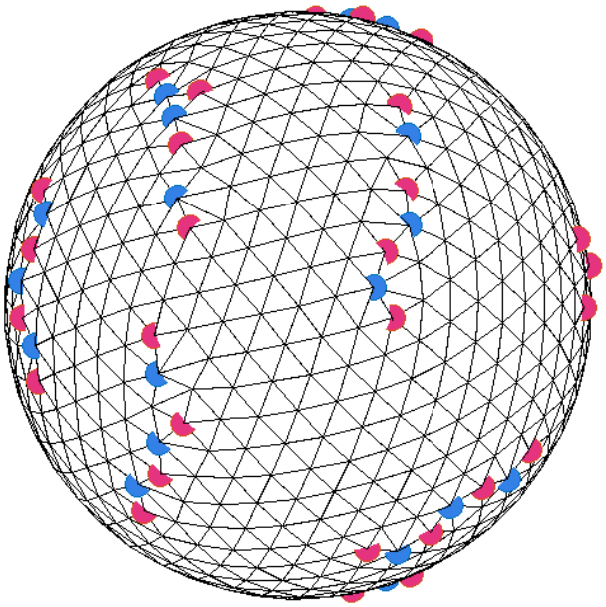

Figure F.7: Triangulated crystal and defects, clearly showing the existence of tails of dipole defects after larger scars, explaining the relatively large number of dipole scars. Both the dipole and scar terminate as opposing vertices of a regular hexagonal unit.

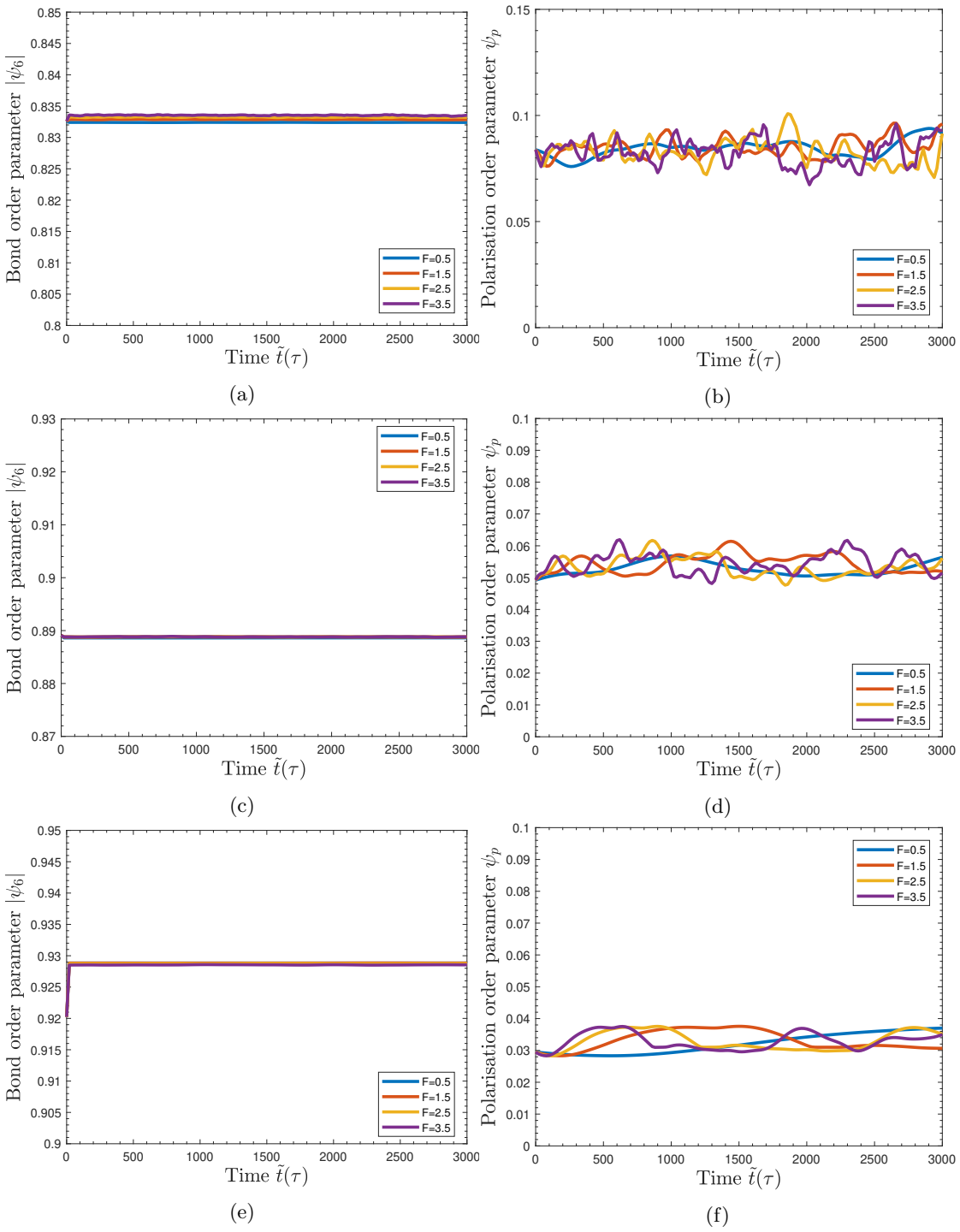


Figure F.8: Behaviour of the bond orientational order parameter $|\psi_6|$ and polarisation order parameter $\psi_p$ as a function of activity for the magic number configurations at $T^\star = 0$ of a)-b) 122 particles, c)-d) 272 particles, and e)-f) 752 particles. Plateau values of $|\psi_6|$ roughly correspond to their *passive static limit* counterpart values.

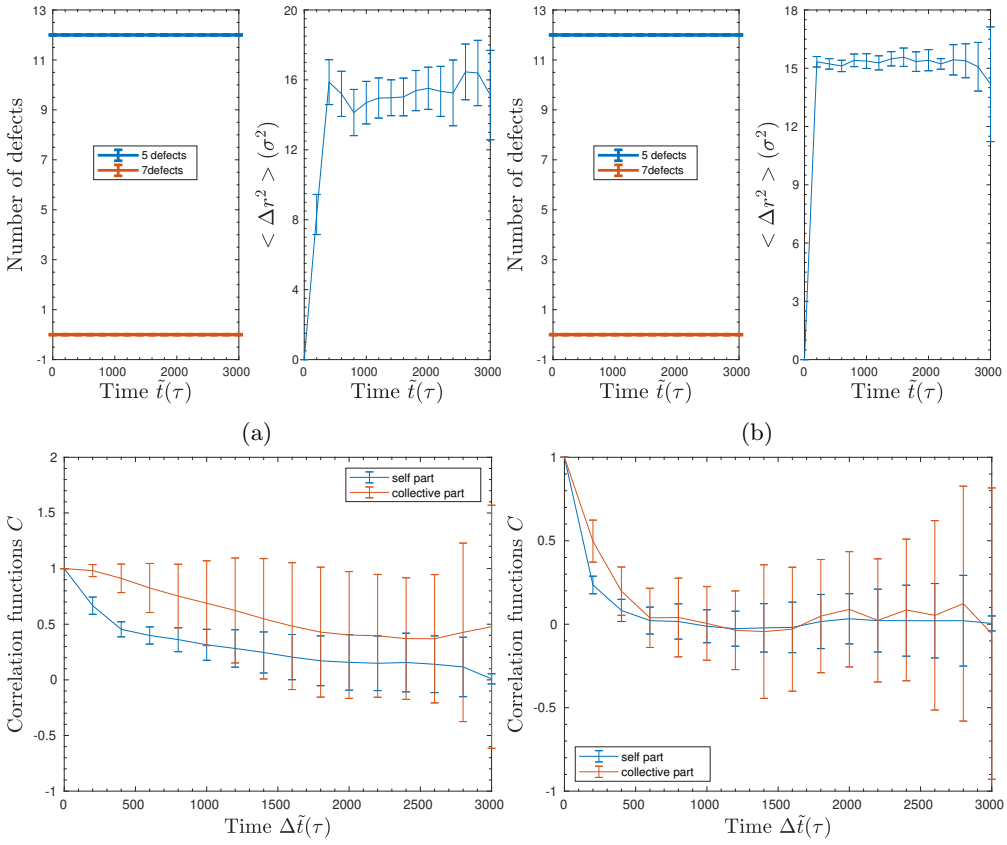


Figure F.9: Results of activity simulations for the magic number configuration of 122 athermal active particles (corresponding to $T^\star = 0$), showing a)-b) evolution of MSD and defects, c)-d) correlation functions for the collective angular velocity and individual normalised angular velocities. Figures in the left column correspond to the extremal case of $F = 0.5$, and figures in the right column correspond to the extremal case of $F = 3.5$. In figures a) and b) the plot for the total number of defects is not shown as this coincides with the plot for the 5-fold defects.

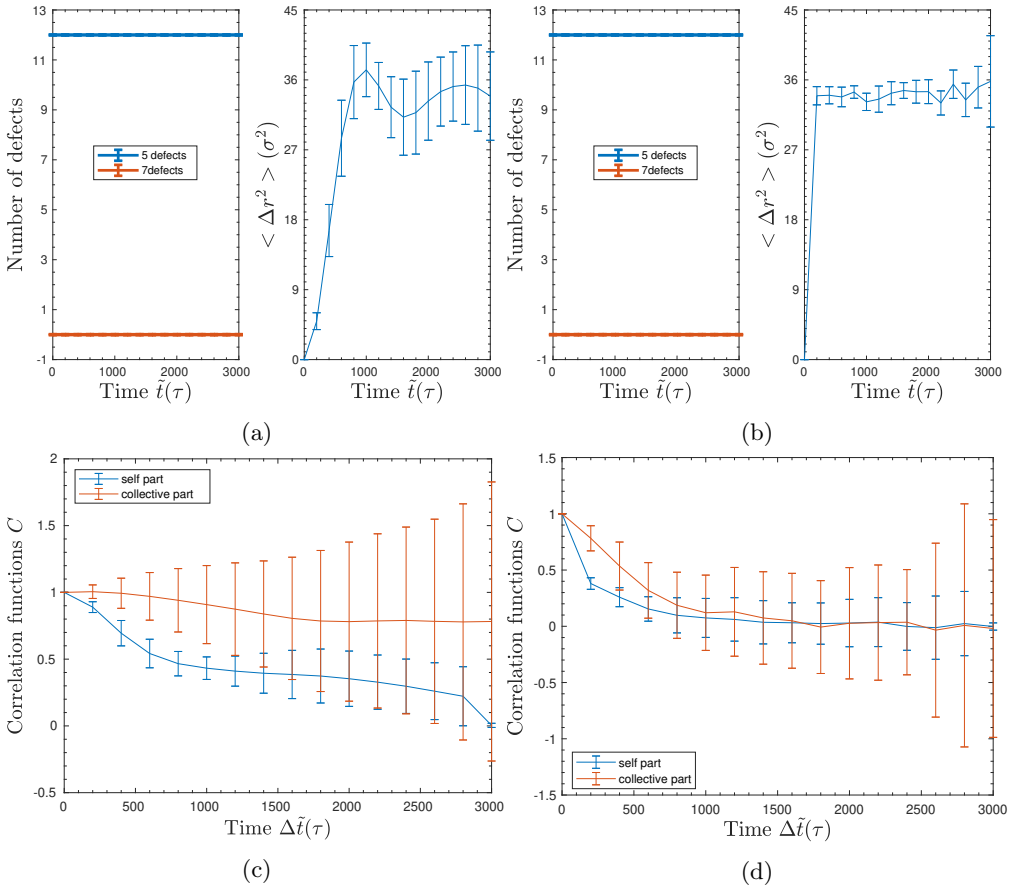


Figure F.10: Results of activity simulations for the magic number configuration of 272 athermal active particles (corresponding to $T^\star = 0$), showing a)-b) evolution of MSD and defects, c)-d) correlation functions for the collective angular velocity and individual normalised angular velocities. Figures in the left column correspond to the extremal case of $F = 0.5$, and figures in the right column correspond to the extremal case of $F = 3.5$. In figures a) and b) the plot for the total number of defects is not shown as this coincides with the plot for the 5-fold defects.

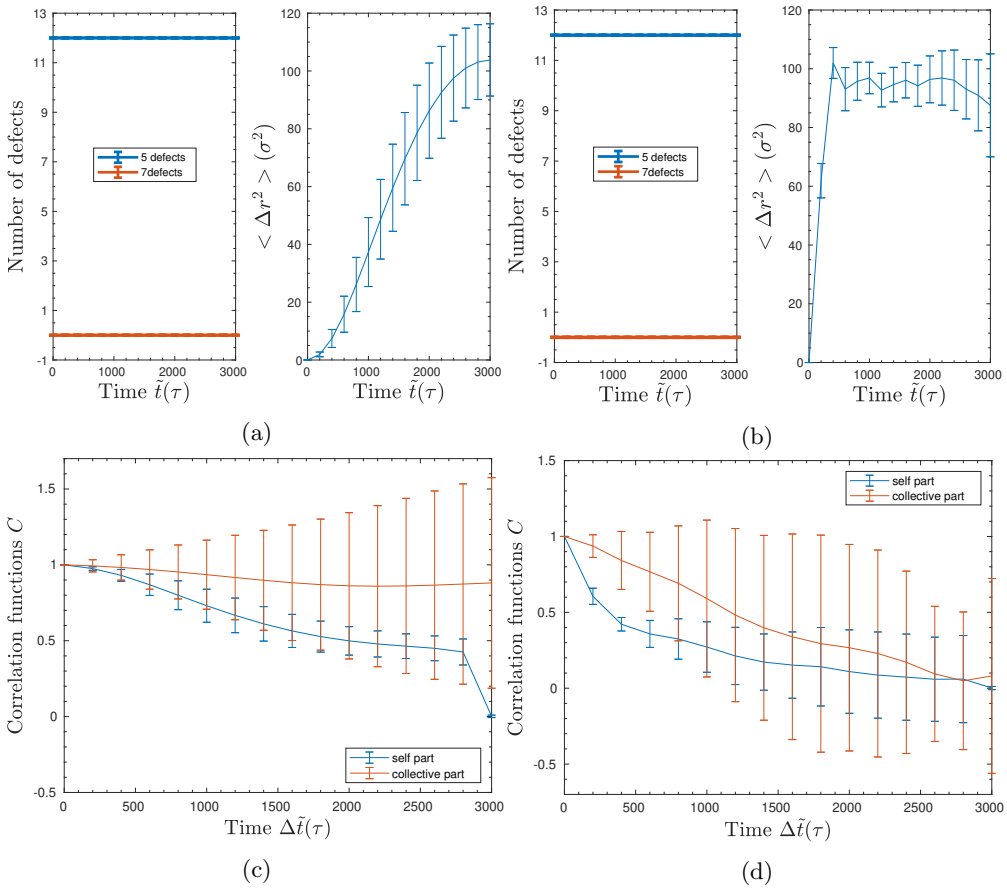


Figure F.11: Results of activity simulations for the magic number configuration of 752 athermal active particles (corresponding to $T^\star = 0$), showing a)-b) evolution of MSD and defects, c)-d) correlation functions for the collective angular velocity and individual normalised angular velocities. Figures in the left column correspond to the extremal case of $F = 0.5$, and figures in the right column correspond to the extremal case of $F = 3.5$. In figures a) and b) the plot for the total number of defects is not shown as this coincides with the plot for the 5-fold defects.

## F.3 Temperature

For the randomly initialised configurations of $N = 300, 800$ increasing the temperature results in a decrease of the total defects, with a stronger decrease for $N = 800$ than for $N = 300$ which is due to the fact that the net topological charge must be +2 which must be satisfied by both scars and isolated defects, rendering fewer options for reorganising scars available for small systems. For $N = 300$ this boils to a transition from $\sim 10$ scars of length 3, $\sim 1$ isolated defects and $\sim 1$ scar of length 5 to $\sim 11$ scars of length 3 and $\sim 1$ isolated defects. In the low temperature case $\sim 1$ defect dipole is present, which is suppressed in the high temperature case as a defect dipole has a net topological charge of 0 and only adds strain to the crystal without aiding in screening the curvature of the sphere. This behaviour is also visible for $N = 800$ where the number of defect dipoles is initially high due to the tailing of defect dipoles behind scars as discussed above, but

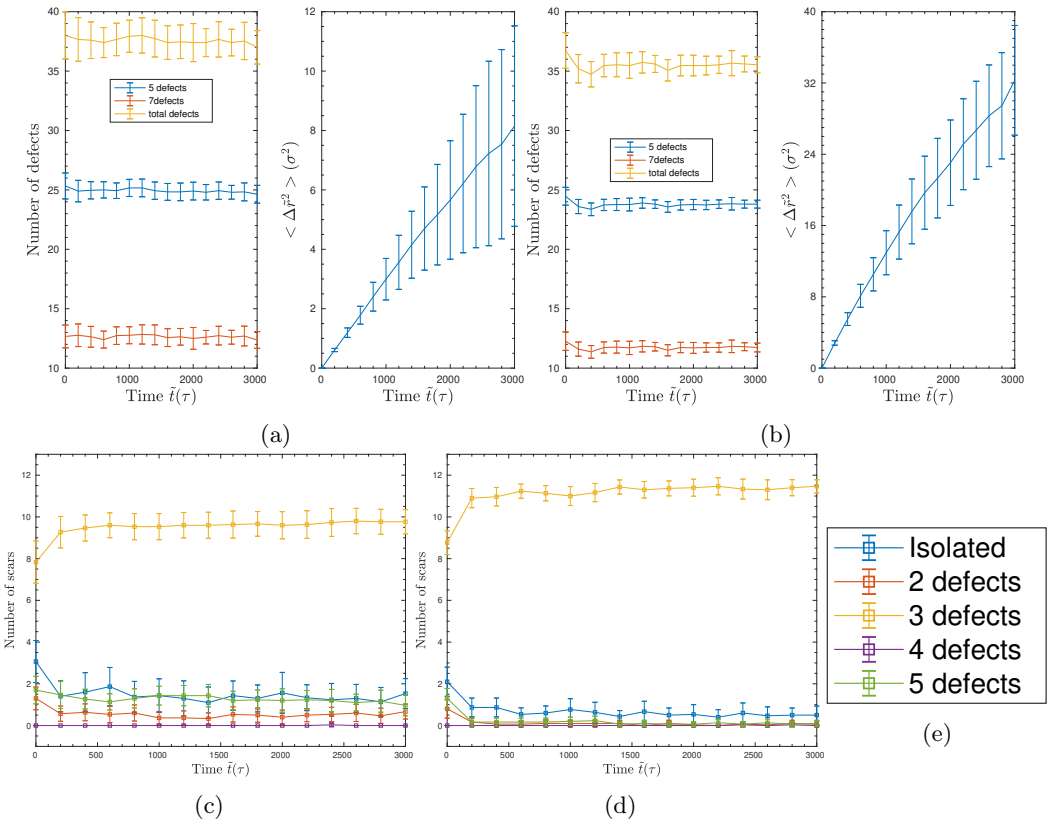


Figure F.12: Results of temperature simulations for $N = 300$ passive Brownian particles (corresponding to $F = 0$), showing a)-b) evolution of MSD and defects, and c)-d) composition of scars. Figures in the left column correspond to the extremal case of $T^\star = 0.5$, and figures in the right column correspond to the extremal case of $T^\star = 2.5$. The legend in figure e) applies to the plots of the scar composition of figures c)-d).

is quenched for higher temperatures. Combined with the results for $N = 500$ particles discussed in 4.3, the intuitive that larger scars can be sustained by larger systems is easily obtained by comparing figures F.12 F.13 4.21. Overall the effects of temperature on the randomly initialised configurations of particles is a reduction in hexagonal crystallinity reflected in a reduction of $|\psi_6|$, and a chaotically fluctuating random order as reflected in the polarisation order parameter $\psi_p$, see figure

For the magic numbers of $N = 122, 272, 752$ temperature has a non uniform effect in contrast to activity. Over all 30 independent realisations for fluctuations the effects of temperature are identical, however the effect of temperature is dependent on the system size. In each case however, for the lowest temperature considered $T^\star = 0.5$ the number of defects remained 12. For the the smallest magic number of 122 the number of defects remained virtually 12 throughout the full temperature range, where only at the highest temperature of $T^\star = 2.5$, fluctuations were strong enough to momentarily generate additional defects, turning some of the isolated defects into scars of length 3, but in each case, the restoring power of the potential is able to revert the system back to its original state, see figure F.16. This behaviour is also reflected in the bond

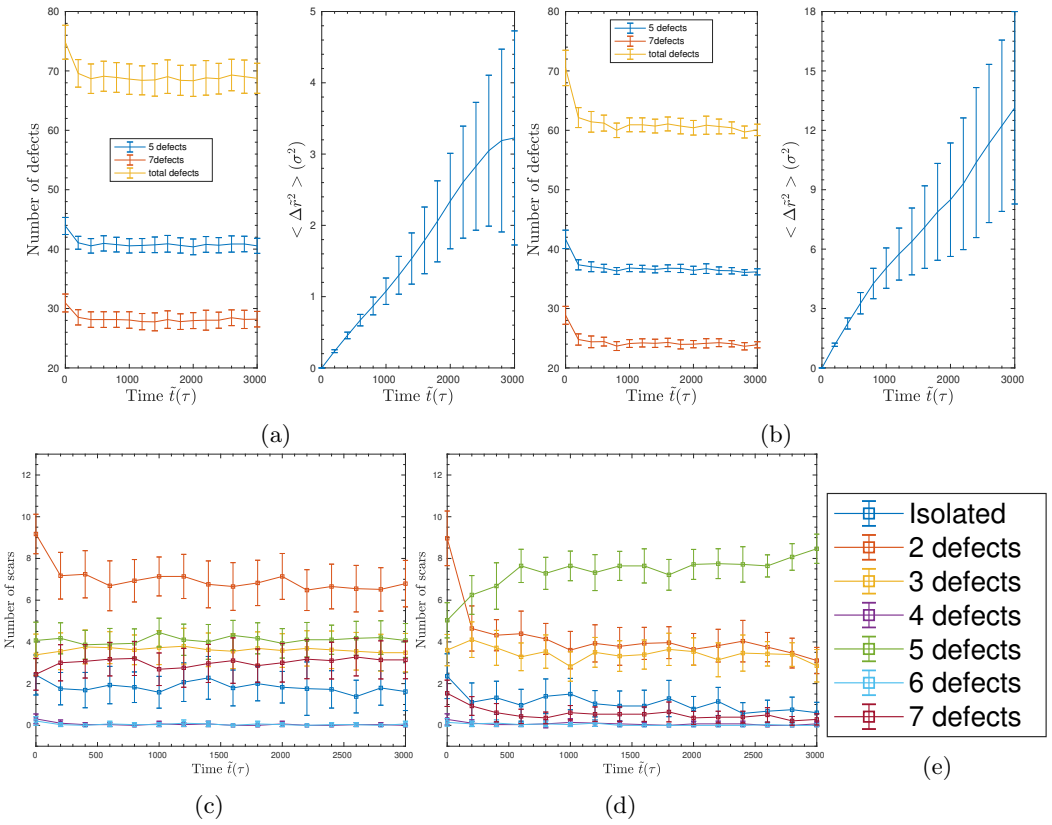


Figure F.13: Results of temperature simulations for $N = 800$ passive Brownian particles (corresponding to $F = 0$), showing a)-b) evolution of MSD and defects, and c)-d) composition of scars. Figures in the left column correspond to the extremal case of $T^\star = 0.5$, and figures in the right column correspond to the extremal case of $T^\star = 2.5$. For the case of $T^\star = 0.5$ 1 realisation became unstable over the simulation and was not considered in data analysis, whereas for the case of $T^\star = 2.5$ 2 realisations became unstable and were not considered in data analysis. The legend in figure e) applies to the plots of the scar composition of figures c)-d).

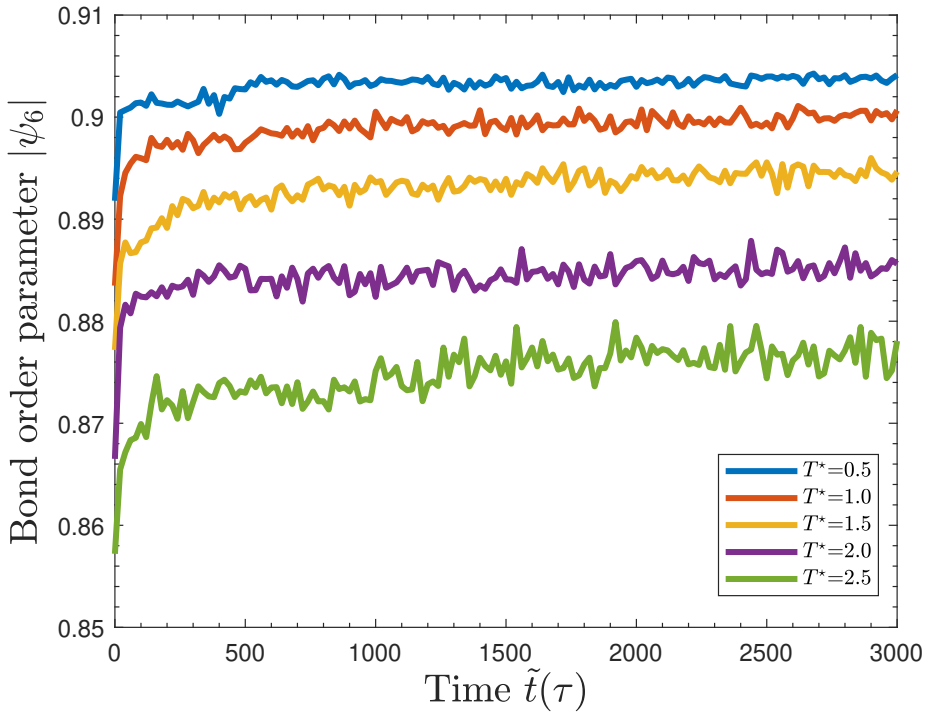


(a)

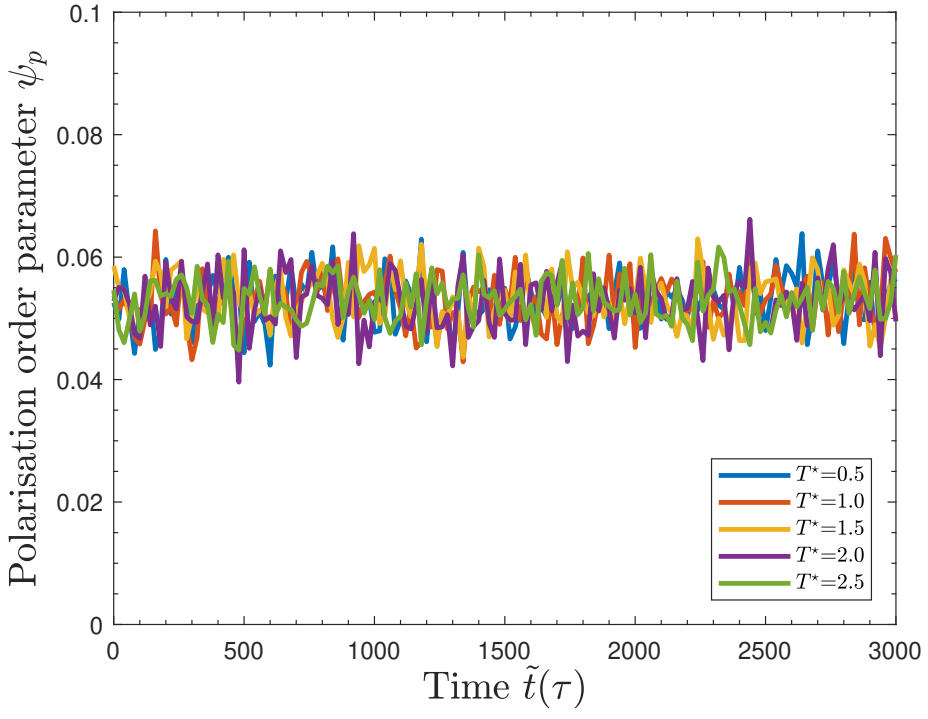


(b)

Figure F.14: Order parameters for the temperature simulations for the randomly initialised system of 300 particles, showing a) the bond orientational order parameter $|\psi_6|$, and b) the polarisation order parameter $\psi_p$.

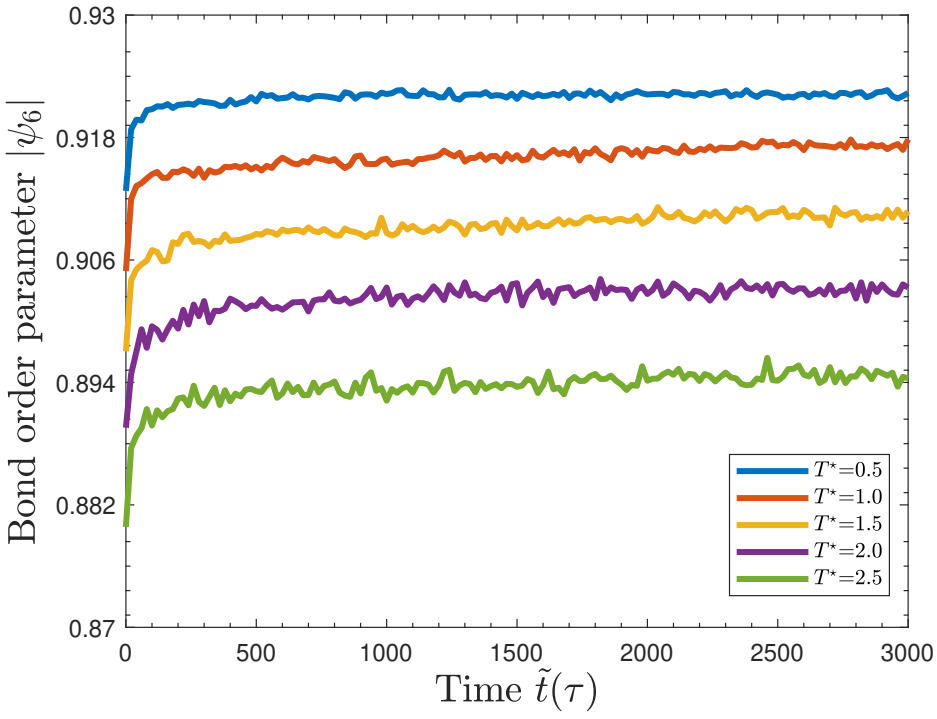


(a)

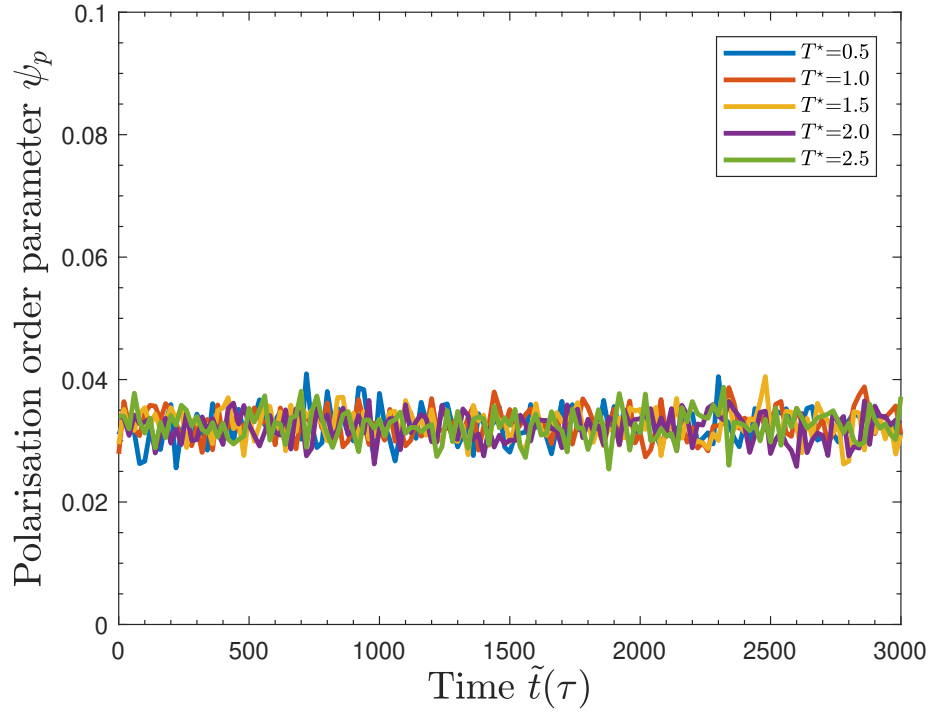


(b)

Figure F.15: Order parameters for the temperature simulations for the randomly initialised system of 800 particles, showing a) the bond orientational order parameter $|\psi_6|$, and b) the polarisation order parameter $\psi_p$.

orientational order parameter, which after a short decrease at all temperatures remains steady at low temperatures, but fluctuates increasingly around a steady value higher temperatures, see figures F.17. For the magic number system of 272 particles, for temperatures of $T^\star = 1.5$ and above, scars of length 3 can be sustained without the potential being able to restore the lattice. For increased temperature, scars of greater length do no occur, but the number of scars of length 3 increases, see figure F.18. This behaviour is also represented by the bond orientational order parameter, which decreases initially for all temperatures, but then stays approximately constant for $T^\star = (0.5, 1.0)$, whereas for higher temperature $|\psi_6|$ increases after the initial decrease, consistent with the discussion in section 4.3, see figure F.19. For the largest system of 752 particles, the number of isolated defects sharply decreases with increasing temperatures, with scars of length 3 and 5 predominantly emerging, with an increasing dominance of scars of length 5 over scars of length 3, see figure F.20. The emergence of defect dipoles is due to the fact that scars of length 5 are relatively unstable, and tend to constantly reorganise from a stretched out linear chain, to a compact triangle, or break into a scar of length 3 and a defect dipole. This constant reformation and breaking is also the reason for the observed monotonic decrease in $|\psi_6|$, although small scars can increase $|\psi_6|$ by lifting the deformations on hexagonal units, larger scars will eventually destroy this healing effect, since their presence influences a large section of the surrounding lattice to induce additional deformations, see figure F.21.

For both the randomly initialised configurations and magic number configurations the MSD starts of in the diffusive regime, but subdues into the sub-diffusive regime as the restoring power of the potential does not allow the particles to move about freely, with increasing size of the MSD as temperature increases, as expected for stronger fluctuations. Furthermore, the larger the systems size, the longer the diffusive regime holds because of the increased dynamical complexity of the fluctuations.

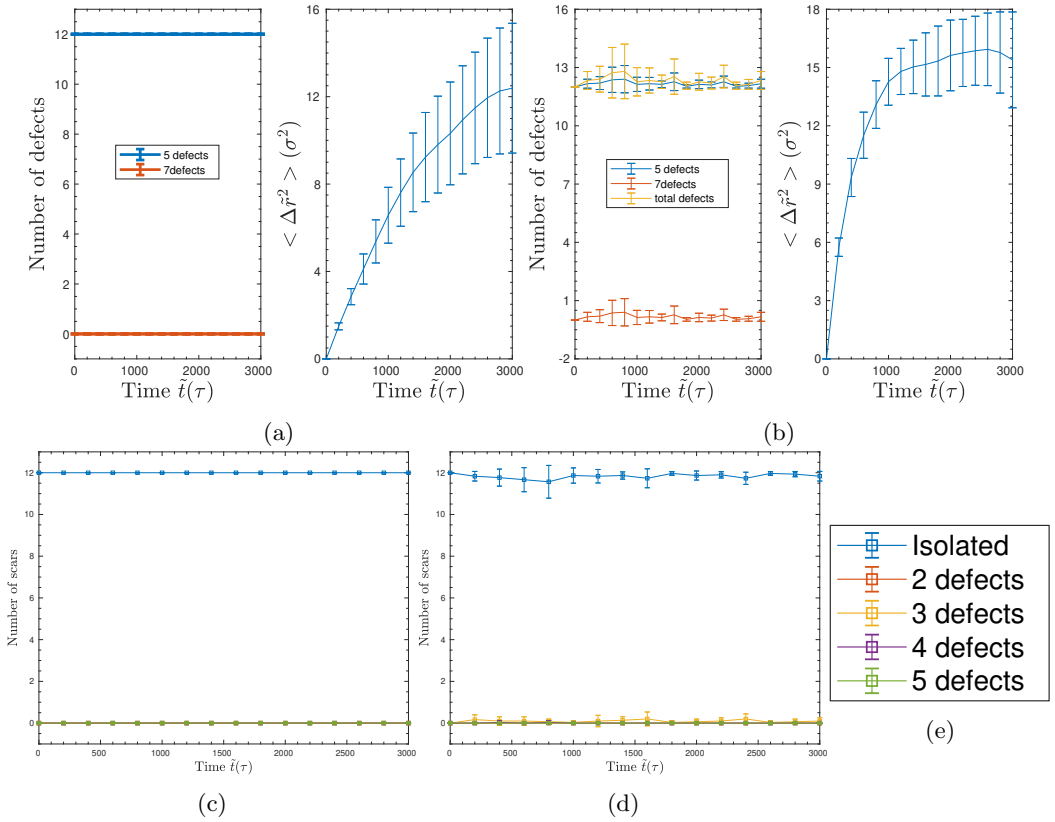


Figure F.16: Results of temperature simulations for the magic number configuration of 122 passive Brownian particles (corresponding to $F = 0$) , showing a)-b) evolution of MSD and defects, and c)-d) composition of scars. Figures in the left column correspond to the extremal case of $T^\star = 0.5$, and figures in the right column correspond to the extremal case of $T^\star = 2.5$. In figure a) the plot for the total number of defects is not shown as this coincides with the plot for the 5-fold defects. The legend in figure e) applies to the plots of the scar composition of figures c)-d). Small deviations from precisely 12 five-fold defects by a formation of a scar can be seen as a result from the Brownian motion of the lattice at high temperature, but these are quickly quenched back to a five-fold defect..

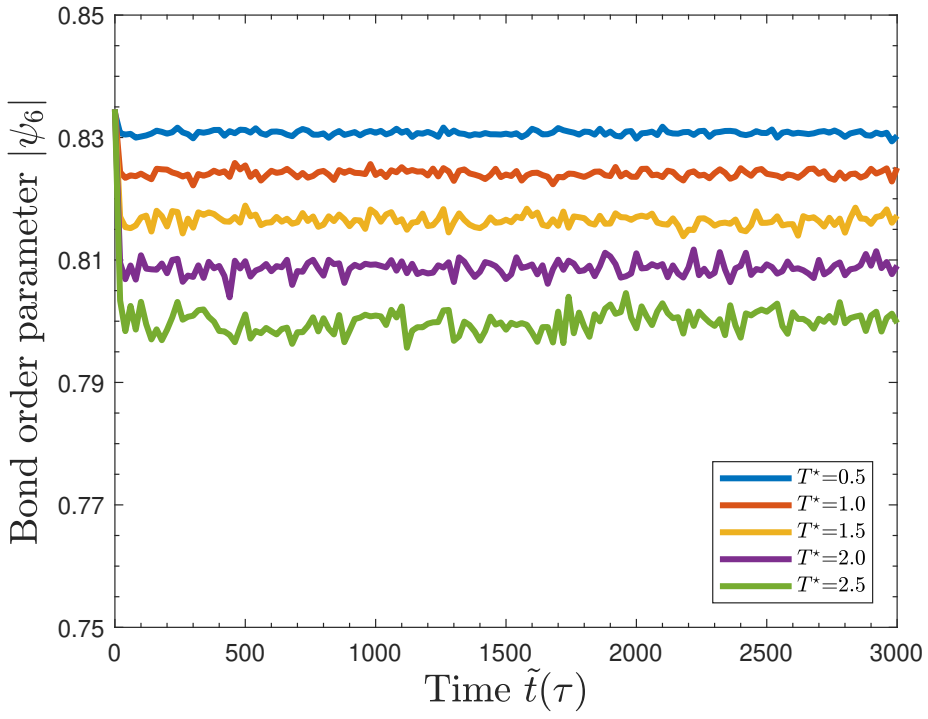


(a)

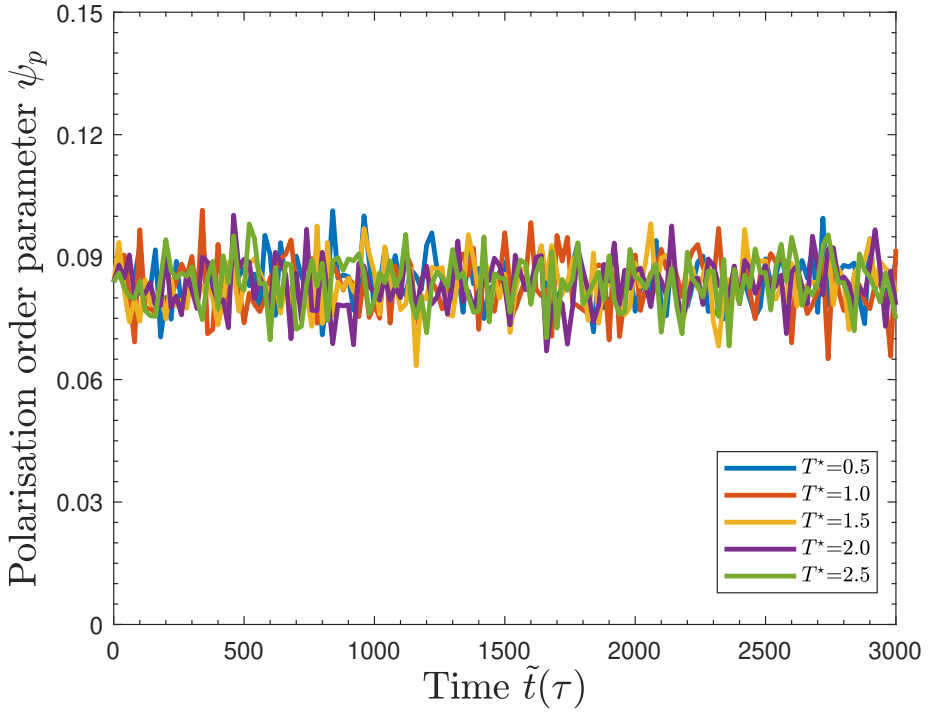


(b)

Figure F.17: Order parameters for the temperature simulations on the magic number configuration of 122 passive Brownian particles (corresponding to $F = 0$), showing a) the bond orientational order parameter $|\psi_6|$, and b) the polarisation order parameter $\psi_p$.

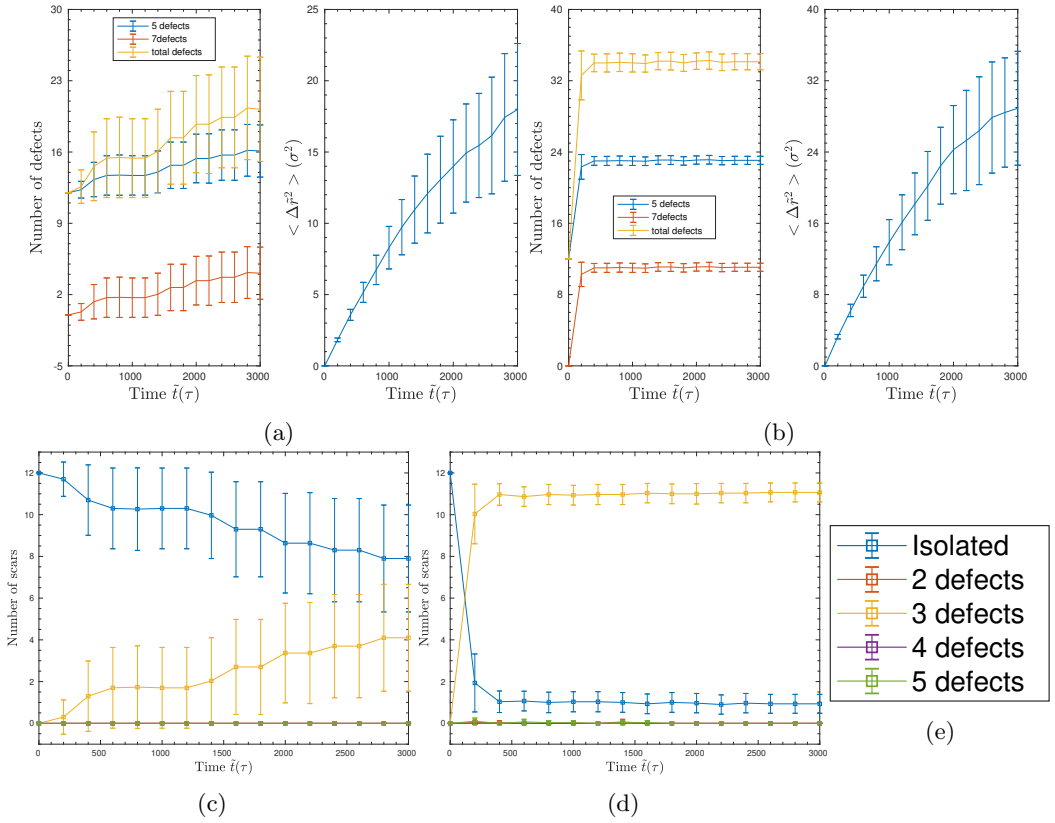


Figure F.18: Results of temperature simulations for the magic number configuration of 272 passive Brownian particles (corresponding to $F = 0$), showing a)-b) evolution of MSD and defects, and c)-d) composition of scars. Figures in the left column correspond to the case of $T^\star = 1.5$ where scars first start to form, and figures in the right column correspond to the extremal case of $T^\star = 2.5$. The legend in figure e) applies to the plots of the scar composition of figures c)-d).

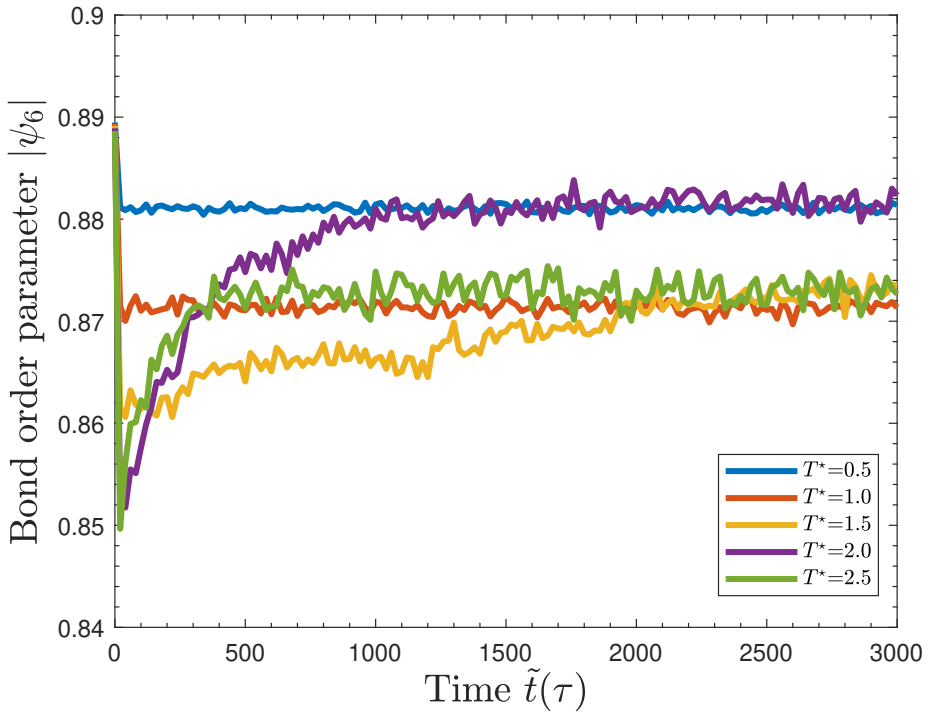


(a)

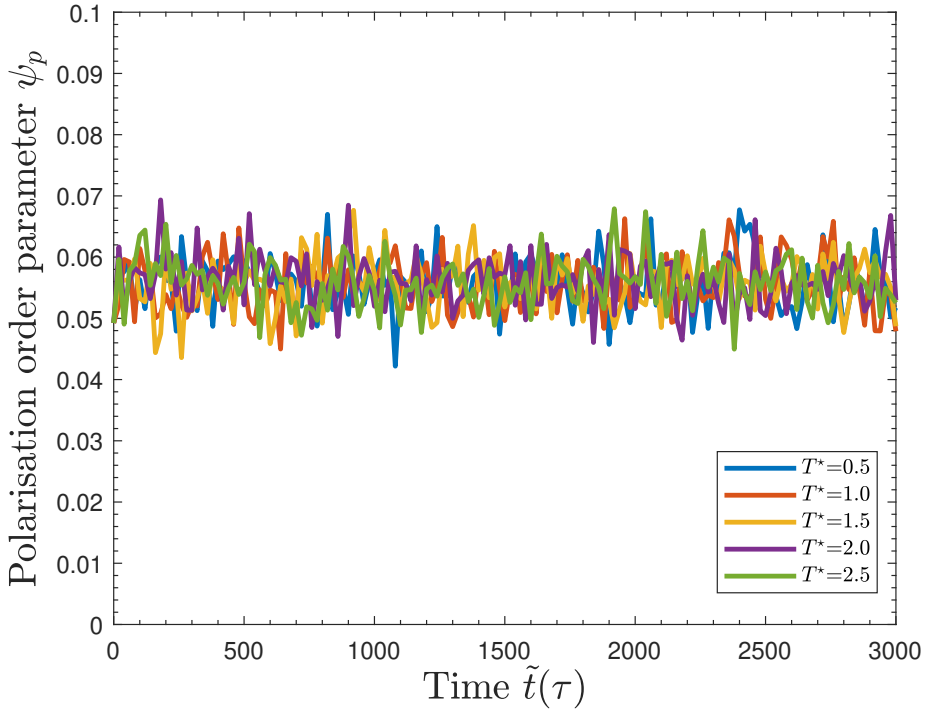


(b)

Figure F.19: Order parameters for the temperature simulations on the magic number configuration of 272 passive Brownian particles (corresponding to $F = 0$) , showing a) the bond orientational order parameter $|\psi_6|$, and b) the polarisation order parameter $\psi_p$.

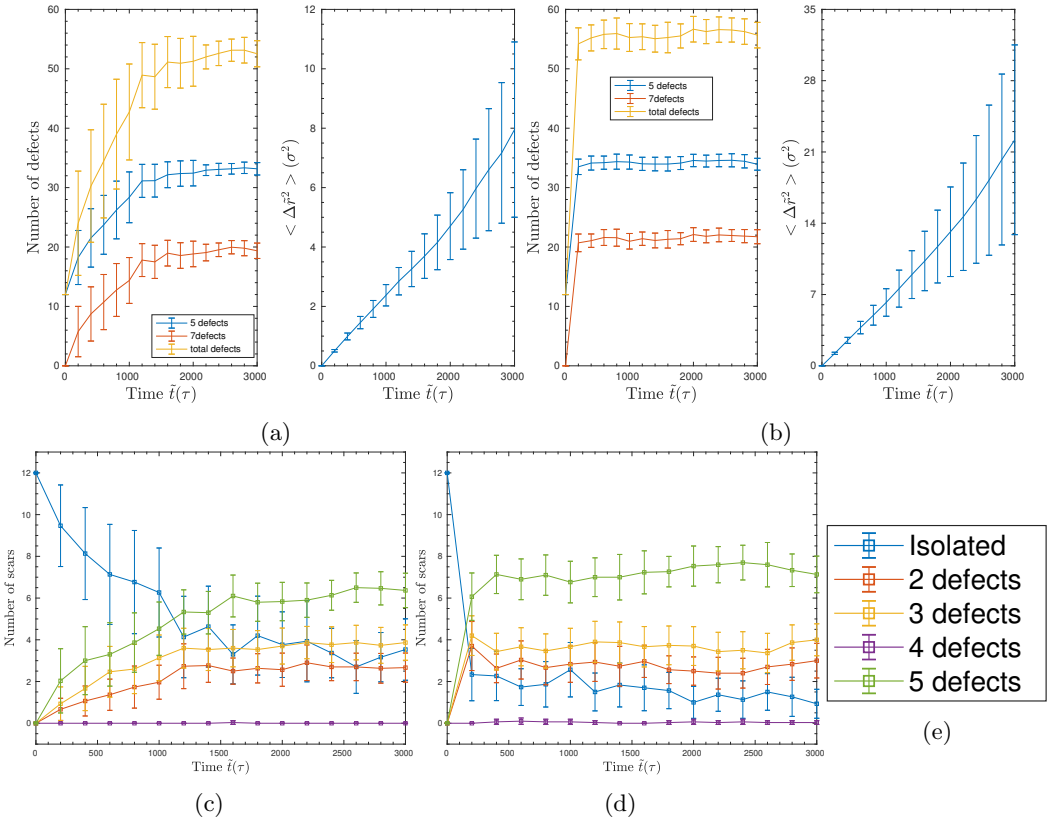


Figure F.20: Results of temperature simulations for the magic number configuration of 752 passive Brownian particles (corresponding to $F = 0$), showing a)-b) evolution of MSD and defects, andls c)-d) composition of scars. Figures in the left column correspond to the case of $T^\star = 1.0$ where scars first start to form, and figures in the right column correspond to the extremal case of $T^\star = 2.5$.

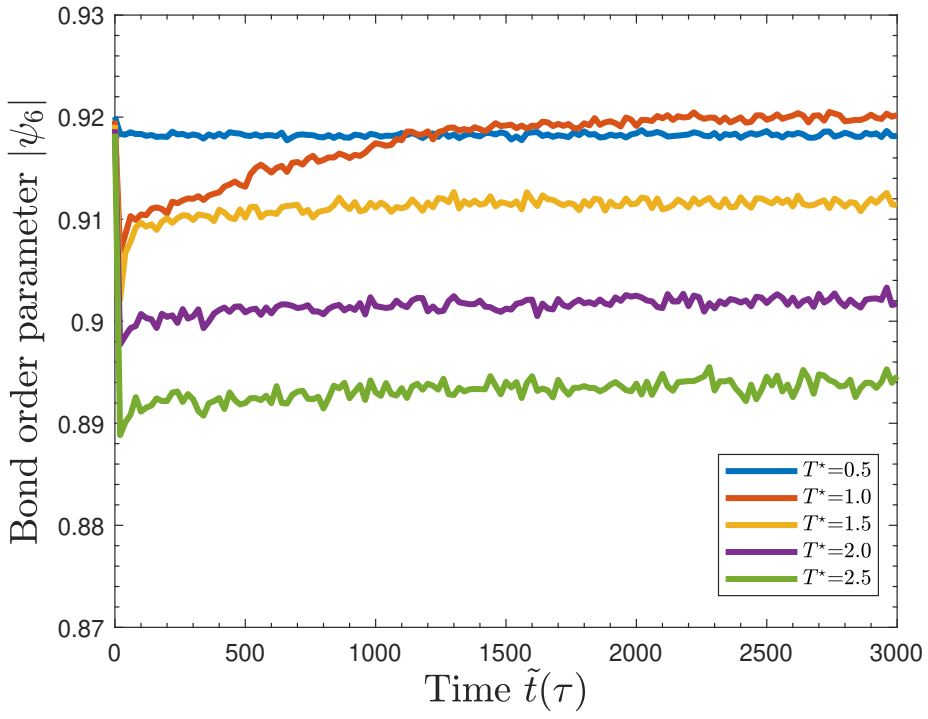


(a)

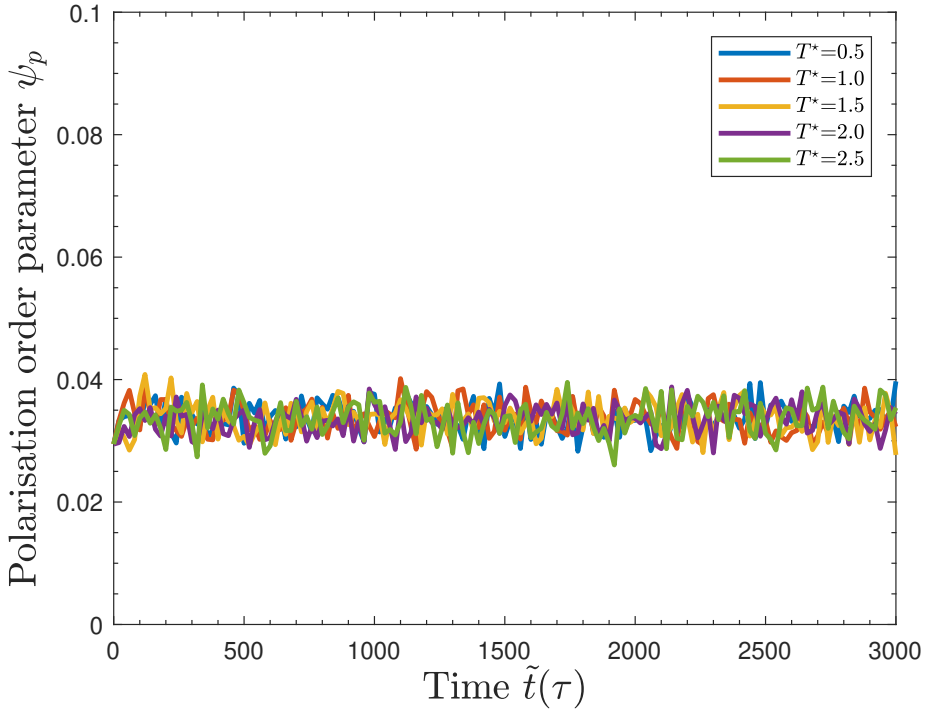


(b)

Figure F.21: Order parameters for the temperature simulations on the magic number configuration of 752 passive Brownian particles (corresponding to $F = 0$), showing a) the bond orientational order parameter $|\psi_6|$, and b) the polarisation order parameter $\psi_p$. The legend in figure e) applies to the plots of the scar composition of figures c)-d).